Strojniški vestnik

Journal of Mechanical Engineering

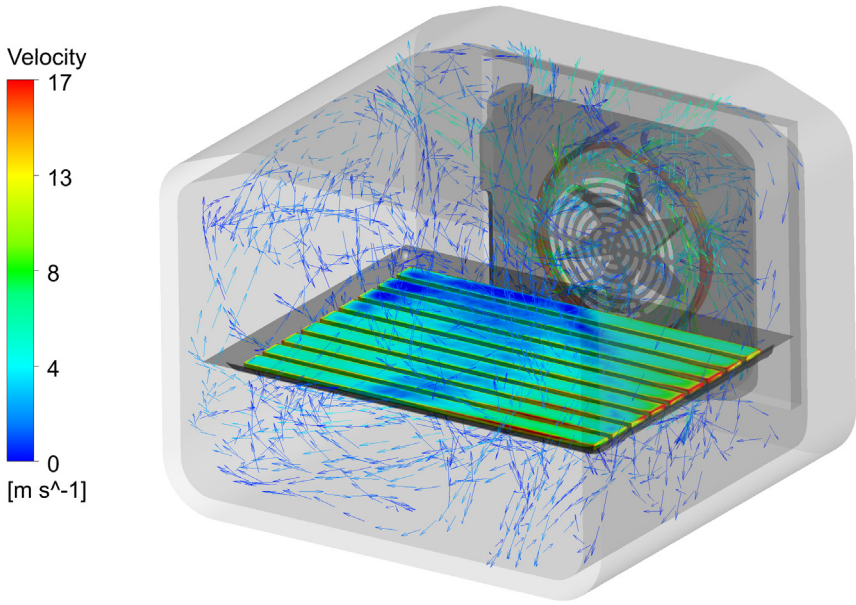

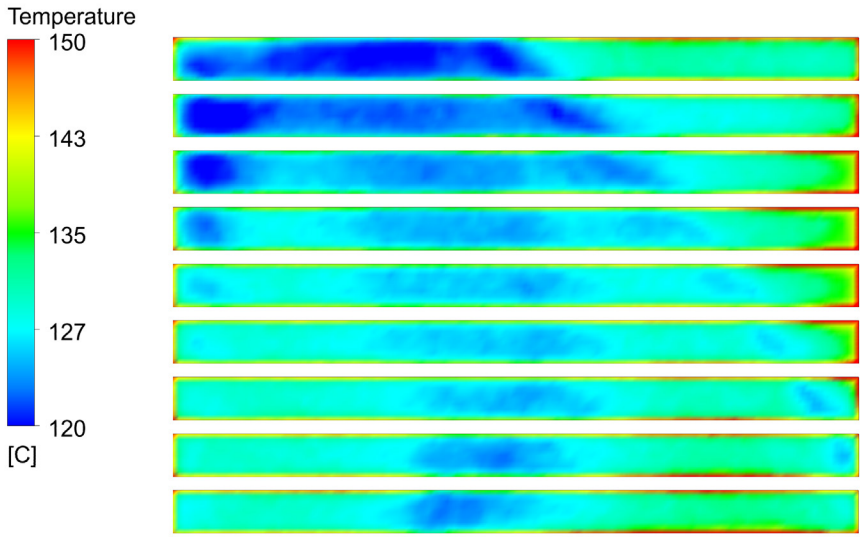

no. 4
year 2017
volume 63

Strojniški vestnik – Journal of Mechanical Engineering (SV-JME)

Aim and Scope
The international journal publishes original and (mini)review articles covering the concepts of materials science, mechanics, kinematics, thermodynamics, energy and environment, mechatronics and robotics, fluid mechanics, tribology, cybernetics, industrial engineering and structural analysis.
The journal follows new trends and progress proven practice in the mechanical engineering and also in the closely related sciences as are electrical, civil and process engineering, medicine, microbiology, ecology, agriculture, transport systems, aviation, and others, thus creating a unique forum for interdisciplinary or multidisciplinary dialogue.
The international conferences selected papers are welcome for publishing as a special issue of SV-JME with invited co-editor(s).

Editor in Chief
Vincenc Butala
University of Ljubljana, Faculty of Mechanical Engineering, Slovenia

Technical Editor
Pika Škraba
University of Ljubljana, Faculty of Mechanical Engineering, Slovenia

Founding Editor
Bojan Kraut
University of Ljubljana, Faculty of Mechanical Engineering, Slovenia

Editorial Office
University of Ljubljana, Faculty of Mechanical Engineering
SV-JME, Aškerčeva 6, SI-1000 Ljubljana, Slovenia
Phone: 386 (0)1 4771 137
Fax: 386 (0)1 2518 567
info@sv-jme.eu, http://www.sv-jme.eu

Print: Grafex, d.o.o., printed in 310 copies

Founders and Publishers
University of Ljubljana, Faculty of Mechanical Engineering, Slovenia
University of Maribor, Faculty of Mechanical Engineering, Slovenia
Association of Mechanical Engineers of Slovenia
Chamber of Commerce and Industry of Slovenia, Metal Processing Industry Association

President of Publishing Council
Branko Širok
University of Ljubljana, Faculty of Mechanical Engineering, Slovenia

Vice-President of Publishing Council
Jože Balič
University of Maribor, Faculty of Mechanical Engineering, Slovenia

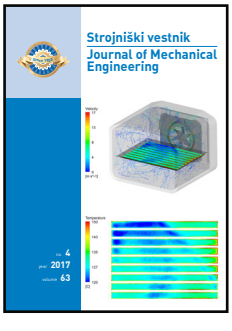

Cover:
The cover visualize the results of numerical simulation of the oven cavity. The full numerical domain where the temperature contours on the shortbread and the velocity field inside the oven are presented. The temperature field on the shortbread was used for the development of the numerical grade of browning model.

Image Courtesy:
Uroš Kokolj, Gorenje, d.d.,
R&D Competence Center Cooking Appliances,
Partizanska 12, 3320 Velenje, Slovenia,
e-mail: uros.kokolj@gorenje.com

ISSN 0039-2480

International Editorial Board
Kamil Arslan, Karabuk University, Turkey
Hafiz Muhammad Ali, University of Engineering and Technology, Pakistan
Josep M. Bergada, Politechnical University of Catalonia, Spain
Anton Bergant, Litostroj Power, Slovenia
Miha Boltežar, UL, Faculty of Mechanical Engineering, Slovenia
Franci Čuš, UM, Faculty of Mechanical Engineering, Slovenia
Anselmo Eduardo Diniz, State University of Campinas, Brazil
Igor Emri, UL, Faculty of Mechanical Engineering, Slovenia
Imre Felde, Obuda University, Faculty of Informatics, Hungary
Janez Grum, UL, Faculty of Mechanical Engineering, Slovenia
Imre Horvath, Delft University of Technology, The Netherlands
Aleš Hribernik, UM, Faculty of Mechanical Engineering, Slovenia
Soichi Ibaraki, Kyoto University, Department of Micro Eng., Japan
Julius Kaplunov, Brunel University, West London, UK
Iyas Khader, Fraunhofer Institute for Mechanics of Materials, Germany
Jernej Klemenc, UL, Faculty of Mechanical Engineering, Slovenia
Milan Kljajin, J.J. Strossmayer University of Osijek, Croatia
Peter Krajnik, Chalmers University of Technology, Sweden
Janez Kušar, UL, Faculty of Mechanical Engineering, Slovenia
Gorazd Lojen, UM, Faculty of Mechanical Engineering, Slovenia
Thomas Lübben, University of Bremen, Germany
Janez Možina, UL, Faculty of Mechanical Engineering, Slovenia
George K. Nikas, KADMOS Engineering, UK
José L. Ocaña, Technical University of Madrid, Spain
Miroslav Plančak, University of Novi Sad, Serbia
Vladimir Popović, University of Belgrade, Faculty of Mech. Eng., Serbia
Franci Pušavec, UL, Faculty of Mechanical Engineering, Slovenia
Bernd Sauer, University of Kaiserlautern, Germany
Rudolph J. Scavuzzo, University of Akron, USA
Arkady Voloshin, Lehigh University, Bethlehem, USA

General information
Strojniški vestnik – Journal of Mechanical Engineering is published in 11 issues per year (July and August is a double issue).

Institutional prices include print & online access: institutional subscription price and foreign subscription €100,00 (the price of a single issue is €10,00); general public subscription and student subscription €50,00 (the price of a single issue is €5,00). Prices are exclusive of tax. Delivery is included in the price. The recipient is responsible for paying any import duties or taxes. Legal title passes to the customer on dispatch by our distributor.

Single issues from current and recent volumes are available at the current single-issue price. To order the journal, please complete the form on our website. For submissions, subscriptions and all other information please visit: *http://en.sv-jme.eu/.*

You can advertise on the inner and outer side of the back cover of the journal. The authors of the published papers are invited to send photos or pictures with short explanation for cover content.

We would like to thank the reviewers who have taken part in the peer-review process.

© 2017 Strojniški vestnik - Journal of Mechanical Engineering. All rights reserved. SV-JME is indexed / abstracted in: SCI-Expanded, Compendex, Inspec, ProQuest-CSA, SCOPUS, TEMA. The list of the remaining bases, in which SV-JME is indexed, is available on the website.

The journal is subsidized by Slovenian Research Agency.

Strojniški vestnik - Journal of Mechanical Engineering is available on http://www.sv-jme.eu, where you access also to papers' supplements, such as simulations, etc.

Contents

Strojniški vestnik - Journal of Mechanical Engineering
volume 63, (2017), number 4
Ljubljana, April 2017
ISSN 0039-2480

Published monthly

Papers

Strojniški vestnik - Journal of Mechanical Engineering 63(2017)4, 215-224
DOI:10.5545/sv-jme.2016.4089
Original Scientific Paper
Received for review: 2016-09-28
Received revised form: 2017-01-30
Accepted for publication: 2017-02-20
© 2017 Journal of Mechanical Engineering. All rights reserved.

The Validation of Numerical Methodology for Oven Design Optimization Using Numerical Simulations and Baking Experiments

Uroš Kokolj[1,*] – Leopold Škerget[2] – Jure Ravnik[2]
[1] Gorenje, R&D Competence Center Cooking Appliances, Slovenia
[2] University of Maribor, Faculty of Mechanical Engineering, Slovenia

*In this paper, we will present the validation of numerical methodology for the improvement of baking performance of a forced convection oven. The baking performance will be assessed as the degree of uniformity between browning and temperature distribution in the oven. We found a linear relationship between the experimentally measured grade of browning and the simulated temperature distribution. Six different designs of oven fan cover were compared through numerical simulations, where a time-dependent 3D numerical model with radiative and convective heat transfers mechanism was used. The results were used in a linear model to estimate the grade of browning. The results were validated with the experimental measurements of baked shortbread using an old and improved-upon oven design. The grade of browning was determined experimentally by the colour contrasts method, based on the colour space CIE L*a*b. The results show that the improved fan cover performs better than the existing fan cover.*

Keywords: computational fluid dynamics, baking, oven, heat transfer, shortbread, optimization

Highlights

- *Numerical model for the determination of the grade of browning was used in the improvement of baking results.*
- *Six different fan cover designs are presented and analyzed.*
- *The improved fan cover decreases the difference in the grade of browning by 25.9 %.*
- *The numerical calculations were validated and match the experimental results very well.*

0 INTRODUCTION

The improvement of existing products and technologies is one of the main global aims of manufacturers and research and development (R&D) teams. In the field of cooking appliance design, baking performance, energy consumption and noise levels are the main features of the product that engineers constantly strive to improve.

The improvement of an existing product usually requires a lot of effort, time and resources for the preparation of prototypes and measurement of different solutions. In order to reach an improved solution with a minimal amount of effort, the use of numerical simulations, such as computational fluid dynamics (CFD), is becoming essential as it helps engineers to understand the processes and to prepare solutions.

The aim of this paper is to prepare and validate a methodology for the improvement of the baking performance of a forced convection oven. We propose the combination of a flow and heat transfer simulation coupled with a model for the grade of browning followed by experimental validation. In order to enable the comparison of experimental and simulation results, we will introduce a model, which is able to use CFD results for the prediction of the browning grade during the baking process. The improvement of the oven fan cover was selected as a case study. In the study, we considered the position of the tray, which is most commonly used in baking.

The use of numerical simulations to study flow and heat transfer in oven cavities has been proposed by researchers [1] to [3]. They considered natural convection ovens, where radiation is the main heat transfer mechanism. Forced convection ovens, where the fan is included, were considered by [4] to [6]. In this paper, we will optimize the baking performance of a forced hot air convection oven. In this case, the fan, the circular heating element, the fan cover and the cavity itself are the potential parts that could be optimized. Since the circular heating element and fan are standard components and because the changes in the oven cavity result in huge costs, we decided to perform the improvements on the fan cover, which is screwed into the oven cavity. The new fan cover design should not affect the other parts of the oven.

The simulation of temperature and air flow in a forced convection oven cavity was studied by [6] and [7]. They report that the performance of the fan, the shape of the fan, and the oven cavity geometry are the most important parts in the oven cavity. The difference between the numerical simulation and experimental measurements were 4.6 °C at a setting

*Corr. Author's Address: Gorenje, R&D Competence Center Cooking Appliances – Velenje, Partizanska 12, 3320 Velenje, Slovenia, uros.kokolj@gorenje.com

of 200 °C. They used the k-ε turbulence model, where the average error in the velocity field was 22 %.

A transient simulation with heating elements turning on and off was performed by [8]. The heating elements were modelled as a volume heat source. They reported that the emissivity of the heating element has a big influence on the results. If the emissivity of the heating element is reduced by 30 %, the oven wall temperature is reduced by 10 %. When the oven wall emissivity is reduced by 20 %, the temperature of the oven wall is reduced by 0.2 %. They performed a natural convection simulation of a bake cycle, where the comparison to experimental measurements showed a 4 % difference. Furthermore, they considered a natural convection simulation, where only the upper heating element was working, and the deviation to experimental measurements was 10 %.

Rek et al. [4] performed three dimensional (3D) numerical simulations of the oven cavity and the fan cover with forced convection. In the numerical model, the following two simplifications were used: the fan, which is the air flow generator, and the heating element were not included in the model. These simplifications were not made in our work.

The experimental measurements are needed to verify the improved design, which was obtained using simulations. When designing an oven cavity, the appropriate experimental method is the baking of food, where the uniformity of browning is a good indicator of how well the oven bakes. The experimental measurements were performed according to the standard EN 60350-1 [9], which prescribes how to verify and evaluate baking performance.

Researchers [1], [3] and [10] used temperature measurements and browning method for the evaluation of numerical results of the bread baking process. They report that all applied radiation models, discrete transfer radiation models, surface to surface, and discrete ordinates gave similar results.

The authors [11] used the computerized determination of the browning of baked bread. The method is based on colour space CIE L*a*b. The authors report that the change in the browning of bread is in linear correlation with its weight change.

The browning process consists of the simultaneous process of mass transfer, heat transfer and chemical reactions of caramelisation and Maillard reactions. The browning process starts when the temperature is above 120 °C and water activity is below 0.6 [12].

In our previous work [13], we developed the numerical model for the prediction of the browning grade according to the standard EN60350-1 [9]. The average shortbread temperature was used to define R_y. The averaging process starts when the surface temperature of the shortbread reaches 120 °C. In the numerical model, radiative, convective and water evaporation mechanisms are taken into account. The model was based on a 3D, time dependent numerical calculation. The model was validated through experimental measurements of the browning of baked shortbread.

The objective of this research was to validate the applicability of the developed numerical model for the determination of the browning grade of baked shortbread, and to present the use of time-dependent 3D numerical simulations for the improvement of baking performance and the design optimization of a forced convection oven.

The results of the numerical simulations were validated through the experimental measurements of baked shortbread. The grade of browning was determined for baked shortbread with the use of the reference browning measurement system (RBMS) [14], which is based on the CIE L*a*b colour space.

The paper is organized as follows: in section 1, our methods will be presented. In section 2, we will present the experimental part. The numerical model will be presented in section 3. In section 4, the results of several simulations of various fan covers and the validation with experimental results will be presented. The main conclusions and results will be summarized in section 5.

1 METHODS

The experimental and numerical methods for improving the baking performance of a forced convection oven will be developed in this paper.

To assess the baking performance of the oven, experimental measurements were performed according to the standard EN 60350-1 [9]. Furthermore, we took additional temperature, weight and heater operation measurements. The baking of shortbread was performed to assess the heat distribution of the oven cavity. The experimental results were used in two ways: firstly to determine the boundary conditions that were used to setup the simulation and secondly to validate and confirm the numerical results.

The numerical calculations for several fan cover designs were performed with commercial computational fluid dynamics software ANSYS CFX 15. 3D time dependent simulations of air flow along with convection, conduction and radiation heat transfer mechanisms were modelled. In addition, a

water evaporation model was included, since during baking an important amount of heat is used for the evaporation of water from the dough. Finally, based on the CFD results, a model was implemented to estimate the grade of browning and facilitate the comparison between the simulation and the experiment.

2 EXPERIMENTAL SETUP

The experiments were performed in two steps: the first during the baking of shortbread (temperature and mass measurements) and the second after the baking process was finished (grade of browning measurement). The experimental set up is presented in Fig. 1.

The shortbread was baked according to the standard EN 60350-1 [9] using the following mass portions: 49.9 % white wheat flour, 19.9 % margarine, 19.9 % sugar, 10 % eggs, and 0.3 % salt. The total mass of the shortbread at the start of the baking procedure was 356 g and the dimensions of the shortbread on the baking tray were 400 mm in length, 20 mm in width and 5 mm in height.

The baking was performed at a stabilized voltage of 230 V obtained by means of a stabilizer by Gorenje Orodjarna, Slovenia.

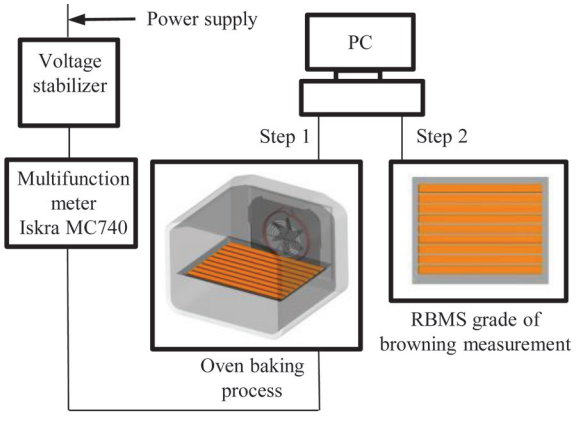

Fig. 1. *Experimental set-up of measuring system*

During the baking process, the operation of the heating elements was recorded using an Iskra MC740 multifunction meter to measure power. Fig. 2 shows the operation of the heating element during the baking process. The oven was set in such a way that both the round heating element and the fan operated. The oven fan rotation speed was measured with a digital stroboscope tachometer by Extech instruments, USA.

The temperature setting of the oven was 175 °C and the baking process lasted for 780 seconds. These parameters were reused in the setup of the numerical model.

The shortbread thermal properties before baking were: thermal conductivity λ = 0.195 W/(m·K), specific heat capacity c_p = 1921 J/(kg·K), and density ρ = 1075 kg/m^3, calculated according the portions of the ingredients added [15]. During the baking process, the water evaporates and the shortbread properties changed. The dry shortbread thermal conductivity λ was 0.128 W/(m·K), the specific heat capacity c_p was 1526 J/(kg·K) and the density ρ was 1088 kg/m^3.

The browning measurement took place 1 hour after baking due to the requirements of the standard. The sample was taken out of the oven and left on the baking tray, which was placed on a table. The measurements of the grade of the browning R_y were carried out by applying the RBMS [14]. The R_y parameter is used by the manufacturer of the browning measurement device and is the reflection density color scale based on the CIE color space. It is defined as $R_y = Y_{10}$. 63 points on the shortbread were measured (matrix 7×9).

The RBMS method is based on the optical measurement system, which is composed of a measurement chamber, a charge coupled device (CCD) camera, and lamps. The RBMS was developed in compliance with the ISO 7724 standard [16] and CIE 15.2., which is based on the CIE L*a*b colour space.

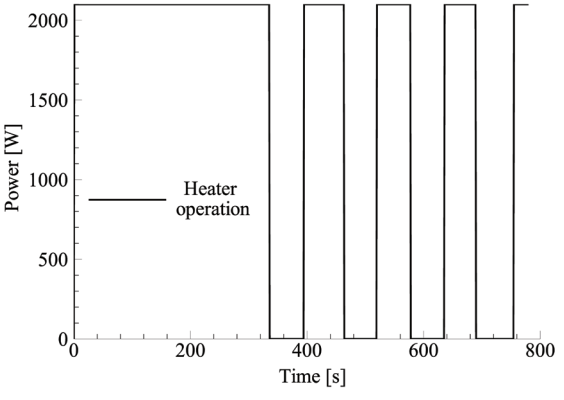

Fig. 2. *The operation of the round heating element during the baking process*

3 CFD MODELING

Simulations of air flow and heat transfer were performed using the commercial software ANSYS CFX 15 [17]. ANSYS CFX is a CFD software, which is based on the finite volume method.

The complete domain dimensions were: width 500 mm, depth 450 mm, and height 380 mm. The numerical model included radiation, conduction and convection heat transfer mechanisms. Eight solid domains were included: the insulation of the oven cavity, the oven cavity, the door glass, the fan cover, the fan, the round heating element, the shortbread, the baking tray as well as two fluid domains including stationary and rotating air. The rotating fluid domain was set as a transient rotor stator interface boundary condition within the stationary fluid domain. The conservative interface flux boundary condition was used for all connections between the domains. Fig. 3 shows all domains.

The mesh sensitivity analysis was performed in our previous work [13], where a similar oven cavity was studied. For this study, we designed the meshes in a similar fashion, keeping the number of elements and the structure of the mesh at the same level for all fan cover designs. The final mesh was designed with 4.5 million elements.

The air in the oven cavity was treated as an ideal gas for temperature dependent density, thermal conductivity, specific heat capacity and dynamic viscosity [18]. The air-flow inside the domain was assumed turbulent, with the Reynolds number 9.7×10^4, which is based on a domain length of 0.4 m and a velocity of 3.71 m/s. There are several URANS turbulence models in the ANSYS CFX [17]. Because of the coupled flow and heat transfer within the complex geometry of the numerical model and based on our previous experience with the use of the SST turbulence model [13], we chose the SST model for the analysis. We have validated the use of the SST turbulence model for oven baking in our previous work [13]. The turbulence model settings used an automatic wall function, with an initial high intensity (10 %) boundary condition. The $y+$ values on the wall ranged from 0 to 71.

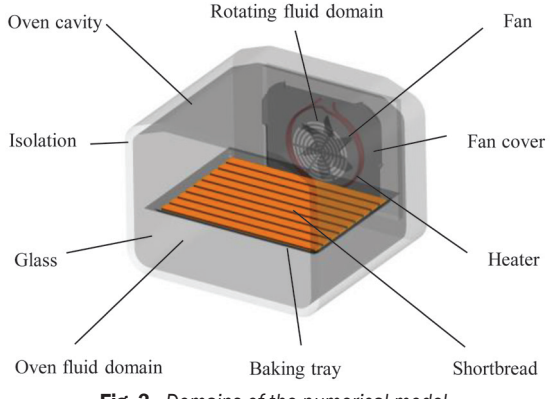

Fig. 3. *Domains of the numerical model*

The following unsteady Reynolds averaged Navier-Stokes equations for flow and heat-transfer were solved:
the continuity equation:

$$\frac{\partial \rho}{\partial t} + \nabla \cdot \left(\rho \vec{v} \right) = 0, \tag{1}$$

the momentum equation:

$$\frac{\partial \vec{v}}{\partial t} + \left(\vec{v} \cdot \nabla \right) \vec{v} = -\frac{1}{\rho} \nabla p + \mu_0 \nabla^2 \vec{v} + \frac{1}{\rho_0} \nabla \left(\bar{\tau}_{ij} + \tau_{ij}^R \right), \tag{2}$$

the energy equation:

$$\rho c_p \frac{DT}{Dt} = \lambda \nabla^2 T + S_r - S_e, \tag{3}$$

the turbulent kinetic energy equation:

$$\frac{\partial k}{\partial t} + \vec{v} \left(\nabla k \right) = \frac{P_k}{\rho_0} - \beta' k \omega + \nabla \left[\left(\mu_0 + \frac{\mu_t}{\sigma_k} \right) \left(\nabla k \right) \right], \tag{4}$$

the turbulent frequency equation:

$$\frac{\partial \omega}{\partial t} + \vec{v} \left(\nabla \omega \right) = \alpha_3 \frac{\omega}{k} \frac{P_k}{\rho_0} - \beta_3 \omega^2 + \\ + \nabla \left[\left(\mu_0 + \frac{\mu_t}{\sigma_{\omega 3}} \right) \left(\nabla \omega \right) \right] + \left(1 - F_1 \right) \frac{2}{\sigma_\omega \omega} \left(\nabla k \right) \left(\nabla \omega \right), \tag{5}$$

and the turbulent viscosity equation:

$$\mu_t = \frac{a_1 k}{\max \left(SF_2, a_1 \omega \right)}, \tag{6}$$

where p is the pressure, $\vec{v}$ is the air velocity field, T is the temperature, S_r is the radiation and S_e is the heat sink due to evaporation. τ_{ij} are viscous stresses, τ_{ij}^R is the Reynolds stress tensor, μ_t is the turbulent viscosity, k is the turbulent kinetic energy, ω is the turbulent frequency, P_k is the production of turbulent kinetic energy, F_1 and F_2 are blending functions, S is an invariant measure of the strain rate and β', σ_k, α_3, β_3, σ_ω, a_1, are constants [17]. The air density ρ_0 was obtained by the ideal gas state equation. The thermal conductivity λ and the viscosity μ_0 of the air as well as the specific heat c_p were considered temperature dependent [18]. All solid material properties, except for the shortbread, were considered to be constant. We simulated 780 seconds of baking using time steps of 10 seconds. The time step was defined and validated by our previous work [13].

The simulation was set up to mimic experimental conditions. The experiments revealed that the heating element can be modelled as a volume energy source at a power of 2100 W. The oven fan rotates at a speed 1350 min^{-1} at a temperature of 20 °C in the oven and 1800 min^{-1} at a temperature of 175 °C. The oven speed

varies because of the air property change due to its heating up the oven. In the simulation, the fan rotation speed changed as a linear function of temperature.

Since the heating element reaches up to 700 °C during baking, radiation plays an important role in the numerical model. The optical thickness is a good indicator for the selection of the radiation model. In our case, the length scale was L = 0.45 m and the absorption coefficient was 0.01 m^{-1} yielding the optical thickness which is much smaller than the unity. The optical thickness defines which radiation model should be used. P1 and Rosseland models are best suited for optically thick materials (where radiation absorption is important), while the Monte Carlo model, which we used, is appropriate for media, where the absorption of radiation is minimal **[17]**. The Monte Carlo radiation model is capable of modeling radiation through the glass door and transparent materials. In our case, the glass was treated as a transparent material with the absorption coefficient a = 89.15 m^{-1}, calculated using Eqs. (7) and (8) and the refractive index of 1.51 **[17]**.

$$I = I_0 e\left(-\alpha x\right), \tag{7}$$

$$a = -\frac{1}{x}\ln\left(T\right) = 89.15\ m^{-1}. \tag{8}$$

The radiation properties and emissivity of the enameled elements were prescribed 0.9 **[2]**, **[8]** and **[13]** and were considered composite materials of steel and enamel with thermal conductivity λ = 45.7 W/(m·K), a specific heat capacity c_p = 513 J/(kg·K), and density ρ = 6515.5 kg/m^3 **[13]**. The emissivity of the heating element and the fan, which are made of steel was 0.85 **[2]**, **[8]** and **[13]**.

The no-slip velocity boundary condition was applied to the walls of the model. Due to the natural convection of the air outside of the domain, a low value of the heat transfer coefficient was prescribed at the insulation, h = 5 W/(m^2·K). A heat transfer coefficient of 5 W/(m^2·K) was used for cases where natural convection cooling took place under quiet ambient conditions **[19]**. Such conditions were set up in our laboratory when experiments were conducted, thus we have used this value in the numerical model. Furthermore, the outside heat transfer coefficients were defined by comparing the experimentally measured temperatures in an empty oven with a simulation.

Due to the slightly forced convection of the cooling system at the door glass, a higher value of the heat transfer coefficient was prescribed there, h = 13 W/(m^2·K) **[13]**.

The experiment showed that during the baking process, water evaporates and the shortbread mass is reduced by 14.89 %. The results of mass measuring experiments are presented in Fig. 4. In the numerical model, the evaporation was modelled as a heat sink of, $S_e = mH_w/t$ = 249.7 W **[13]**. Here m = 42 g is the mass of evaporated water, H_w = 2260 kJ/kg is the water vaporization heat and t = 380 s is the duration of the evaporation process, which causes linear shortbread mass loss, see Fig. 4. Evaporation was modelled as a temperature dependent heat sink imposed on the shortbread. This kind of evaporation model was developed in **[13]** and was adopted here.

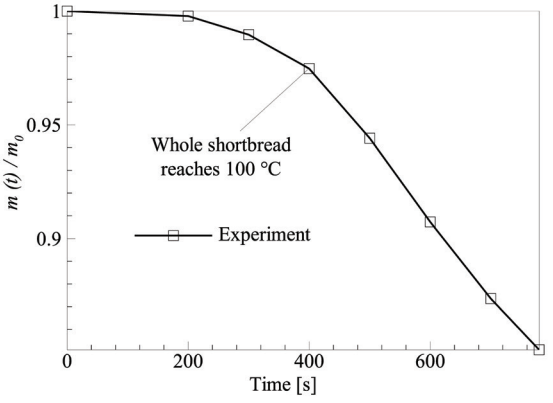

Fig. 4. *Shortbread mass change due to the evaporation of the water; the mass at the start of the baking process was m_0 and the mass as a function of time during the baking process was m (t)*

Due to the evaporation process, the change in shortbread properties has also been included in the numerical model. Since the shortbread mass changes linearly over time (Fig. 4), we calculated the shortbread properties using a linear model interpolating between the wet shortbread properties before baking and the dry shortbread properties after baking.

4 RESULTS AND DISCUSSION

The results of the numerical simulations and experimental measurements have been compared to the grade of browning method. For comparison, a different grade of browning fields of baked and simulated results have been used. The experimental grade of browning has been established through the RBMS system according to the standard EN 60350-1 **[9]**. For the evaluation of numerical results, the numerical grade of browning model was developed **[13]**. In our previous work, we evaluated the empty oven cavity with numerical simulations where the average difference between the experimental

measured and numerically calculated temperature at the center of the oven was 2.8 K and 5.6 K in the shortbread. For development of the model, we used the boundary condition that the browning starts when the first measurement point on the shortbread exceeds 120 °C **[20]**.

Secondly, we compared the experimental results of the browning grade of baked shortbread and the temperatures of the numerical calculation and found a linear relationship. For the determination of the numerical browning grade, the following model was proposed **[13]**:

$$R_y = \alpha T + \beta. \quad (9)$$

After adopting the model for the present case, we found that the constants of the model are: and . Based on our experimental data and simulation results, the equation is valid for the temperature range from 100 °C to 150 °C. The Eq. (9) was used to predict the browning grade based on the CFD simulations of different fan cover designs.

We simulated the existing and five additional fan cover designs. The CPU time was 28 hours and using 12 processors / simulation.

All designs of the fan cover along with descriptions of their modifications are presented in Fig. 5. The existing fan cover is marked with a). Detailed descriptions of the modifications are given in Table 1.

Table 1. *Modifications of various fan covers*

	Modifications
a)	Existing fan cover
b)	Closed opening 1
c)	Closed opening 1 and 2
d)	Closed opening 1, 50 % closed upper opening
e)	Closed opening 1, 50 % open corner
f)	Closed opening 1, 20% closed upper opening

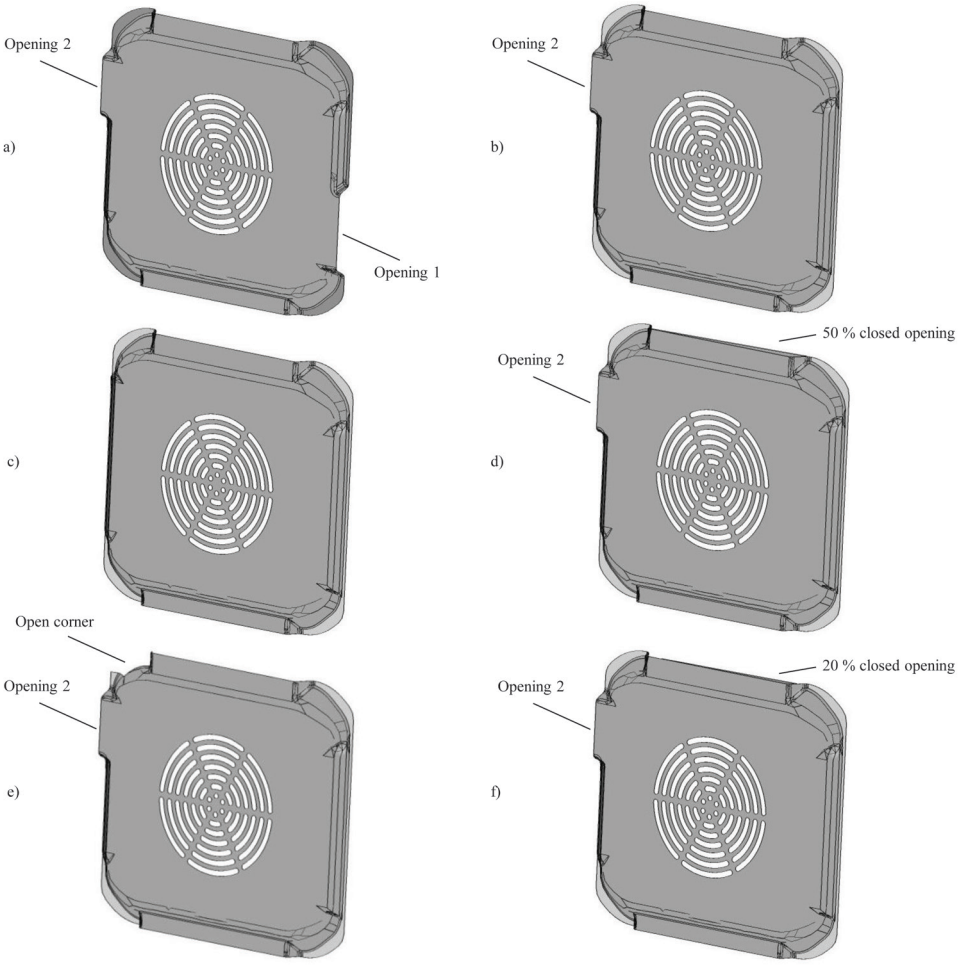

Fig. 5. *Existing fan cover a) and modifications b), c), d), e) and f)*

The results of the numerical simulations of different fan cover models are presented in Table 2 and in Fig. 6. The R_y contours were obtained by the interpolation of 7×9 R_y measurements. Two different criteria were used: the difference in the maximum and minimum grade of browning ($R_{y\,max} - R_{y\,min}$) and the standard deviation σ of the field of the browning grade, which was estimated using the following equation, Eq. (10):

$$\sigma = \sqrt{\frac{1}{n}\sum_{i=1}^{n}\left(R_{yi} - \overline{R_y}\right)^2}, \qquad (10)$$

where $\overline{R_y}$ is the average grade of browning and $n = 63$ are all of the measurement points.

The reason for introducing the two criteria is two-fold: From an oven user point of view, an important indicator of oven quality is the difference in browning along the whole baking tray as well as the uniformity of browning of the baked food.

Table 2. *Numerical results of various fan covers*

	$R_{y\,max} - R_{y\,min}$ [%]	σ
a)	22.21	4.82
b)	13.46	2.99
c)	26.16	7.65
d)	33.92	8.27
e)	21.10	5.56
f)	15.57	3.66

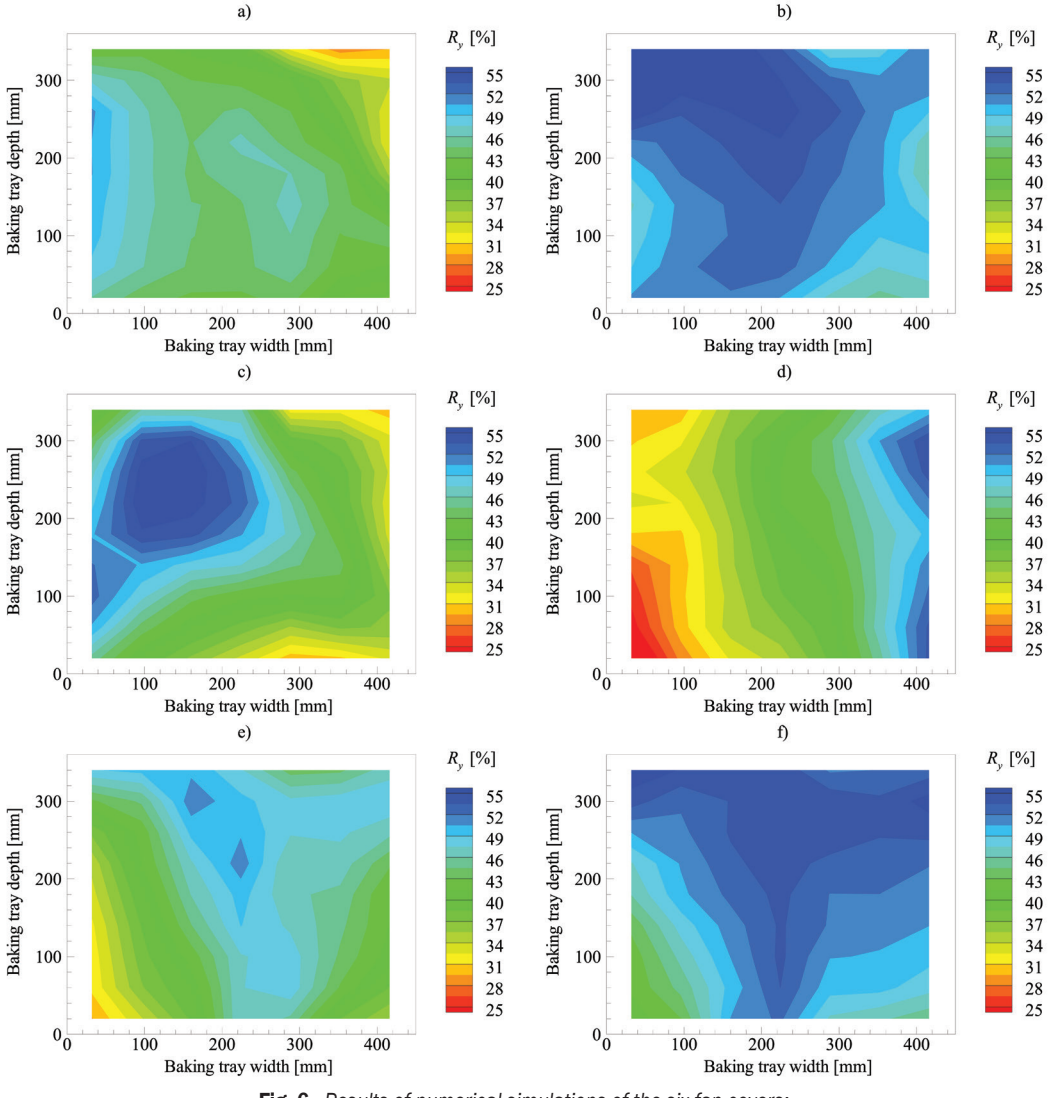

Fig. 6. *Results of numerical simulations of the six fan covers: a) existing fan cover, b), c), d), e), f) new designs; the numerically estimated grade of browning R_y is also presented*

Considering all of the fan cover designs (Table 2), we have observed that the lowest difference in the grade of browning, 13.46, and the lowest value of standard deviation, 2.99, were found for fan cover design b).

In order to visualize the results of numerical simulation, Fig. 7 shows the full numerical domain where the temperature contours on the shortbread at the end of the numerical simulation for variant b) are presented.

The existing fan cover a) and the improved version b) were verified by an experimental test of baking shortbread and evaluated through the grade of browning based on the RBMS method. The results of the experimental measurements are presented in Fig. 8. The results are presented on a common scale of the grade of browning, so it is easy to visualize the improvement of fan cover variant b). With design b), the intensive browning on the rear right part of the baking tray disappears.

In Table 3, the difference in the grade of browning between the existing and improved fan cover is shown, which was obtained experimentally.

Table 3. *Experimental results of a) existing and b) improved fan cover*

	$R_{y\,max} - R_{y\,min}$ [%]	σ
a) Existing	31.10	6.64
b) Improved	23.06	5.13

The new design of the fan cover decreased the difference in the grade of browning R_y between the maximal and minimal value for 25.9 % and improved the uniformity of baking performance by 22.7 %. In comparison with the numerical estimation the difference in the grade of browning R_y was predicted to improve by 39.3 % and the equality of baking performance by 37.9 %. These values were obtained by using the following equation: (new design/old design - 1) ×100. The numerical simulation predicted the improvement of the fan cover well, even though the model is a simplified version of the experimental set-up. This results prove, that the proposed CFD model alongside with the grade of browning model are capable of verifying oven design changes.

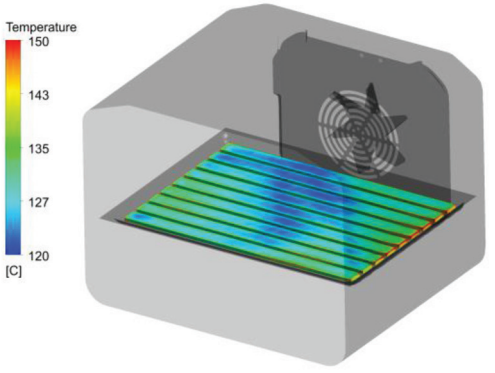

Fig. 7. *Temperature distribution of numerical simulation for fan cover version b)*

The velocity field, 20 mm above the baking tray, is shown in Fig. 9. The impact of the new proposed fan cover on browning is very visible in the right rear corner of the oven cavity, where the velocity decrease is significant in comparison to the existing fan cover. The decreased velocity leads to improvement in the uniformity of the baking in this corner.

This means that with a lower forced convection heat transfer originating from the fan cover openings, we are able to reduce browning in this area. Furthermore, Fig. 9 also shows the low velocity field area in the left rear corner, which means that the browning in this area starts later on.

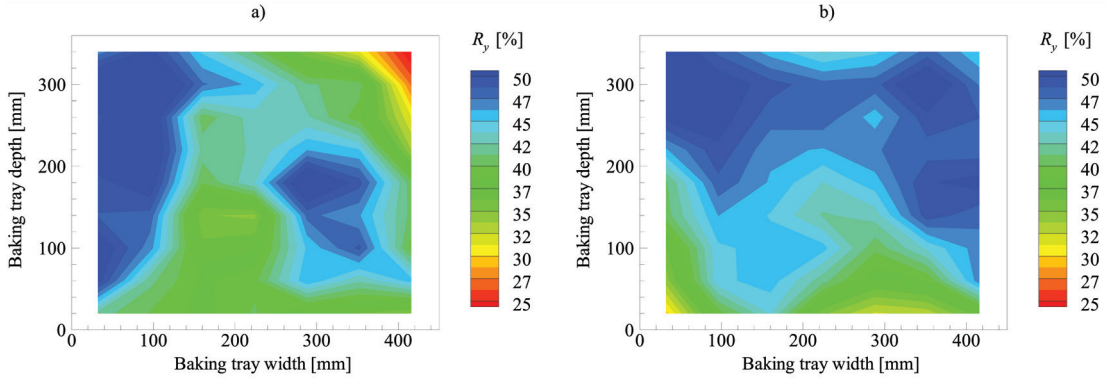

Fig. 8. *Grade of browning of experimental results of a) existing and b) improved fan cover*

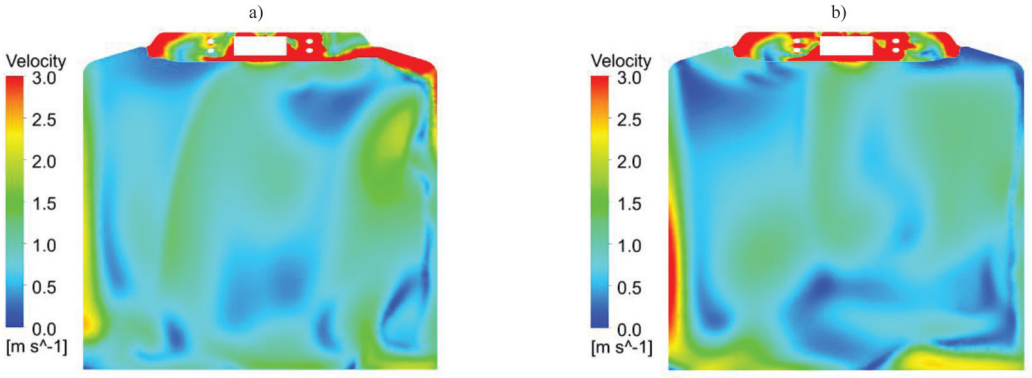

Fig. 9. *The velocity field of a) existing fan cover and b) improved fan cover*

The results of the velocity field, 20 mm above the baking tray, are presented in Table 4. The standard deviation $\sigma_{(x,y,z)}$ of the velocity field was estimated by using the following equation, Eq. (11):

$$\sigma_{(x,y,z)} = \sqrt{\frac{1}{n}\sum_{i=1}^{n}\left(v_{(x,y,z)i} - \overline{v_{(x,y,z)}}\right)^2}. \qquad (11)$$

Table 4. *Results of the velocity field 20 mm above the baking tray*

	v_{average} [m/s]	σ_x	σ_y	σ_z
a) Existing	0.98	0.49	0.39	0.25
b) Improved	0.79	0.41	0.35	0.29

5 CONCLUSIONS

The objective of this study was to propose and validate the methodology, which uses computational fluid dynamics combined with additional models for evaporation and grade of browning to improve the baking performance of the oven cavity.

We focused our attention on the design of the fan cover. Several designs were considered using the proposed numerical methodology. Based on the uniformity of the grade of browning, we identified the optimal design. The optimal fan cover design was confirmed and validated by the experimental measurements of baking performance, where the measurements of the grade of browning R_y were carried out. The results of the numerical calculation correspond very well to the experimental measurements.

This satisfactory agreement between the experiment and simulation validates the proposed methodology. Using the simulation methodology in the design process will enable engineers to quickly and efficiently verify new design ideas and thus speed up the design process. Furthermore, the use of the developed methodology will help the engineers avoid the preparation of a large number of expensive prototypes.

6 ACKNOWLEDGEMENTS

This research was co-financed by the public agency, Spirit Slovenia. The authors gratefully acknowledge the support of the manufacturer of home appliances, Gorenje, d.d..

7 REFERENCES

[1] Chhanwal, N., Anishaparvin, A., Indrani, D., Raghavarao, K.S.M.S., Anandharamakrishnan, C. (2010). Computional fluid dynamics (CFD) modeling of an electrical heating oven for the bread baking process. *Journal of Food Engineering*, vol. 100, no. 3, p. 452-460, **DOI:10.1016/j.jfoodeng.2010.04.030**.

[2] Mistry, H., Ganapathisubbu, S., Dey, S., Bishnoi, P., Castillo, J.L. (2011). A methodology to model flow-thermals inside a domestic gas oven. *Applied Thermal Engineering*, vol. 31, no. 1, p. 103-111, **DOI:10.1016/j.applthermaleng.2010.08.022**.

[3] Ploteau, J.P., Nicolas, V., Glouannec, P. (2012). Numerical and experimental characterization of a batch bread baking oven. *Applied Thermal Engineering*, vol. 48, p. 289-295, **DOI:10.1016/j.applthermaleng.2012.04.060**.

[4] Rek, Z., Rudolf, M., Žun, I. (2012). Application of CFD simulation in the development of a new generation of heating oven. *Strojniški vestnik - Journal of Mechanical Engineering*, vol. 58, no. 2, p. 134-144, **DOI:10.5545/sv-jme.2011.163**.

[5] Verboven, P., Datta, A.K., Anh, N.T., Scheerlick, N., Nicolai, B.M. (2003). Computation of airflow effects on heat and mass transfer in a microwave oven. *Journal of Food Engineering*, vol. 59, no. 2-3, p. 181-190, **DOI:10.1016/S0260-8774(02)00456-9**.

[6] Verboven, P., Scheerlinck, N., De Baerdemaeker, J., Nicolai, B.M. (2000). Computational fluid dynamics modelling and validation of the isothermal airflow in a forced convection oven. *Journal of Food Engineering*, vol. 43, no. 1, p. 41-53, **DOI:10.1016/S0260-8774(99)00131-4**.

[7] Verboven, P., Scheerlinck, N., De Baerdemaeker, J., Nicolai, B.M. (2000). Computational fluid dynamics modelling

and validation of the temperature distribution in a forced convection oven. *Journal of Food Engineering*, vol. 43, no. 2, p. 61-73, **DOI:10.1016/S0260-8774(99)00133-8**.

[8] Mistry, H., Ganapathi-subbu, S., Dey, S., Bishnoi, P., Castillo, J.L. (2006). Modeling of transient natural convection heat transfer in electric ovens. *Applied Thermal Engineering*, vol. 26, no. 17-18, p. 2448-2456, **DOI:10.1016/j.applthermaleng.2006.02.007**.

[9] EN 60350-1:2013. H*ousehold Electric Cooking Appliances Part 1: Ranges, Ovens, Steam Ovens and Grills - Methods for Measuring Performance*. CENELEC European Committee for Electrotechnical Standardization, Brussels.

[10] Chhanwal, N., Indrani, D., Raghavarao, K.S.M.S., Anandharamakrishnan, C. (2011). Computational fluid dynamics modeling of the bread baking process. *Food Research International*, vol. 44, no. 4, p. 978-983, **DOI:10.1016/j.foodres.2011.02.037**.

[11] Purlis, E., Salvadori, V.O. (2007). Bread browning kinetics during baking. *Journal of Food Engineering*, vol. 80, no. 4, p. 1107-1115, **DOI:10.1016/j.jfoodeng.2006.09.007**.

[12] Purlis, E. (2010). Browning development in bakery products - A review. *Journal of Food Engineering*, vol. 99, no. 3, p. 239-249, **DOI:10.1016/j.jfoodeng.2010.03.008**.

[13] Kokolj, U., Škerget, L., Ravnik, J., (2017). A numerical model of the shortbread baking process in a forced convection oven. *Applied Thermal Engineering*, vol. 111, p. 1304-1311, **DOI:10.1016/j.applthermaleng.2016.10.031**.

[14] SLG, Pruf und Zertifizierungs, GmbH. (2009). *Reference Browning Measurement System for the Determination of Browning Values if Small Cake*s, Hartmannsdorf.

[15] ASHRAE Handbook, (2006). *Refrigeration: SI Edition (International System of Units)*. ASHRAE Publications, Atlanta.

[16] ISO 7724-1:1984. *Paints and Varnishes, Colorimetry, Part 1: Principle*s. ISO International Organization for Standardization, Geneva.

[17] *ANSYS 15 CFX*, ANSYS Inc., Southpointe, 2600 ANSYS Drive, Canonsburg.

[18] Incropera, F.P., Dewitt, D.P., Bergman, T.L., Lavine, A.S. (2007). *Fundamentals of Heat and Mass Transfer, 6th ed*. John Wiley & Sons, Inc., Hoboken.

[19] Bird, R.B., Stewart, W.E., Lightfoot, E.N. (2007). T*ransport Phenomena,* Revised 2nd ed. John Wiley & Sons, Inc., New York.

[20] Purlis, E., Salvadori, V.O. (2009). Modeling the browning of bred during baking. *Food Research International*, vol. 42, no. 7, p. 865-870, **DOI:10.1016/j.foodres.2009.03.007**.

Strojniški vestnik - Journal of Mechanical Engineering 63(2017)4, 225-234
© 2017 Journal of Mechanical Engineering. All rights reserved.
DOI:10.5545/sv-jme.2016.4239 Original Scientific Paper
Received for review: 2016-12-04
Received revised form: 2017-02-16
Accepted for publication: 2017-03-13

Pneumatic Muscle-Actuated Adjustable Compliant Gripper System for Assembly Operations

Tudor Deaconescu* – Andrea Deaconescu
Transilvania University of Brasov, Romania

The aim of this paper is to present and discuss an innovative, constructive solution for a gripper system that can be attached to an industrial robot for assembly operations. The construction of this gripper system is based on a linear pneumatic muscle used as the actuator and the transmission of motion by gear-and-rack mechanisms. Air compressibility renders pneumatic muscle behaviour inherently compliant; this favours automated assembly applications as it allows the correction of inevitable lateral and angular misalignments in mating operations. Therefore, the jamming of a peg-like object can be avoided when this is introduced into a hole with tight clearance. In addition to the construction of the gripper system, this paper discusses its actuation, as well other characteristics.
Keywords: assembly, compliance, grippers, manipulators, pneumatic muscles, stiffness

Highlights
- *An adjustable compliant gripper system for assembling robots is proposed.*
- *The utilised motor, namely the pneumatic muscle, benefits from adjustable compliance and can adapt its operational behaviour between two limits, ranging from rigid (for high accuracy positioning) to compliant.*
- *The structural diagram of the gripper system, its construction and its pneumatic control diagram are presented.*
- *The variation of the gripper system stiffness and compliance are both demonstrated.*

0 INTRODUCTION

Grippers are defined as those components of robots that facilitate temporary contact with a manipulated object, ensuring its position and orientation during transport, assembly or while conducting certain specific tasks. At present, grippers tend to become increasingly sophisticated, more complex, so as to meet varied requirements. Complex construction, however, entails high costs, often unacceptable in a competitive industrial scenario [1]. For this reason, current industrial applications typically deploy simple and reliable gripper systems, while for research purposes complex mechanical hands are proposed.

One modality of classifying gripper systems is by their destination. According to this criterion, while gripper systems can be designed for industrial applications, another category includes mechanical hands used mostly for research. In principal, industrial gripper systems are described by the developed force and their structural rigidity. These characteristics can be ensured by conceiving grippers with few degrees of freedom, thus facilitating system reliability and low costs. Mechanical hands resemble natural systems and are thus characterized by better compliance and dexterity, which makes them eligible for dexterous applications [2].

Conceiving a novel gripper system entails correctly defining its required functional characteristics. Requirements, such as the developed force, stiffness/compliance, dexterity, and the number of degrees of freedom, depend on the application for which the gripper is designed. Studies have revealed that if the object gripping ability of a five-finger mechanical hand is of 100 %, then a four-finger mechanical hand will have 99 % of its ability, a three-finger one about 90 %, while this ability will be of only 40 % in a hand with two "fingers" [3].

In applications in which emphasis is laid on safe seizing, the risk of damaging the seized object can be significantly reduced by drastically increasing sensorization and by adequate design of the control diagrams. An alternative to over-sensorization is using variable stiffness actuators (VSAs), also known as adjustable compliant actuators (ACAs). These actuators are used because of their benefits, including the capacity of minimizing the effects of mechanical shocks, the safety of interaction with human operators or the ability to store and release energy into passive elastic elements [4].

The utilization of adjustable compliant actuators ensures the adaptability of the gripper system to concrete work situations that may differ from the initially envisaged ones. A mechanical system is defined as adaptive when it has the capacity to adequate responding to new situations within the limitations given by the mechanical band width determined by the system's elasticity and inertia, as well as by the internal friction. In such a system, the presence of sensors or complex controllers is not

*Corr. Author's Address: Transilvania University, 29 Eroilor Bd., Brasov, Romania, tdeacon@unitbv.ro

necessary, as it is the mechanical system itself that provides the required adaptive behaviour [5].

In the case of gripper systems, adaptive behaviour entails adaptation to either the (irregular) shape of the seized object, or to the constraints created by the environment it evolves within (for example positioning the gripper relative to the object). In recent years, numerous efforts have been made to create new gripper systems with easily achievable and controllable constructions, adaptable to environmental constraints. Thus, paper [6] presents a highly compliant robotic hand actuated via a novel pneumatic actuator, called PneuFlex. Paper [7] discusses an object-grasping strategy with directional position uncertainty, and [8] presents a tendon-driven robotic gripper performing fingertip and enveloping grasps. In [9], the authors describe a novel adaptive and compliant grasper that can grasp objects spanning a wide range of size, shape, mass, and position/orientation using only a single actuator.

Robot applications for assembly entail the utilization of adjustable compliant gripper systems. This has become desirable because, while at present, very good positioning precisions can be obtained, assembly errors caused by machine inaccuracy (tolerances), vibration, effects of contamination, etc., will still occur. The deployment of a robot arm of lesser positioning precision and combined with a compliant gripper system provides a more cost-effective solution.

In manual assembly, the above difficulties can be easily overcome by the human operator drawing upon the brain's reasoning capacity, expertise, experience and the dexterity of their fingers (the fingers' compliance). All these are completed by closed loop control provided by the link between the senses and the brain [10].

In automated assembly, the above disadvantages can be prevented by either uncontrolled (passive) mating mechanisms: remote centre compliance mechanisms (RCC) or controlled (active and passive) mating mechanisms, and instrumented remote centre compliance (IRCC) mechanisms [10].

An RCC mechanism is a passive mechanical device that facilitates automated assembly by correcting inherent lateral or angular misalignments in mating operations. Thus, the jamming of a peg-like object can be avoided when this is introduced into a hole with tight clearance.

The construction of gripper systems for automated assembly includes an RCC device that ensures the adaptive behaviour required for compensating the misalignments of mating parts. The need for developing gripping systems that allow adaptive behaviour has yielded numerous solutions of actuators, sensors and structural design. Nature is an endless source of inspiration for engineers and holds many examples of gripper systems that can become starting points for practical applications. A few such examples of natural grippers are bird claws and beaks, elephant trunks, octopus tentacles, each using mechanical contact forces. While in natural systems these forces are generated by muscles, artificial grippers use motors to develop forces [2].

The above examples suggest that innovative, bio-inspired gripper systems should be made from light components that can be flexibly structured, that ensure a large useful load-to-eigenweight ratio, that have integrated position and force control, all at an affordable price. It is in this sense that this paper presents and discusses the construction and performance of a novel gripper system actuated by a pneumatic muscle type motor, a bioinspired system similar to human and animal muscles.

The second part of the paper presents the actuator used in the construction of the gripper system for automated assembly, with an emphasis on a characteristic of the pneumatic muscle, namely compliance. The third part of the paper describes the construction of the gripper system and its actuation, and the fourth part presents the experimental results obtained for system compliance. The paper continues with the presentation and discussion of a case study of a mating operation (peg into hole) and is finalized by a section for conclusions.

1 THE PNEUMATIC MUSCLE – A COMPLIANT ACTUATOR

The pneumatic muscle mimics the behaviour of natural muscle fibres, and is characterized by low weight, reduced overall dimensions, a small mass-to-power unit ratio, the capacity to absorb shocks, as well as compliance. When fed compressed air, the pneumatic muscle contracts axially and deforms radially. The compressibility of air makes it inherently compliant (passive compliant actuator), and it behaves in a spring-like fashion, that can store energy.

The emergence of pneumatic muscles has led in certain applications to the replacement of single-acting pneumatic cylinders. Compared to these, pneumatic muscles of the same size have an eight-times lower weight, while generating a ten-times greater force. As in pneumatic muscles, stick-slip does not occur, motions of small amplitude and reduced velocity are achievable, thus proving their superior dynamic behaviour compared to pneumatic cylinders.

Using pneumatic muscles in grippers ensures obtaining of light and flexible constructions capable of safely manipulating objects. Firm gripping of an object without damaging it is ensured by a special characteristic of pneumatic muscles, known as compliance.

Compliance, the inverse of rigidity is an actuator's characteristic of allowing deviations from a certain position of equilibrium when the system is subject to the action of exterior forces. Actuators are adjustable compliant when their stiffness is not constant, which is the case when the dependency between the developed force and the displacement is non-linear. Pneumatic muscles (bio-inspired actuation systems) fit this description, due to their adaptive compliant behaviour, materialized by the possibility of continuous variation of the stiffness [11].

The utilization of pneumatic muscles in the construction of gripper systems remains in an incipient stage, because of the relatively recent emergence of these actuators. An example of a pneumatic muscle-actuated gripper system is the device called Power Gripper manufactured by Festo (Germany), based on the way birds seize objects with their beaks [12]. The construction of the gripper is based on Watt linkages, and due to the deployment of a light motor (a pneumatic muscle) the system has a well-developed force-to-eigenweight ratio.

Other such achievements can be found in literature [13] and [14].

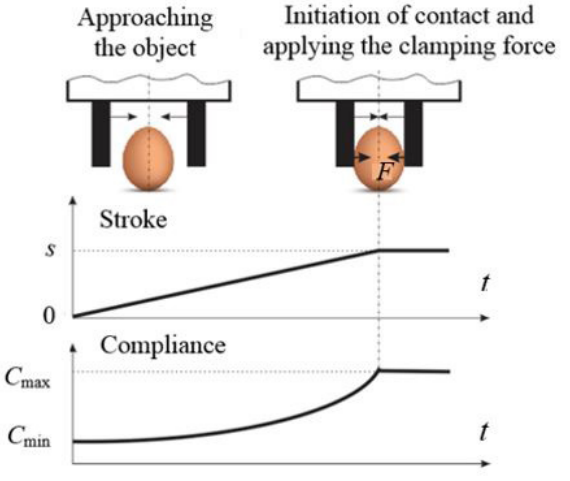

Fig. 1. *Variation versus time of jaw stroke and system compliance*

Fig. 1 presents certain standard phases of the gripping process, namely approaching the targeted object, initiation of contact and securing the seized object between the jaws by increasing the clamping force. For these phases graphs that describe the evolution versus time of the jaw stroke and of the compliance are presented. It can be noticed that once contact has been made with the targeted object, in order to avoid deformation of the object, the jaws remain motionless in position; thus, in this position of the jaws a maximum compliance has to be reached, such as to allow the correction of misalignments.

The pneumatic muscle is a passive compliant actuator, whose compliance is dependent on the stroke. For this reason, the compliance varies (increases) inevitably over the entire carried-out stroke, even before contact occurs between the jaw and object to be seized. Significant is the concave shape of the curve describing the variation of compliance; in the first part of the curve corresponding to the first stage of jaw motion: approaching the targeted object, the gradient of compliance increase is small, while at the end of stroke compliance increases abruptly. When clamping between the jaws is achieved, the compliance of the gripper system needs to reach its highest values, thus allowing manipulation without the risk of deforming/destroying the seized object.

An adjustable compliant motor can adapt its operational behaviour between two limits, ranging from rigid - for high accuracy positioning - to compliant, when the primary desired result is not precision, but safety of the motion [15]. A compliant actuator, like the pneumatic muscle, allows deviations from the position of equilibrium of a magnitude depending on the external forces the actuated element is subjected to [4].

Structures that can go from soft to rigid and vice-versa (adjustable compliant ones) are used in this paper in order to design a novel gripper system for assembly operations. The gripper system includes a pneumatic muscle as a motor and a power transmission mechanism consisting of gears and racks.

2 THE CONSTRUCTION OF THE GRIPPER SYSTEM

While pneumatic muscles, as adjustable compliant actuators, are used mostly in applications where the safety of man-robot interactions needs to be ensured with priority, their deployment in other industrial applications is not excluded. An example of such application is assembling, such as introducing a peg into a hole (Fig. 2).

If the two components are not coaxial, the presence of a compliant assembling system is required such as to allow the compensation of the deviations. In order to facilitate the assembling, guiding chamfers are to be machined either at the upper part of the

hole or the extremity of the peg or at the end of both components.

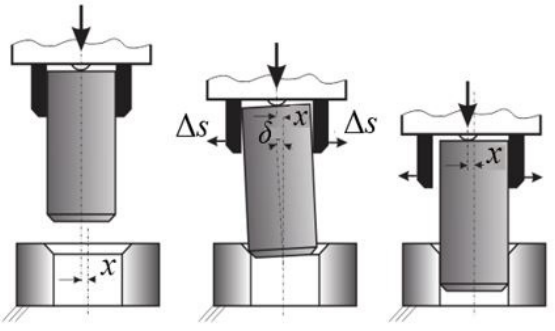

Fig. 2. *Schematic of self-adaptive assembling*

The figure shows that initially the peg and the hole are not coaxial. As soon as the front end of the peg makes contact with the hole's chamfer, the jaws of the gripper system are capable of displacement such as to compensate the misalignment. This, however, is possible only in case of a compliant actuation system of the jaws.

The gripper proposed in this paper is an asymmetrical two-jaw system, with a gear mechanism for power transmission. The asymmetry of the gripper system is given by the asymmetrical positioning of the pneumatic muscle in relation to the symmetry axis of the seized object, which allows fitting the proportional pressure regulator into the gripper body. In contrast, the asymmetry of the gripper is also given by the non-identical structures of the two component linkages, the former including one intermediary gear and the latter two intermediary gears.

The gripper system was dimensioned based on the following input data: mass of the object m = 0.7 kg; acceleration of the motion of the system consisting of the gripper and the object: a = 5 m/s^2; gravitational acceleration: g = 9.81 m/s^2; emergency stop deceleration: a_S = 10 m/s^2; friction coefficient: μ = 0.2; safety coefficient: S = 2.5. Taking into account the imposed requirements related to functioning and overall dimensions, the model proposed in this paper uses the smallest pneumatic muscle, (MAS-10-45N-AA-MC-O-ER-EG), with an interior diameter of 10 mm and an active length of 45 mm.

The maximum forces that have to be developed by this pneumatic muscle are generated when the accelerations are maximum, namely in sudden braking. In such case, the necessary gripping force of one jaw is computed by Eq. (1):

$$F_{jaw} = \frac{m \cdot (g + a_S) \cdot S}{\mu \cdot n} = \frac{0.7 \cdot (9.81 + 10) \cdot 2.5}{0.2 \cdot 2} = 86.67 \text{ N}. \quad (1)$$

The construction of the proposed gripper system has two jaws; therefore, the selected pneumatic muscles have to be able to develop a force of minimum 2 × 86.67 N = 173.34 N. Fig. 3 presents the graph that describes the evolution of the force developed by the selected pneumatic muscle versus charging pressure and stroke. The hachured rectangle highlights the optimum deployment area of the pneumatic muscle, so that for a maximum stroke of the jaws of 4 mm, the developed force exceeds 173.34 N.

Fig. 4 shows a view of the gripper system and Fig. 5 illustrates its pneumatic control diagram. The pneumatic control diagram of the pneumatic muscle includes a proportional pressure regulator (MPPES-3-1/4-6-010), controlled by a reference module MPZ-1-24DC-SGH-6-SW.

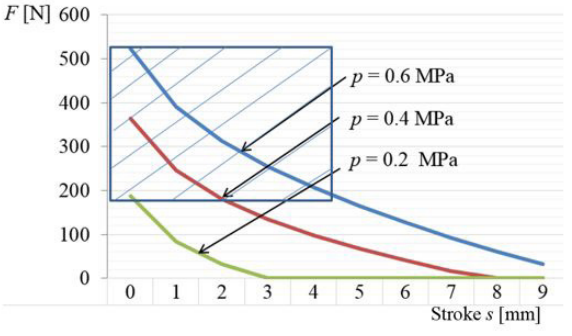

Fig. 3. *Variation of the developed force versus the charging pressure and stroke*

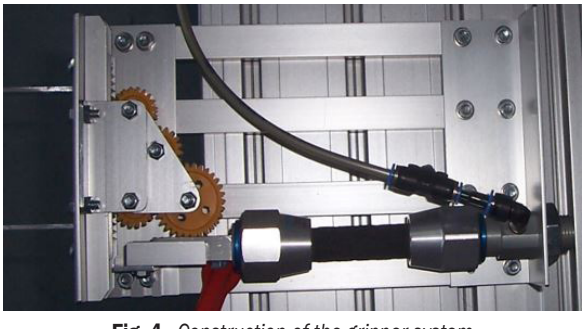

Fig. 4. *Construction of the gripper system*

Using rotational potentiometers, the reference module can generate up to six different values of the reference voltage, which are transmitted in form of signals to the proportional pressure regulator. If none of these reference values is used, the signal transmitted

to the pressure regulator is a voltage adjustable via an external potentiometer. The continuous adjustment of the air pressure allows for modifying the compliance of the entire system.

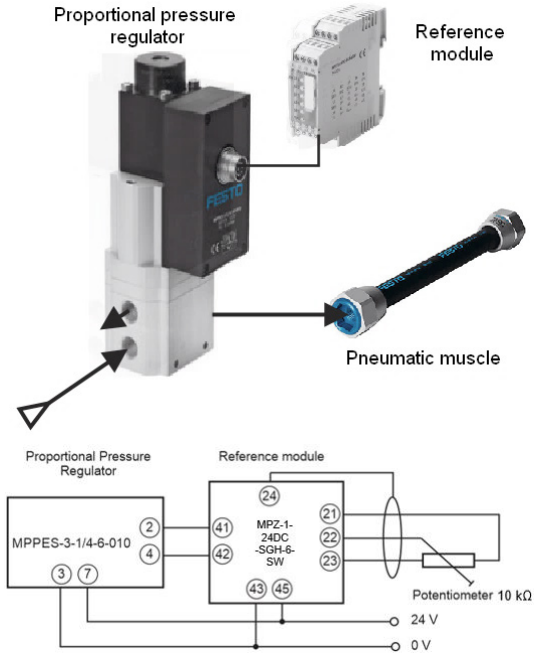

Fig. 5. *Control of the gripper system by means of a proportional pressure regulator*

The structural and block diagrams of the gripper system are presented in Fig. 6.

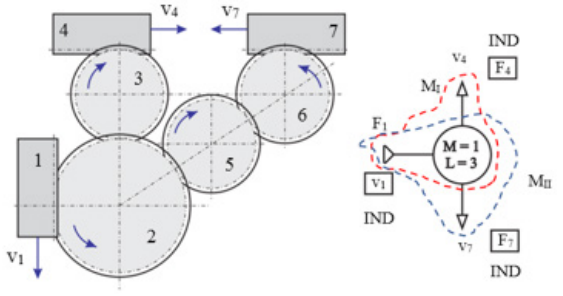

Fig. 6. *Structural and block diagrams of the gripper system*

The mechanism consists of two parallel-connected linkages (M_I and M_{II}) that branch out at gear 2. The motion of the entire system is generated by the pneumatic muscle and is characterized by a velocity (v_1) and a force (F_1) of the same orientation. The system outputs are its exterior links to the gripper jaws, and are characterized each by a velocity (v_4 and v_7) and a force (F_4 and F_7), of opposite directions.

The characteristics of the gears and racks used in the construction of the gripper system are: racks 4 and 7: module = 1 mm; number of teeth of the gears: z_2 = 30; $z_3 = z_5 = z_6 = 20$.

If the friction occurring in the mechanism is not neglected, the efficiency of each gear has to be included in the computation of the transmission function of the forces. The following efficiencies were considered for the analysed gripper system: $\eta_{12} = \eta_{34} = \eta_{67} = 0.97$; $\eta_{23} = \eta_{25} = \eta_{56} = 0.95$.

According to how the mechanisms are linked, the analysed gripper system is a mixed type aggregate, in which the two series-type mechanisms M_I and M_{II} are parallel connected starting from the power node at gear 2. As the number of mechanisms composing the two branches is not equal, the studied aggregate is of the non-homogeneous mixed type. An energetically equivalent homogenous diagram can with associated to this aggregate, presented in Fig. 7. The power at the system input is denoted by N, while $N_{u1,2}$ are the useful powers obtained at the outputs of the branches of the aggregate.

The efficiency of the gripper system was determined by matrix calculus. An array containing the coefficients β associated to the distribution onto branches of the output powers, and the partial efficiencies ordered by the connection of the component linkages was attached to the analysed mechanism. This array is called an associated matrix and takes the form of Eq. (2) for the studied aggregate:

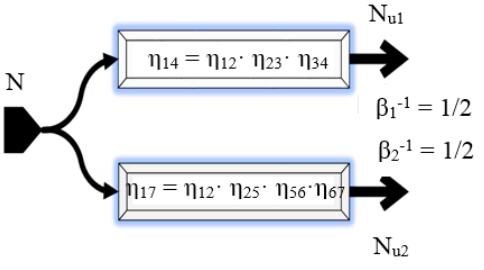

Fig. 7. *Homogenous diagram associated to the gripper system*

$$\left[M_\beta\right] = \begin{bmatrix} \beta_1^{-1} & \eta_{12}^{-1} & \eta_{23}^{-1} & \eta_{34}^{-1} & 1 \\ \beta_2^{-1} & \eta_{12}^{-1} & \eta_{25}^{-1} & \eta_{56}^{-1} & \eta_{67}^{-1} \end{bmatrix}. \quad (2)$$

The number of rows of the matrix corresponds to the branches of the aggregate, while the number of columns is that of the maximum number of gears included by the branches +1. Thus, a 2×5 matrix resulted. Based on this matrix, the efficiency of the aggregate can be determined by Eq. (3):

$$\left[\eta^{-1}\right] = \sum_C \left(\prod_l \left[M_\beta\right] \right), \quad (3)$$

where the following two operators have been introduced:

- Product by row operator $\prod_{l}\left[\mathrm{M}_{\beta}\right]$:

$$\prod_{1}\left[\mathrm{M}_{\beta}\right]=\begin{bmatrix}\beta_{1}^{-1}\cdot\eta_{12}^{-1}\cdot\eta_{23}^{-1}\cdot\eta_{34}^{-1}\cdot 1\\ \beta_{2}^{-1}\cdot\eta_{12}^{-1}\cdot\eta_{25}^{-1}\cdot\eta_{56}^{-1}\cdot\eta_{67}^{-1}\end{bmatrix}. \tag{4}$$

- Sum by column operator $\sum_{C}$:

$$\sum_{C}\begin{bmatrix}\beta_{1}^{-1}\cdot\eta_{12}^{-1}\cdot\eta_{23}^{-1}\cdot\eta_{34}^{-1}\cdot 1+\\ \beta_{2}^{-1}\cdot\eta_{12}^{-1}\cdot\eta_{25}^{-1}\cdot\eta_{56}^{-1}\cdot\eta_{67}^{-1}\end{bmatrix}. \tag{5}$$

By entering the values of the efficiencies of each elementary mechanism, the efficiency of the system will be computed in the following steps:

$$\left[\mathrm{M}_{\beta}\right]=\begin{bmatrix}0.5 & 0.97^{-1} & 0.95^{-1} & 0.97^{-1} & 1\\ 0.5 & 0.97^{-1} & 0.95^{-1} & 0.95^{-1} & 0.97^{-1}\end{bmatrix},$$

$$\prod_{l}=\begin{bmatrix}0.5\cdot 0.97^{-1}\cdot 0.95^{-1}\cdot 0.97^{-1}\cdot 1\\ 0.5\cdot 0.97^{-1}\cdot 0.95^{-1}\cdot 0.95^{-1}\cdot 0.97^{-1}\end{bmatrix}=\begin{bmatrix}0.5593\\ 0.5888\end{bmatrix},$$

$$\sum_{C}\left(\prod_{l}\left[\mathrm{M}_{\beta}\right]\right)=\left[0.5593+0.5888\right]=1.1481,$$

$$\rightarrow\eta=1.1481^{-1}=0.8709.$$

Knowing the value of the theoretical global efficiency, the equilibrium of powers can be written in the form of Eq. (6):

$$F_{1}\cdot v_{1}\cdot\eta+F_{4}\cdot v_{4}+F_{7}\cdot v_{7}=0, \tag{6}$$

where from follows the transmission function of the forces:

$$F_{1}=\frac{1}{\eta}\left(-F_{4}\cdot\frac{v_{4}}{v_{1}}-F_{7}\cdot\frac{v_{7}}{v_{1}}\right)=$$
$$=\frac{1}{\eta}\left(-F_{4}\cdot\frac{1}{i_{14}}-F_{7}\cdot\frac{1}{i_{17}}\right)=\frac{1}{\eta}\left(F_{4}-F_{7}\right),$$
$$\rightarrow F_{1}=\frac{F_{4}-F_{7}}{0.8709}. \tag{7}$$

3 EXPERIMENTAL RESULTS

The experimental research was focused on the study of the entire assembly, such as to determine the force generated at the jaws and the compliance of the system.

The maximum force that can be developed by one jaw was measured by the attached force sensor (Fig. 8).

The magnitude of this force depends, as was the case of the jaw's stroke, not only on the pressure but also on the direction of pressurization (increasing/inflation or decreasing/deflation). Fig. 9 shows the evolution of the force developed by a jaw versus pressure, when the pneumatic muscle is charged (inflated) and discharged (deflated), respectively.

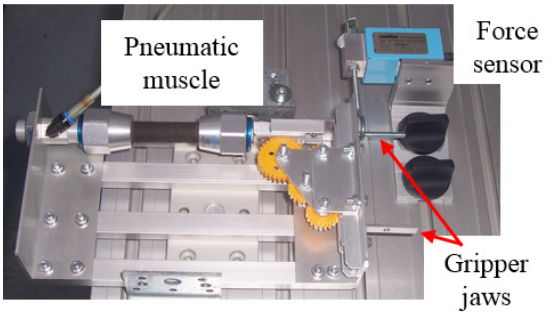

Fig. 8. *Force measurement developed by one jaw*

The graphs reveal a strong hysteresis type behaviour of the developed force. It can be observed that during the charging of the muscle the force starts increasing only beyond 1.318 bar pressure, and reaches its maximum of 83.33 N at 6 bar.

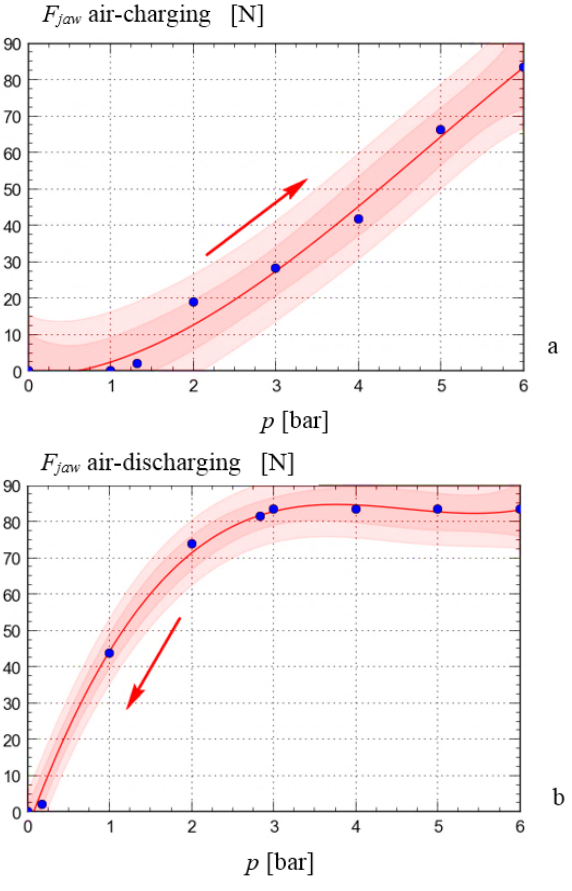

Fig. 9. *The force developed by one jaw for pressure: a) charging, and b) discharging*

During the discharging of the muscle, the force at first holds its maximum value, and starts decreasing only beneath 2.9 bar pressure, reaching 0 N at 0.15 bar.

The occurrence of hysteresis during operation is a major disadvantage of pneumatic muscles. In essence, hysteresis is a loss of energy, and a source of error difficult to control in a system that requires high positioning accuracy.

The hysteresis of pneumatic muscles is caused by the deformation of the elastic tube, as well as by the internal friction between each aramid fibre and its elastic envelope. These phenomena generate a so-called threshold pressure that translates into a stay (stagnation) of the pneumatic muscle's axial deformation, even if the feed pressure varies.

The hysteresis of pneumatic muscles increases the non-linearity of the systems in which they are included and adds to the complexity of the control systems.

In the case of the analysed gripper system of interest is the curve corresponding to the inflation of the pneumatic muscle, i.e. when the standard phases of the gripping process described in Fig. 1 are carried out. The threshold pressure (at 1.318 bar) narrows the useful area of the working pressures: only after this threshold value is exceeded will the gripping force move away from zero thus allowing the seizing of the targeted object.

The second curve corresponding to the deflation of the pneumatic muscle has an insignificant influence on the gripping process. It can be noticed that while the pressure decreases from 6 bar to 2.9 bar the force exerted by the jaw does not change (does not decrease); it is only beyond this value that the object is released. Thus, there is a certain delay (lag) in the system response (releasing of the object) to the command (decrease of the pressure).

Fig. 10 shows the variation of the force developed by one jaw versus its stroke. It can be noticed that at the beginning of the motion the force is maximum (83.33 N), and that it decreases as the jaw nears the end of its stroke.

Eq. (8) describes the regression function corresponding to the curve displayed above with a correlation coefficient of 0.999997:

$$F_{jaw} = 83.36 - 19.146 \cdot s + 0.7088 \cdot s^2, \qquad (8)$$

where s denotes the stroke of one jaw.

The obtained experimental results also allow the determination of the global efficiency of the analysed gripper system, to be matched against the theoretically

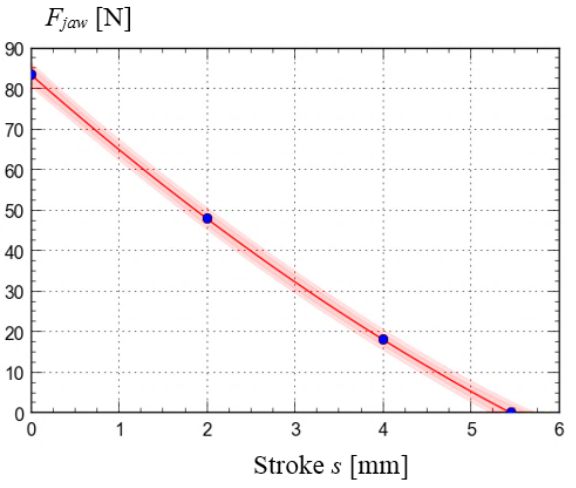

Fig. 10. *Variation of the force developed by one jaw versus its stroke*

computed value ($\eta_{theoretical} = 0.8709$). Thus, depending on the measured forces, the efficiency of the entire gripper system will be:

$$\eta_{real} = \frac{2 \cdot F_{jaw}}{F_i} = \frac{2 \cdot 83.33}{187.4} = 0.8893,$$

where F_i = 187.4 N is the value of the maximum force developed by the selected pneumatic muscle (measured value). This value of the efficiency is very close to the theoretically obtained one.

The stiffness k of the analysed system is computed by Eq. (9), and compliance C is determined as the inverse of stiffness.

$$k = -\frac{dF}{ds} = 19.146 - 1.4176 \cdot s, \qquad (9)$$

$$C = k^{-1} = \left(-\frac{dF}{ds} \right)^{-1} = \frac{1}{19.146 - 1.4176 \cdot s}. \qquad (10)$$

Fig. 11 presents the graphs of the stiffness and the compliance of the analysed gripper system. The concave shape of the curve describing the variation of the compliance ensures an enhanced growth of the compliance towards the end of the jaws' stroke, exactly at the beginning of contact with the gripped object and in accordance with the requirements specified in Fig. 1. The compliance of the gripper system grows as the stroke of the jaw advances, thus ensuring safe and soft gripping, without the risk of deforming the seized object.

Fig. 12 illustrates the dependence of the gripper system stiffness and compliance on the stroke of one jaw and on the air pressure. According to these

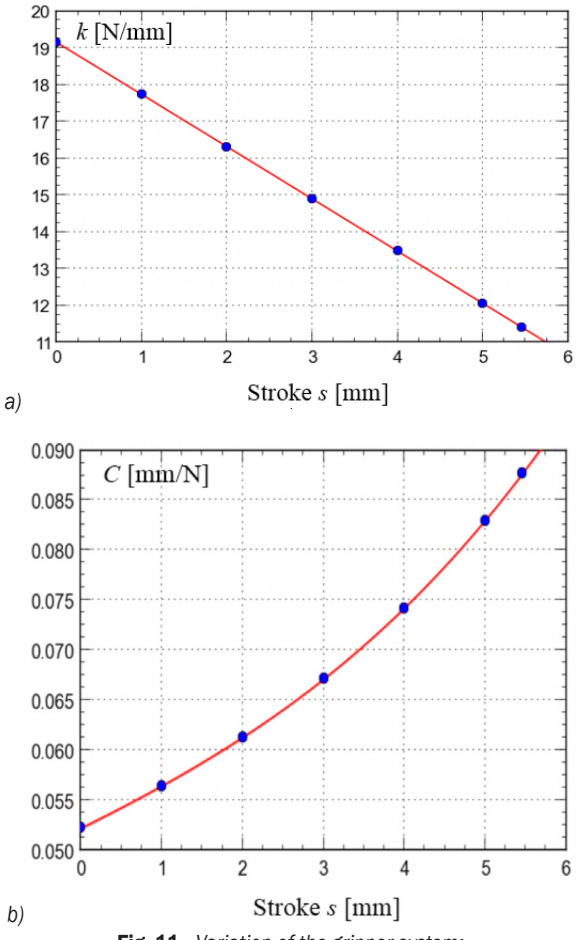

Fig. 11. *Variation of the gripper system: a) stiffness and b) compliance*

figures, the studied gripper system is characterized by decreasing stiffness and increasing compliance as the jaw's stroke advances and pressure grows. Such an evolution of stiffness and compliance results in a longer response time of the system to load variations, and evidently in smaller accuracy, which may represent an inconvenience. In contrast, in applications where system rigidity is less important, the main requirement being that of safe handling of the gripped object, the possibility of adjusting compliance so that it increases with pressure most certainly represents and advantage.

The functions describing the stiffness and the compliance of the studied gripper are:

$$k = 19.146 - 0.000346 \cdot p - 1.417 \cdot s, \quad (11)$$

$$C = 0.0522 + 0.00011 \cdot p + 0.00232 \cdot s + \\ + 0.000132 \cdot p^2 + 0.000581 \cdot s^2. \quad (12)$$

The concrete data collected by the conducted measurements further allow defining intervals of

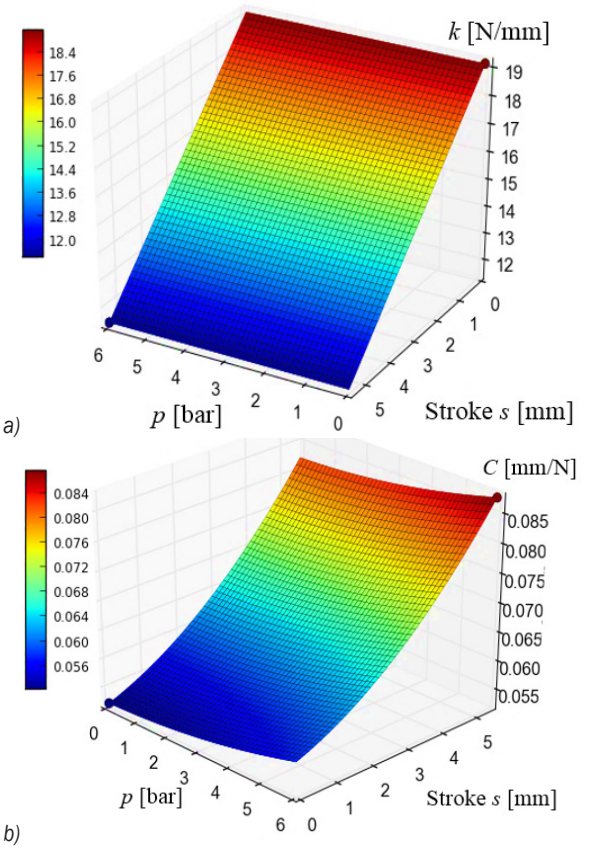

Fig. 12. *Variation of the gripper system a) stiffness and b) compliance versus pressure and stroke*

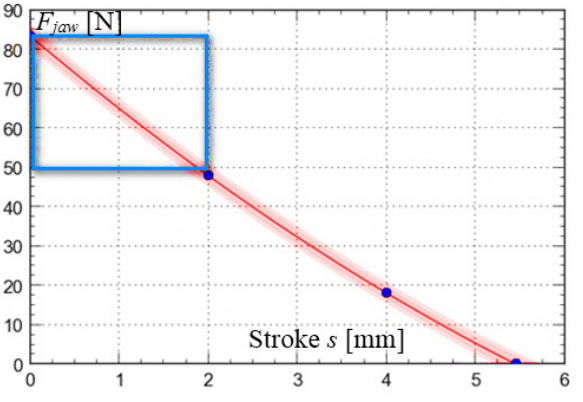

Fig. 13. *Identification of the area of interest in the deployment of the gripper system*

forces and strokes of the jaw, recommended for the deployment of the gripper system.

Thus, Fig. 13 presents the curve describing the variation of the force developed by one jaw versus its stroke. An area of interest is identified in this diagram where forces ranging from 50 to 83.33 N are obtained, at jaw strokes up to 2 mm.

For this functional area, the masses of the objects that can be seized range from 0.4 kg (for a 2-mm stroke) to 0.7 kg (for a 0-mm stroke).

4 CASE STUDY

Fig. 14 presents the case of assembling a non-chamfered peg into a chamfered hole, the two components being axially misaligned.

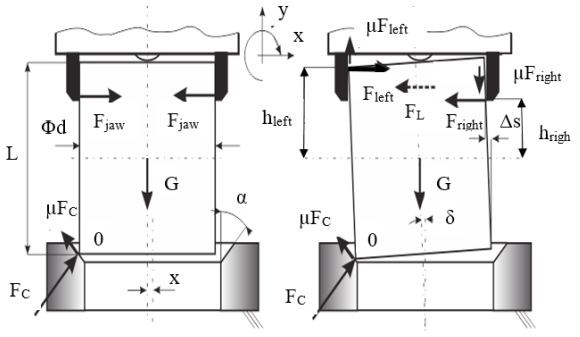

Fig. 14. *Assembling of radially misaligned components*

The peg is moved to the assembly zone by the jaws of the gripper system, until its edge touches the surface of the hole's chamfer. At this point, a contact force F_C is generated that tends to rotate the peg so as to allow assembly. This is not achievable unless the peg's gripper system is a compliant one, as is the one actuated by pneumatic muscles.

The tilt of the peg of angle δ causes additional forces to appear at the jaws, denoted by F_{left} and F_{right}. It is their cumulative effect ($F_L = F_{left} - F_{right}$) that allows a small displacement (Δs) of the two jaws, and consequently the turning of the peg by angle δ. In order to determine the additional displacement Δs of the two jaws, the following numerical case will be considered: $d = 47$ mm; $L = 50$ mm; $\alpha = 45°$; $m = 0.7$ kg; $g = 9.81$ m/s^2; $\mu = 0.2$; $h_{left} = 25$ mm; $h_{right} = 15$ mm.

Furthermore, the equations of equilibrium of the forces and torques developed in the system are written:

$$\sum F_x = 0;$$
$$F_C \cdot \cos\alpha - \mu \cdot F_C \cdot \sin\alpha + F_{left} - F_{right} = 0, \quad (13)$$
$$\sum F_y = 0;$$
$$F_C \cdot \sin\alpha + \mu \cdot F_C \cdot \cos\alpha + \mu \cdot F_{left} - \mu \cdot F_{right} - G = 0, \quad (14)$$
$$\sum M_0 = 0;$$
$$F_{left}\left(h_{left} + \frac{L}{2}\right) + G\frac{d}{2} - F_{right}\left(h_{right} + \frac{L}{2}\right) + \mu \cdot F_{right} \cdot d = 0. \quad (15)$$

For the above input data, the following results were obtained upon solving of the system of equations: $F_{right} = 5.3$ N; $F_{left} = 0.02$ N; $F_L = F_{left} - F_{right} = -5.28$ N.

The resulting lateral force F_L is the one that allows a small displacement (retraction) of the system's jaws. Thus, the clamping force of the handled object is slightly diminished, and the peg, due to its own weight and the pushing force developed by the gripper system is introduced into the hole.

Starting from Eq. (10) the additional displacement of the jaws can be determined. This is computed by Eq. (16):

$$\Delta s = \frac{F_L}{19.146 - 1.4176 \cdot s}. \quad (16)$$

Fig. 15 shows the corresponding graph.

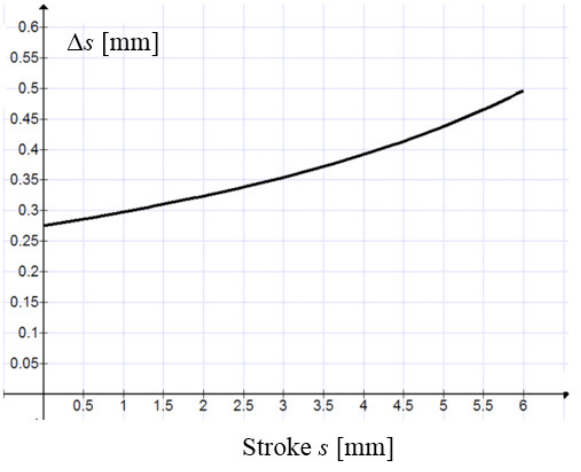

Fig. 15. *Magnitude of one jaw's radial displacement versus its stroke*

The conclusion following from the above graph is, that as the stroke carried out by the jaw becomes greater and implicitly the system's compliance grows, the additional displacements can be correspondingly greater. This allows working with a lesser positioning accuracy of the robot and with increased misalignments of the mating components, without compromising the assembling process.

5 CONCLUSIONS

The obtained experimental results reveal that the analysed gripper system is characterized by a behaviour strongly affected by hysteresis. The hysteresis of the pneumatic muscle is caused by the friction occurring between the enveloping tissue and the elastic tube, by the inner friction between

the threads of the enveloping tissue, as well as by the non-elastic deformation of the inner tube. This disadvantage carried by the behaviour of the entire system renders pneumatic muscle based actuations feasible only when the required precision of the gripping is not very high.

The measurements yielded a non-linear dependency of the developed force on the displacement for this gripper system. This means that the system has adjustable compliance, which renders it eligible for assembling applications. In this case, when two parts to be assembled are not perfectly aligned, a compliant system, like the one presented and discussed in this paper, offers the benefit of behaviour adaptable to the given situation, allowing assembling without destroying the two components.

As a conclusion to the conducted research, it can be asserted that due to their specific behaviour pneumatic muscles represent a viable constructive alternative for modern gripper systems.

6 REFERENCES

[1] Fantoni, G., Gabelloni, D., Tilli, J. (2012). *How to Design New Grippers by Analogy, Report*. University of Pisa, Pisa.

[2] Negrea, D., Deaconescu, T., Deaconescu, A. (2014). Symmetrical pneumatic muscle actuated gripper system with two mobile jaws. *Applied Mechanics and Materials*, vol. 541-542, p. 852-856, **DOI:10.4028/www.scientific.net/AMM.541-542.852**.

[3] Stăncescu, C. (2009). *Theoretical and Experimental Study of Grippers Systems with Jaws used in Industrial Robots*. PhD thesis, Transilvania University of Braşov, Braşov.

[4] Van Ham, R., Sugar, T.G., Vanderborght, B., Hollander, K.W., Lefeber, D. (2009). Compliant Actuator Designs. *IEEE Robotics & Automation Magazine*, vol. 16, no. 3, p. 81-94, **DOI:10.1109/MRA.2009.933629**.

[5] Petkovic, D., Isac, M., Pavlovic, N.D., Zentner, L. (2012). Passively adaptive compliant gripper. *Applied Mechanics and Materials*, vol. 162, p. 316-325, **DOI:10.4028/www.scientific.net/AMM.162.316**.

[6] Deimel, R., Brock, O. (2013). A compliant hand based on a novel pneumatic actuator. *IEEE International Conference on Robotics and Automation*, **DOI:10.1109/ICRA.2013.6630851**.

[7] Christopoulos, V.N., Schrater, P.R. (2009). Grasping objects with environmentally induced position uncertainty. *PLoS Computational Biology*, vol. 5, no. 10, p. 538, **DOI:10.1371/journal.pcbi.1000538**.

[8] Ciocarlie, M., Hicks, F.M., Stanford, S. (2013). Kinetic and Dimensional Optimization for a Tendondriven Gripper. *IEEE International Conference on Robotics and Automation.*

[9] Dollar, A.M., Howe, R.D. (2010). the highly adaptive SDM hand: design and performance evaluation. *The International Journal of Robotics Research*, vol. 29, no. 5, p. 585-597, **DOI:10.1177/0278364909360852**.

[10] Monkman, G.J., Hesse S., Steinmann, R., Schunk, H. (2007). *Robot Grippers*. Wiley-VCH Verlag, Weinheim.

[11] Deaconescu, A., Deaconescu, T. (2011). Bio-inspired pneumatic muscle actuated robotic system. *Intelligent Automation and Systems Engineering*, Springer New York, p. 27-40, **DOI:10.1007/978-1-4614-0373-9_3**.

[12] Festo. Power Gripper, from *http://www.festo.com/net/SupportPortal/Files/156738/Brosch_FC_PowerGripper_EN_lo_L.pdf,* accessed on 2015-12-07.

[13] Negrea, D., Deaconescu, A., Deaconescu, T. (2014). Constructive and functional modelling of a pneumatic muscle actuated symmetric gripper system with two mobile jaws. *Applied Mechanics and Materials*, vol. 657, p. 574-578, **DOI:10.4028/www.scientific.net/AMM.657.574**.

[14] Deaconescu, T., Deaconescu, A. (2015). Structural, kinematic and static modelling of a pneumatic muscle actuated gripper system. *Applied Mechanics and Materials*, vol. 811, p. 318-322, **DOI:10.4028/www.scientific.net/AMM.811.318**.

[15] Bicchi, A., Tonietti, G. (2004). Fast and soft arm tactics: dealing with the safety-performance trade-off in robot arms design and control. *IEEE Robotics and Automation Magazine*, vol. 11, no. 2, p. 22–33, **DOI:10.1109/MRA.2004.1310939**.

Strojniški vestnik - Journal of Mechanical Engineering 63(2017)4, 235-247
DOI:10.5545/sv-jme.2016.4258
Original Scientific Paper
Received for review: 2016-12-12
Received revised form: 2017-02-06
Accepted for publication: 2017-02-14
© 2017 Journal of Mechanical Engineering. All rights reserved.

Performance Index in MHD Duct Nanofluid Flow Past a Bluff Body at High Re

Kozhikkatil Sunil Arjun* – Rakesh Kumar
Department of Mechanical Engineering, Indian Institute of Technology (ISM), India

The quasi-two-dimensional Al_2O_3-water nanofluid magneto hydro-dynamics (MHD) flowing over a circular cylinder at higher Reynolds number has been modelled using Ansys FLUENT 15.0 in a rectangular duct to determine the viability of heat transfer enhancement. The effect of the numerical simulations on performance indices were analysed for the range of $1000 \le Re \le 3000$ Reynolds numbers, $10 \le Ha \le 100$ modified Hartmann numbers, $0.5 \le \varphi \le 2$ nanoparticle volume concentrations, $0.1 \le \beta \le 0.4$ blockage ratios, $1 \le \gamma \le 0.25$ position ratios, $0.75 \le G/d \le 1.5$ gap ratios and $0 \le d \le 10$ distance downstream of cylinder along heated duct wall. The results are presented graphically and discussed quantitatively. Grid independence is achieved with the domain having 3 upstream and 20 downstream cylinder diameter distance lengths with element polynomial degree 7 with respect to mean drag coefficient and Strouhal number. Cylinder placement with gaps to the heated wall of diameters between 0.75 and 1.25 and 10 diameters downstream of cylinder performed best, achieving 117 % enhancement of the performance indices at $Re = 3000$, $Ha = 20$, $\varphi = 2$ %, $\beta = 0.4$, $\gamma = 1$ and $G/d = 1$. The performance indices were greater than one for all the cases tested, which indicates that the heat transfer enhancement for this flow is viable. The Nusselt number values of the present study were compared with the analytical and experimental data published earlier and found to be in perfect agreement validating the reliability of the present model.

Keywords: computational fluid dynamics, heat transfer enhancement, bluff body, circular cylinder, magneto hydro-dynamics

Highlights

- *A very high performance index enhancement is achieved, incorporating the impacts of Re, Ha and φ in rectangular duct flow.*
- *A circular cylinder is used as bluff body in MHD nanofluid flow at higher Reynold numbers.*
- *Ideal cylinder placement conditions of blockage, position and gap ratios are proposed.*
- *Viable heat transfer enhancements analysed using numerical simulations and the resulting quasi-2D model predictions are validated.*

0 INTRODUCTION

Flow around bluff bodies such as circular and elliptical cylinders is a fundamental fluid mechanics problem. Many engineering applications, such as off-shore structures, bridge piers and pipelines, can be modelled as circular cylinders. However, flow over complex bodies, such as wings, submarines, missiles, and rotor blades, in which the parameters such as axis ratio, the angle of attack, and initial velocity profile, can influence the flow characteristics of the wake, nature of separation, and forces (drag and lift force); such type of flow can be modelled as an elliptical cylinder. Elliptic cylinders have the general fluid dynamic features between those of a circular cylinder and a flat plate. When a flow goes across a circular cylinder, complex flow phenomena and behaviours near the cylinder surface and the wake region, such as flow separation, vortex shedding and shear-layer instability are induced in different regimes of Reynolds numbers. These flow phenomena would inevitably apply unsteady lift and drag forces to the cylinder and play a very significant role in engineering applications. The dynamics of flow around a cylinder depend on the Reynolds number and external forces, such as magnetic field. Effective medium theories have proved that thermal conductivity of nanoparticles is very much greater than that of micro particles. The heat transfer methods with performance indices greater than one would be feasible choices in practical applications as it is more in the favour of heat transfer enhancement rather than in the favour of the pressure drop increasing.

At lower *Re,* the wake length increases linearly with *Re* and the development of drag coefficient, the angle of separation, pressure and vorticity distributions over the cylinder surface with *Re* is consistent, but is too slow at higher *Re*, for steady incompressible flow around a circular cylinder [1]. The rate of forced convection heat transfer in the steady cross-flow regime over unconfined circular cylinder increases with an increase in *Re* and *Pr* with a higher value for uniform heat flux condition than that of the constant wall temperature [2]. When the imposed flow is oriented normal to the direction of gravity and assumed to be steady, mixed convection distorts streamline and isotherm patterns and increases the drag coefficient as well as the rate of heat transfer from the circular cylinder immersed in power law fluids [3]. As the spin ratio increases in a counter-

*Corr. Author's Address: Department of Mechanical Engineering, Indian Institute of Technology (ISM), Dhanbad, India, arjun@mece.ism.ac.in

clockwise rotation of cylinder at $Re = 1.4 \times 10^5$, the lift coefficient increases while the drag coefficient and mean pressure coefficient reduces, the lower vortex diminishes and finally disappears [4].

High Re flow (1×10^6 to 3.6×10^6) around a smooth circular cylinder by using 2D standard k–ε model and coefficient of drag, lift and Strouhal number predictions were acceptable [5]. The Spalart-Allmaras (S-A) and realizable k–ε (RKE) turbulence models are not suited for the near wake region of circular cylinder flow with a high level of separation at $Re = 41300$, while the Wilcox K Omega (WKO) and Menter's Shear Stress Transport (SST) model predictions are in good agreement, and the use of SST turbulence model with a fine mesh near the wall predict more realistic and accurate results [6]. By using an easy unstructured mesh [7], the dense cells are meshed forcibly in the wake region of the turbulent flow around a circular cylinder. Using hybrid Reynods-Averaged Navier-Stokes (RANS) / large Eddy simulation (LES) Detached Eddy Simulation, Scale-Adaptive Simulation (DES, SAS), the model showed good agreement for the Strouhal number, more realistic agreement than S-A, SST Unsteady Reynods-Averaged Navier-Stokes (URANS) with respect to the coefficient of pressure, recirculation length, bubble size, and the average turbulent kinetic energy. The blending parameter, which allows a smooth passing with RANS/LES (fluctuation correction) hybrid model for pressure distribution over the surface, and velocity field in the flow around a circular cylinder at Re 1.4×10^5 are in good agreement with experimental and other studies [8].

The acceptability of a LES mesh-free vortex method to simulate complex flow over a circular cylinder at Re ranging from 10^4 to 6×10^5 was investigated [9]. Using a combination of finite element method (FEM) and finite volume method (FVM), discretization on an unstructured grid with a variationally multi-scale (VMS) - LES model over a circular cylinder, [10] showed qualitative and quantitative acceptability at subcritical Re up to 2×10^5 for the Strouhal number, drag coefficient, and RMS coefficient of lift, as well as overall good agreement for the coefficient of pressure at the surface with overestimation at the stagnation point. The 2D URANS with eddy-viscosity based turbulence models were examined [11] over a circular cylinder at Re varying from 10^4 to 10^7, and it was concluded that the predictions are in a qualitative sense only and accurate prediction required a more sophisticated model. Using VMS-LES with a dynamic subgrid scale model for flows around a circular cylinder in subcritical regime at $Re = 2 \times 10^4$, [12], very good agreement of mean drag coefficient and Strouhal number was observed. Good agreement of mean recirculation length and root mean square (RMS) of the lift coefficient, and less discrepancy of mean pressure coefficient distribution at the cylinder show less discrepancy with experimental and other results.

Forced convective heat transfer was reported [13] using copper-water nanofluid over a circular cylinder at constant wall temperature. The steady axisymmetric mixed convection boundary layer flow past a thin vertical cylinder placed in a water-based copper nanofluid presents the existence of dual solutions when the surface of the cylinder is cooled [14]. Stabilized mixed convective flow using copper-water nanofluid flowing past a circular cylinder at constant wall temperature was reported [15]. Total entropy generation of nanofluids past a square cylinder in vertically upward flow decreases with increasing nanoparticle volume fractions and for mixed convection flows with nanofluids, thermal irreversibility is higher than frictional irreversibility [16]. The homotopy analysis method has excellent potential for simulating nanofluid dynamics problems for the laminar axisymmetric mixed convection boundary-layer nanofluid flow past a vertical cylinder [17]. In a steady, 3D stagnation point flow of a nanofluid past a vertical circular cylinder that has a sinusoidal radius variation, [18] and [19] it was found that the skin friction coefficient and the heat transfer rate at the surface are higher for copper–water nanofluid than alumina–water and titania–water nanofluids.

Heat transfer is enhanced with increasing frequency of oscillation, nanoparticle volume fraction and Re; the level of nonlinearity decreases with increasing ϕ and with decreasing Re in forced pulsating flow at a backwards facing step with a stationary cylinder [20]. Suppression of vortex shedding at $Ri \geq 0.15$ in water-based nanofluid past a square cylinder in vertically upward flow and the average Nu was found increasing with nanoparticle concentration [21]. Energy content in the mean mixed convective flow of the base fluid at Ri of 0.5 is found to be maximum compared to that of nanofluids past a square cylinder [22]. Increasing the value of non-uniform heat generation/absorption parameter in boundary layer nanofluid flow leads to deterioration in heat transfer over a stretching circular cylinder [23]. Proper solutions at each time step were obtained reaching steady state using an unsteady free convective boundary layer flow of a nanofluid over a vertical cylinder with an explicit finite-difference

scheme [24]. The energy content in the individual modes of mixed convective flow stability for Cu-water nanofluids past a square cylinder is found to be higher than that of Al_2O_3–water nanofluids [25].

A small control cylinder placed in turbulent wake of a much larger 2D bluff body can cause a significant increase in drag fluctuations and can occur on longer timescales than vortex shedding and reveal a bistable wake regime [26]. Flow around porous and solid cylinders with external magnetic fields showed a decline of critical Stuart number for suppressed vortex shedding with increasing Darcy numbers and the enhancement of Stuart number for the disappearance of the re-circulating wake with increased *Re* [27]. Three distinct regions observed among the bluff bodies of different shapes in the vertical axis wind/water turbine wake structure are similar: near wake, where periodic blade shedding dominates; transition region, where blade vortices decay and growth of shear layer instability occurs and far wake, where bluff body wake oscillations dominate [28].

Numerical simulations are necessary for many engineering applications, which operate at high-speed or in highly turbulent regimes, which are very difficult to model. Most of the computational works available in literature employ two-equation turbulence models for modelling due to their simplicity and reasonable accuracy. The absence of comprehensive data is observed in magneto hydro-dynamics (MHD) duct nanofluid flow past a circular cylinder as a bluff body. This study aims to establish the relationship between the size and position of the cylinder, magnetic field strength, Reynolds number, nanoparticle volume fraction and performance index for quasi-two-dimensional flow around circular cylinders, in which the parameters can influence the flow characteristics of the wake, nature of separation, drag, and lift forces.

1 GEOMETRY, BOUNDARY CONDITIONS AND SIMULATION

A circular cylinder with diameter d is placed in a rectangular duct with length 23 d and diameter 10 d ($2L$) with its axis parallel to a magnetic field with strength B at distance G from a heated sidewall of constant wall temperature T_w (Fig. 1), higher than the ambient temperature. The blockage ratio, $\beta = d/(2L)$ characterizes the size of the cylinder relative to the duct. The cylinder position is defined relative to the distance to the duct centreline as position ratio, $\gamma = G/(L\text{-}d/2)$. The value of position ratio varies between 1 when the cylinder is placed symmetrically between the sidewalls to 0 when it is in contact with the heated sidewall. The cylinder proximity to the heated wall is characterized better in terms of the gap ratio G/d. The induced magnetic field is assumed negligible.

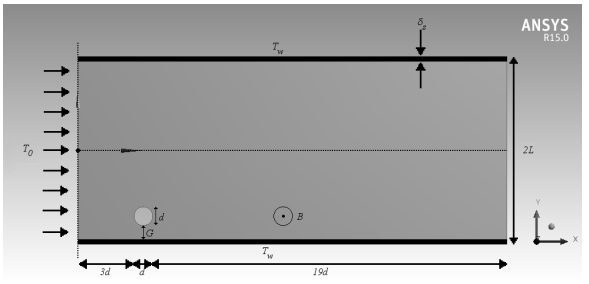

Fig. 1. *Geometry of rectangular duct showing Schercliff layer*

This produces dimensionless magneto hydrodynamic equations governing continuity, momentum, and energy expressed as:

$$\nabla \cdot u = 0, \tag{1}$$

$$\frac{\partial u}{\partial t} + \left(u \cdot \nabla\right) \cdot u + \nabla p = \frac{1}{Re} \nabla^2 \cdot u - \frac{Ha}{Re} \cdot u, \tag{2}$$

$$\frac{\partial T}{\partial t} + \left(u \cdot \nabla\right) \cdot T = \frac{1}{Pe} \nabla^2 \cdot T, \tag{3}$$

The terms describing the effects of viscous dissipation and Joule heating, as included in [29], are not considered in the energy equation here, following [30] to [32]. An order of magnitude calculation confirmed that their contributions were between 500 times and 10^7 times smaller than those of the included terms for applications considered in this study [33]. However, at applied magnetic fields, the destabilizing effect of shear generated at the sidewalls wins the competition with the damping effect by Joule's dissipation and turbulent side layers are created, as already reported [31]. The purpose of the present study is to investigate the effects of applied magnetic fields on the forced convection around a cylinder and as a result, the effect of buoyancy is ignored in the momentum equation of the present study and treated as a case of incompressible flow of constant thermodynamic and transport property for the Newtonian fluid, as reported earlier [32].

The volume fraction equation is solved for the secondary phase (nanoparticles). The concentration of the secondary dispersed phase (nanoparticles) is solved by a scalar equation, considering the correction made by phase slip. The governing equations of fluid flow and heat transfer for a multiphase Eulerian-Eulerian mixture model in dimensional form are utilized [34]. In the above equations, the velocity component of the mixture (nf) is treated as the product

of the mixture density and mass averaged mixture velocity. The mixture momentum is obtained by summing the individual momentum equations of every phase. The energy of the mixture is calculated from the effective thermal conductivity of the mixture. The velocity of the secondary phase (s) is the sum of drift velocity for the secondary phase and mass averaged mixture velocity. The velocity of the secondary phase in relation to the primary phase (f) is known as the relative or slip velocity and is calculated as its difference. The drift velocity, slip velocity and drag function are calculated as per the standard equations proposed by **[35]** and **[36]**.

The Reynolds number is the ratio of inertial to viscous forces and is defined as:

$$Re = u_0 \frac{d}{v}. \tag{4}$$

The Hartmann number is the square root of the ratio of electromagnetic to viscous forces and is defined as:

$$Ha = aB\sqrt{\frac{\sigma}{\rho v}}. \tag{5}$$

The local Nusselt number along the heated sidewall (x) of the duct after time t is defined as

$$Nu_w(x,t) = \frac{d}{Tf - Tw}\frac{\partial T}{\partial y}\Big/_{\text{wall}}. \tag{6}$$

T_f is the bulk fluid temperature calculated using the velocity and temperature distribution as

$$T_f(x,t) = \frac{\int_{-L}^{L} uTdy}{\int_{-L}^{L} udy}. \tag{7}$$

The heat transfer improvement and the pressure drop penalty on the duct are considered together for better quality and expressed as the performance index defined as:

$$\eta = \frac{\dfrac{Nu}{Nu_0}}{\dfrac{\Delta P}{\Delta P_0}}, \tag{8}$$

where Nu/Nu_0 and $\Delta P/\Delta P_0$ are the heat transfer enhancement ratio and pressure penalty ratio. Nu and ΔP are the overall Nusselt number and pressure drop across the duct where a circular cylinder is shifted from the channel centreline; and Nu_0 and ΔP_0 are the overall Nusselt number and pressure drop without a cylinder.

ANSYS FLUENT 15.0 is used for simulation. A nodal spectral-element method is utilized to discretise the governing flow and energy equations in space, and a third-order scheme based on backwards differentiation is employed for time integration **[37]**. The setup of the system is the same as that described in **[33]**. The flow is quasi two-dimensional, consisting of a cold flow core region, where the velocity is uniform along the direction of the magnetic field **[38]** and variable-variance two-dimensional Gaussian-weighted summation of particles in the vicinity of each interpolation point **[39]**, a thin Hartmann layer at the wall perpendicular to the magnetic field and a thin Schercliff layer along the heated wall. A thorough description of this model is available in **[40]** and **[41]**.

The boundary conditions imposed on Eqs. (1) to (3) are as follows: a no-slip boundary condition for velocity is imposed on all solid walls. At the channel inlet, the analytical solution to Eqs. (1) and (2) for fully-developed flow in a channel without a cylinder is imposed **[42]** and **[43]**. At the exit, a constant reference pressure is imposed and a zero stream-wise gradient of velocity is weakly imposed through the Galerkin treatment of the diffusion term of the momentum equation **[44]**, **[39]** and **[45]**. The SIMPLE algorithm **[46]** has been adapted for the pressure velocity coupling. A high-order Neumann condition for the pressure gradient is imposed on the Dirichlet velocity boundaries to preserve the third-order time accuracy of the scheme **[37]**. The temperature of the incoming stream and the unheated top wall is taken as T_0, and at the bottom heated wall as T_w. The cylinder is thermally insulated (i.e. a zero normal temperature gradient is imposed at its surface).

The computational domain is divided into a non-uniform grid of quadrilateral elements, concentrated near the cylinder and the heated wall that experience high velocity gradients to capture the small-scale structures in the flow (Fig. 2). Within each element, a grid of interpolation points resolves the high-order tensor product of polynomial shape functions using the second order upwind scheme to describe flow fields. The asymmetrically positioned cylinder requires the creation of new meshes, and further grid-independence tests are performed to ensure that adequate spatial resolution is maintained for the simulations in this study.

A convergence study for spatial resolution has been performed by varying the element polynomial degree from 4 to 9, while keeping the macro element distribution unchanged. It is found that the results converge to within less than 0.5 % with polynomial order 7, which is used for the simulations reported in this study. Continuous phase modelling is followed in this study and the thermo-physical properties of base

fluid and nanoparticles are provided as in [47], and the classic formulae of [48] were used to determine the density and heat capacitance of nanofluids in this study.

A grid independence study is carried out for base fluid at Reynolds number 100. Three different combinations of grid with the Nusselt number have been considered to ensure the grid independence of the solution. The results of grid sensitivity analysis exhibited the *Nu* values of 0.8163, 0.821 and 0.8211 respectively for 100 × 50, 100 × 100 and 100 × 150 grids. Based on the results of grid sensitivity analysis, 100 × 100 grid has been selected to ensure consistent numerical results.

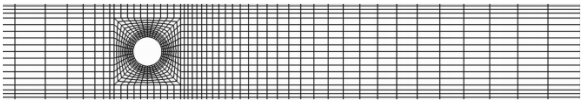

Fig. 2. *Spectral element mesh of the computational domain*

Grid independence study is conducted at $Re = 3000$, $Ha = 100$ and blockage ratio 0.4 for mean drag coefficient and the Strouhal number, which are sensitive to domain size. The meshes to model the placement of the cylinder at various domain lengths along the heated side wall are constructed. The domain length for downstream distance is made constant as 20 and that for upstream distance is varied. Values of mean drag coefficient and the Strouhal number resulting from the use of 2, 3 and 4 domain lengths for the upstream distance with 1188, 1472 and 1488 macro elements showed 1.659, 2.15 and 2.152 values for mean drag coefficient and 0.246, 0.262 and 0.262 values for Strouhal number, respectively. Thus, the second domain with 3 upstream and 20 downstream distance lengths is sufficient to resolve the flow.

2 RESULTS AND DISCUSSION

2.1 Effect of Nanoparticle Volume Fractions

The influence of Al_2O_3 nanoparticle volume fractions from 0.5 % to 2 % and *Re* from 1000 to 3000, when a circular cylinder is placed at the mid-plane of the rectangular duct with magnetic field strength of $Ha = 100$ is shown in Fig. 3. As the volume concentrations and *Re* increase, the performance indices also increase successively with the maximum value of 2.4 using 2 % Al_2O_3-water nanofluid at $Re = 3000$. The results are in agreement with the previous reports. The *Nu* increases as *Re* and the nanoparticle volume fraction increase over a stretching circular cylinder [49]. Heat transfer over a heated circular cylinder wall increases with an increase in particle fraction of copper-water nanofluid and *Re* at lower *Re* range [50]. 25 nm size (0.01 volume fraction) Al_2O_3 nanofluid with circular cylinder as the bluff body has the highest *Nu* compared to CuO, SiO_2, and TiO_2 nanofluids at low *Re* [51]. The heat transfer of nanofluid flow over a square cylinder increases with higher *Pe* and particle volume concentration, but with smaller particle diameter [52].

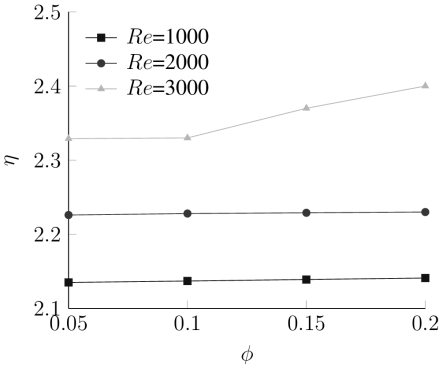

Fig. 3. *Effect of nanoparticle volume fractions on performance index at different Re*

2.2 Effect of Blockage Ratio and Position Ratio

The results (Fig. 4) demonstrate that the improvements in performance indices are much higher at higher blockage ratios (≥ 0.3) for all *Re* from 1000 to 3000 with the highest value of 2.29 for blockage ratio 0.4 at $Re = 3000$ using 2 % Al_2O_3-water nanofluid at $Ha = 100$. The performance indices were higher than 1.5 for blockage ratio 0.3 and higher than 2 for blockage ratio 0.4. As the position ratio decreases from 1 to 0.25, the performance index increases for all *Re* for blockage ratio 0.1. However, for blockage ratio 0.2, this increase is limited to position ratio 0.5; thereafter, it decreases up to position ratio 0.25 for all *Re*. For blockage ratio ≥ 0.3, it decreases as position ratio decreases for all *Re*. Performance indices increase as *Re* increases. Maximum performance index for heat transfer enhancement is augmented by 37 % through decreasing position ratio for a small blockage ratio, i.e. when the cylinder is close to the heated wall. As *Re* and blockage ratio increases, performance index also increases. The maximum performance index augmentation was higher than two-fold at the duct centreline. Proximity of the cylinder to the heated wall has significant influence on heat transfer and flow characteristics. The interaction of Schercliff layer with shear layers separating cylinder surface might be responsible for this observation.

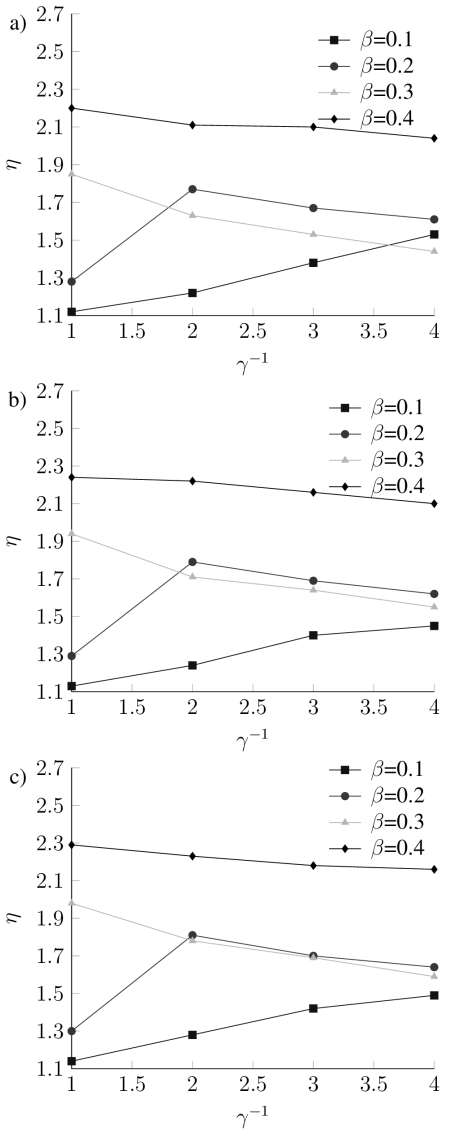

Fig. 4. *Effect of blockage and position ratio on performance index at Re a) 1000 b) 2000 c) 3000*

Similar results have been reported in literature. The transition from steady to unsteady flow regimes of a liquid metal past a circular cylinder in a rectangular duct is determined as a function of Ha, the blockage ratio, the Strouhal number, and heat transfer from heated wall to fluid **[33]** and downstream cross-stream mixing induced by cylinder wake found to increase heat transfer by two-fold. Variation in wake recirculation length in the steady flow regime of liquid metal flow under a strong axial magnetic field in a rectangular duct is determined as a function of *Re*, *Ha* and blockage ratio **[53]**. The blockage ratio controls fluid flow and heat transfer from the circular cylinder is confined between parallel planes and delays the separation **[54]**. Increasing *L*/*d* from 1 to 2 has insignificant lower effect on heat transfer and *Nu* of circular tube **[55]**. Vortex generators with height equal to half the boundary-layer thickness produce a significant delay of separation and 60 % drag reduction in incompressible steady flow past a circular cylinder in a transcritical flow regime, with turbulent boundary layers ahead of separation **[56]**.

As the immersion level ratio of a horizontal circular cylinder in shallow water increases, the magnitude of jet-like flow velocity goes up and result a difference between primary and developing circulation bubble and this stimulates the momentum transfer between the core and wake flow region **[57]**. A 30 % frequency was reduced independent of *Re*, downstream of a circular cylinder, and shear layers were elongated in wake so that the Karman vortex street was not developed in water flow; and vortex formation length was considerably extended downstream of cylinder and peak magnitudes of turbulence parameters were comparably smaller **[58]**. 3D unsteady LES shows the broadband nature of shear-layer instability behind a circular cylinder and the dependence of shear-layer frequency on high *Re* **[59]**. When a nonlinear optimal control free-stream velocity is applied, vortex shedding was suppressed in incompressible flow past a circular cylinder up to $Re=1000$ with a 70 % drag reduction **[60]**. The correlation coefficient of a circular cylinder bluff body placed inside a circular pipe in a fully developed turbulent regime improves with an increase in blockage ratio **[61]**.

2.3 Effect of Gap Ratio

When the cylinder approaches the heated wall (small gap ratio), the performance indices decrease at all blockage ratios and *Re* than its magnitude when the cylinder is located at the duct centreline. This enhancement might be due to the increased velocity of the flow near the heated surface caused by the wake vortices leading to effective mixing taking place in the flow core. It is also observed from Fig. 5 that when the cylinder is further away from both the heated wall and mid-plane, performance indices decrease for a particular blockage ratio and *Re*. The performance indices at gap ratio 0.75 and 1.25 are at par. From Figs. 3 and 4, the performance indices were greater than 1 for all the cases tested, which indicates that the heat transfer enhancement for this flow is viable. The highest performance index of 2.4 is recorded for the highest blockage ratio when the cylinder is located at the duct centreline.

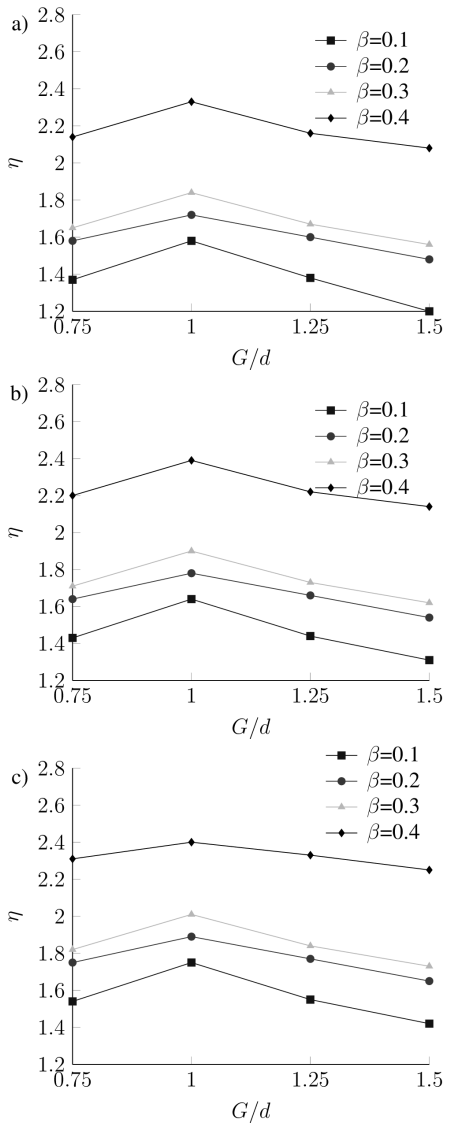

Fig. 5. *Effect of blockage and gap ratio on performance index at Re a) 1000, b) 2000 c) 3000*

Cylinder placement with gap ratios between 0.75 and 1.25 diameters performed best, achieving a 100 % performance index enhancement for the highest blockage ratio. These gap ratios corresponded to deviation of cylinder from the wake centreline of counter rotating vortex pairs that carry hot fluid farther. In the present study, the duct geometry is wide enough to accommodate the cylinder with high blockage ratio at these optimal gap ratios without crossing the aforesaid centreline showing performance indices higher than 2 in all cases (Fig 4). This trend is repeated for all blockage ratios including the smallest one. The highest performance indices were consistent for gap ratio one for all blockage ratios. Thus, the assumptions for the quasi 2D nature of the model is proved.

Non-monotonic dependence of critical *Re* along the circular cylinder placed symmetrically in a rectangular duct for vortex shedding with respect to *Ha* and onset of new flow regime based on quasi-2D simulations are confirmed earlier [62]. The drag coefficient increases as G/d increases and for $G/d=0.3$, the influence of the gap becomes negligible [63]. For a small gap, the pressure coefficient around the cylinder is asymmetric and results a net upward lift force on the cylinder, for an intermediate gap ($G/d=0.25$). The pressure coefficient is symmetric and causes a negative mean lift force on the cylinder; for large gaps, the pressure coefficient is again symmetric and the mean lift force approaches zero. Circular cylinder placement in conducting fluid flows within a strong transverse magnetic field with gaps to the heated duct wall between 0.83 and 1.4 diameters performed best. This leads to achieving at least 95 % of the peak efficiency indices for each blockage ratio with heat transfer enhancement of up to 48 % compared to the centreline placement and only a modest increase in pressure head losses from cylinder drag [30].

2.4 Effect of Position of Cylinder along Duct Wall

The performance index at position along the heated duct wall is depicted in Fig. 6, which shows that as the distance downstream of cylinder increases from 0 to 20, the performance indices increases up to 10 *d* and thereafter decreases for all *Re*.

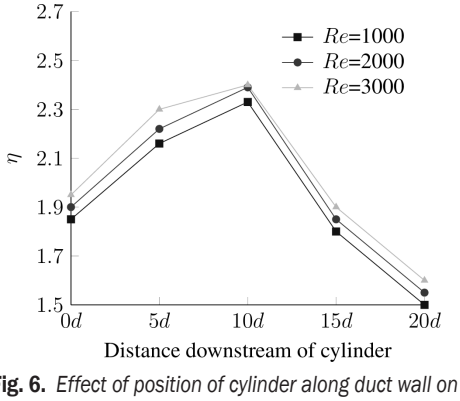

Fig. 6. *Effect of position of cylinder along duct wall on performance index at different Re*

As *Re* increases from 1000 to 3000, the performance indices also increase with the maximum value recorded for *Re* = 3000 at 10 *d* downstream of cylinder. This region from the cylinder to distance 10 *d* downstream of cylinder, where a successive

increase in performance index corresponds to a strong interaction region of the heated Shercliff layer vorticity and cylinder wake vorticity. Beyond this region, the placement of the cylinder was not distinguishable in all *Re*, which might be due to the non-interaction of wake and Shercliff layers. Due to rotational oscillation of the cylinder in MHD flow of fluid in a rectangular duct, maximum heat transfer enhancement of more than 30 % from the heated channel wall over a zone extending 10 diameters downstream of the cylinder is reported [64].

2.5 Effect of magnetic field strength

As the magnetic field strength is varied from *Ha* 10 to 100 with blockage ratio 0.4, position ratio = 1 and gap ratio 0.75 with the circular cylinder placed 10 diameters distance downstream of the cylinder at *Re*=3000; *Ha*=20 recorded best performance index of 2.426 (Fig. 7). A higher value at *Ha*=10 and a lower value at *Ha*=50 are also recorded.

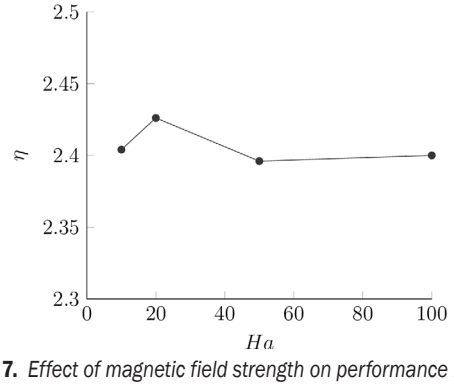

Fig. 7. *Effect of magnetic field strength on performance index*

The *Nu* decreases as the magnetic parameter increases over a stretching circular cylinder [49]. In the presence of the magnetic field, the near wall velocity gradients increase, enhancing the slip velocity at the pipe walls and thus the heat transfer rate and pressure drop increase [65]. Increasing *Ha* (intensifying magnetic field) leads to an increase in the Lorentz force (a retarding force to the transport phenomena), which tends to resist the fluid flow and thus reduces the nanofluid's velocity.

2.6 Flow Structures and Temperature Field

In order to better characterize the effect of vortex patterns on the wall heat transfer, vorticity and temperature contour plots are visualised using nanofluid of 2 % volume concentration, Hartmann number 20, circular cylinder placement in a rectangular duct with position and gap ratios of one each are shown in Figs. 8 to 10. Diffused and blurred structures observed in the temperature contours might be due to greater thermal diffusion than viscous diffusion. Wavy structures in the contours might be due to the cross-stream mixing by advecting vortices. Low-temperature fluid is transported towards the hot region of the duct and the high temperature fluid near the heated wall is convected away to mix with the low-temperature fluid. This transport enhances the mixing between the heated surface and the cold fluid. The effect of increasing blockage ratio from 0.2 to 0.3 at *Re* 2000 with respect to vorticity contours are compared in Fig. 8; whereas the effect with respect to temperature contours are presented in Fig. 9. The vorticity and temperature contours at *Re* 3000 and blockage ratio 0.4 are shown in Fig. 10.

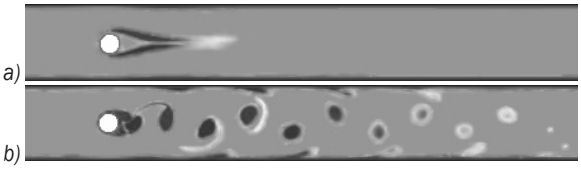

Fig. 8. *Vorticity Contour Plots for a) Re = 2000, β = 0.2 b) Re = 2000, β = 0.3*

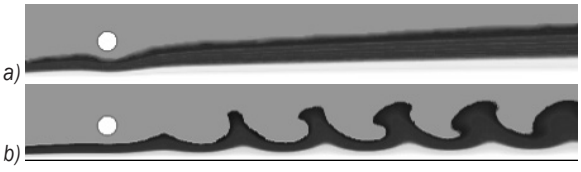

Fig. 9. *Temperature Contour Plots for a) Re = 2000, β = 0.2 b) Re = 2000, β = 0.3*

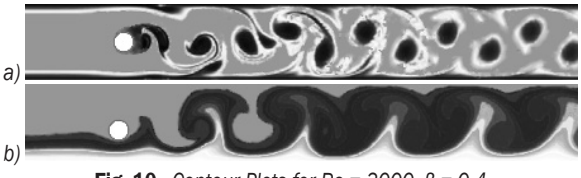

Fig. 10. *Contour Plots for Re = 3000, β = 0.4 a) vorticity b) temperature*

3 VALIDATION

The numerical system has been validated for the flow and heat transfer of stationary and oscillating cylinders in both an open flow and confined within a channel for cases with and without a magnetic field [33], [45], [66] and [67]. The mean percentage differences between the *Nu* predicted by the present simulations and those of the previous studies were less than 1 %. These studies demonstrate the reliability of the present solution. Validation was performed against published

experimental results [68] and presented in Fig. 11 to ensure the accuracy of the present formulation and model. The test concerns the critical Reynolds number (Re_c) under the influence of a magnetic field and the associated blockage ratio (β) and exhibits a very close agreement (R^2 = 0.999). The mean percentage differences between the critical Reynolds number predicted by the present simulations and those of the previous experimental study was less than 0.001 %. This study demonstrates the reliability of the present solution.

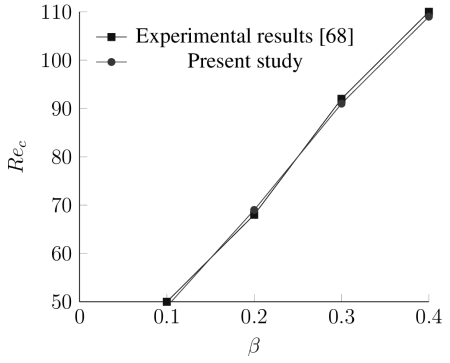

Fig. 11. *Comparison of numerical results with experimental results*

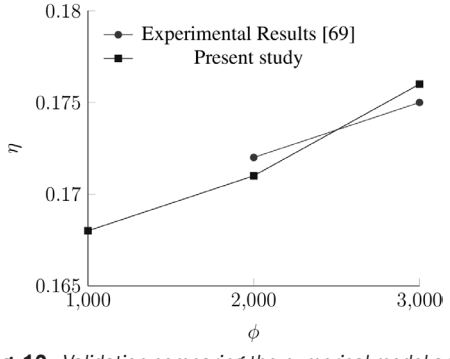

Fig. 12. *Validation comparing the numerical model and experimental results*

The Strouhal number computed for various *Re* from the numerical results of the present study is compared with those from the experimental study of a circular cylinder placed in the flow of a circulating water channel facility with Reynolds number ranging from 2000 to 5000, and velocity up to 0.4 m/s [69]. A perfect agreement of simulated and experimental values of the Strouhal number is observed (Fig. 12). The Strouhal number increase with *Re* in the present study is in agreement with that of [70]. In the Reynolds-number range ($Re \leq 1600$), the Strouhal number increased as the shear parameter increased beyond about 0.1 as reported in laboratory experiments placing circular cylinders as bluff body flow [71] and [72].

The *Nu* values of the present study at *Re* = 1000 and β = 0.2 and 0.4 were compared with the data published by [54] and found in good agreement with less than 10 % deviation, validating the model. The aforesaid model of [54] was validated with the experimental *Nu* values at *Re* = 1000 and β = 0.67 [73] and 0.5 [74] and found to be in perfect agreement by them. These studies demonstrate the reliability of the present solver.

4 CONCLUSIONS

When a circular cylinder is placed at the mid-plane of the rectangular duct with magnetic field strength and as the volume concentrations of water-based nanofluid and *Re* increase, the performance indices also increase successively. The maximum performance index augmentation was higher than two-fold at the duct centreline. As the blockage ratio increases, the performance index also increases for higher *Re* using nanofluid and magnetic field. The proximity of the cylinder to the heated wall has significant positive influence on the performance index for small blockage ratios. As the position ratio decreases, the performance index increases for all *Re* for lower blockage ratio; and as the blockage ratio increases, the performance index first increases and then decreases; thereafter, the performance index decreases successively when blockage ratio increased to 0.3 and further. When the cylinder approaches the heated wall (small gap ratio), the performance indices decrease at for all blockage ratios and *Re* than its magnitude when the cylinder is located at the duct centreline. When the cylinder is further away from both the heated wall and mid-plane, performance indices decrease for a particular blockage ratio and *Re*.

The performance indices were greater than 1 for all the cases tested, which indicates that the heat transfer enhancement for this flow is viable. Cylinder placement with gap ratios between 0.75 and 1.25 diameters performed best achieving 100 % performance index enhancement for the highest blockage ratio with the trend repeated for all blockage ratios. The highest performance indices were consistent for gap ratio one for all blockage ratios. The assumptions for quasi two-dimensional nature of the model is proved. Beyond the region from the cylinder to distance 10 diameters downstream of cylinder, where there is a successive increase in performance index is noticed; the placement of cylinder was not distinguishable. A magnetic field strength of *Ha* = 20

with blockage ratio 0.4, position ratio and gap ratio one with the circular cylinder placed 10 diameters distance downstream of cylinder at $Re = 3000$ recorded best performance index of 2.43. The Nu values of the present study were compared with the analytical and experimental data published earlier and found in perfect agreement, validating the reliability of the present model. The wake vorticity and temperature contours were found to be closely related.

5 NOMENCLATURE

a duct depth (out of plane)
B uniform magnetic field strength
f primary phase
G gap between cylinder and heated duct wall
Ha Hartmann number
L duct half-width (in the y direction)
nf nanofluid
Nu_0 Nu for duct without a cylinder
Nu_w local Nu along heated duct wall
p kinematic pressure
Ri Richardson number
s secondary phase
T_f bulk fluid temperature
T_0 cold wall and fluid temperature
T_w hot wall temperature
u quasi-two-dimensional velocity vector
u_0 Initial quasi-2 D velocity
U_0 peak fluid velocity at duct inlet
x, y streamwise direction, transverse direction
β blockage ratio
γ position ratio
δ_s Shercliff layer thickness (duct sidewalls)
η performance index
ν fluid kinematic viscosity
ρ fluid density
σ magnetic permeability of fluid
φ nanoparticle volume fraction
ΔP total pressure drop in duct
ΔP_0 duct pressure drop (no cylinder)

6 REFERENCES

[1] Dennis, S.C.R., Chang, G.Z. (1970). Numerical solutions for steady flow past a circular cylinder at Reynolds numbers up to 100. *Journal of Fluid Mechanics*, vol. 42, no. 3, p. 471-489, **DOI:10.1017/s0022112070001428**.

[2] Bharti, R.P., Chhabra, R.P., Eswaran, V. (2007). A numerical study of the steady forced convection heat transfer from an unconfined circular cylinder. *Heat and Mass Transfer*, vol. 43, no 7, p. 639-648, **DOI:10.1007/s00231-006-0155-1**.

[3] Soares, A.A., Anacleto, J., Caramelo, L., Ferreira, J.M., Chhabra, R.P. (2008). Mixed convection from a circular cylinder to power law fluids. *Industrial & Engineering Chemistry Research*, vol. 48, no.17, p. 8219-8231, **DOI:10.1021/ie801187k**.

[4] Karabelas, S.J. (2010). Large Eddy Simulation of high-Reynolds number flow past a rotating cylinder. *International Journal of Heat and Fluid Flow*, vol. 31, no. 4, p. 518-527, **DOI:10.1016/j.ijheatfluidflow.2010.02.010**.

[5] Ong, M.C., Utnes, T., Holmedal, L.E., Myrhaug, D., Pettersen, B. (2009). Numerical simulation of flow around a smooth circular cylinder at very high Reynolds numbers. *Marine Structures*, vol. 22, no. 2, p. 142-153, **DOI:10.1016/j.marstruc.2008.09.001**.

[6] Ünal, U.O., Atlar, M., Gören, O. (2010). Effect of turbulence modelling on the computation of the near-wake flow of a circular cylinder. *Ocean Engineering*, vol. 37, no. 4, p. 387-399, **DOI:10.1016/j.oceaneng.2009.12.007**.

[7] You, J.Y., Kwon, O.J. (2010). Numerical Comparisons between URANS and Hybrid RANS/LES at a High Reynolds Number Flow Using Unstructured Meshes. *International Journal of Aeronautical & Space Sciences*, vol. 11, no. 1, p. 41-48 **DOI:10.5139/IJASS.2010.11.1.041**.

[8] Belme, A., Dervieux, A., Koobus, B., Wornom, S., Salvetti, M.V. (2010). Application of hybrid and VMS-LES turbulent models to aerodynamic simulations. *27th International Congress of the Aeronautical Sciences*, p. 1-8.

[9] Mustto, A.A., Bodstien, G.C.R. (2011). subgrid-scale modeling of turbulent flow around circular cylinder by mesh-free vortex method. *Engineering Applications of Computational Fluid Mechanics*, vol. 5, no. 2, p. 259-275, **DOI:10.1080/19942060.2011.11015369**.

[10] Wornom, S., Ouvrard, H., Salvetti, M.V., Koobus, B., Dervieux, A. (2011). Variational multiscale large-eddy simulations of the flow past a circular cylinder: Reynolds number effects. *Computers & Fluids*, vol. 47, no. 1, p. 44-50, **DOI:10.1016/j.compfluid.2011.02.011**.

[11] Rajani, B.N., Kandasamy, A., Majumdar, S. (2012). On the reliability of Eddy viscosity based turbulence models in predicting turbulent flow past a circular cylinder using URANS approach. *Journal of Applied Fluid Mechanics*, vol. 5, no. 1, p. 67-79.

[12] Moussaed, C., Belme, A., Wornom, S., Koobus, B., Dervieux, A. (2014). A dynamic variational multiscale LES model for the simulation of bluff body flows on unstructured grids. *11th World Congress on Computational Mechanics*, Barcelona, p. 1-2.

[13] Valipour, M.S., Ghadi, A.Z. (2011). Numerical investigation of fluid flow and heat transfer around a solid circular cylinder utilizing nanofluid. *International Communications in Heat and Mass Transfer*, vol. 38, no. 9, p. 1296-1304, **DOI:10.1016/j.icheatmasstransfer.2011.06.007**.

[14] Grosan, T., Pop, I. (2011). Axisymmetric mixed convection boundary layer flow past a vertical cylinder in a nanofluid. *International Journal of Heat and Mass Transfer*, vol. 54, no. 15-16, p. 3139-3145, **DOI:10.1016/j.ijheatmasstransfer.2011.04.018**.

[15] Sarkar, S., Ganguly, S., Biswas, G. (2012). Mixed convective heat transfer of nanofluids past a circular cylinder in cross flow in unsteady regime. *International Journal of Heat and Mass Transfer*, vol. 55, no. 17, p. 4783-4799, **DOI:10.1016/j.ijheatmasstransfer.2012.04.046**.

[16] Sarkar, S., Ganguly, S., Dalal, A. (2012). Analysis of entropy generation during mixed convective heat transfer of nanofluids past a square cylinder in vertically upward flow. *Journal of Heat Transfer*, vol. 134, no. 12, p. 122501, **DOI:10.1115/1.4007411**.

[17] Rashidi, M.M., Bég, A.O., Freidooni, M.N., Hosseini, A., Gorla, R.S.R. (2012). Homotopy simulation of axisymmetric laminar mixed convection nanofluid boundary layer flow over a vertical cylinder. *Theoretical and Applied Mechanics*, vol. 39, no. 4, p. 365-390, **DOI:10.2298/TAM1204365R**.

[18] Dinarvand, S., Abbassi, A., Hosseini, R., Pop, I. (2015). Homotopy analysis method for mixed convective boundary layer flow of a nanofluid over a vertical circular cylinder. *Thermal Science*, vol. 19, no. 2, p. 549-561, **DOI:10.2298/TSCI120225165D**.

[19] Dinarvand, S., Hosseini, R., Damangir, E., Pop, I. (2013). Series solutions for steady three-dimensional stagnation point flow of a nanofluid past a circular cylinder with sinusoidal radius variation. *Meccanica*, vol. 48, no. 3, p. 643-652, **DOI:10.1007/s11012-012-9621-7**.

[20] Selimefendigil, F., Öztop, H.F. (2013). Identification of forced convection in pulsating flow at a backward facing step with a stationary cylinder subjected to nanofluid. *International Communications in Heat and Mass Transfer*, vol. 45, p. 111-121, **DOI:10.1016/j.icheatmasstransfer.2013.04.016**.

[21] Sarkar, S., Ganguly, S., Dalal, A. (2013). Buoyancy driven flow and heat transfer of nanofluids past a square cylinder in vertically upward flow. *International Journal of Heat and Mass Transfer*, vol. 59, p. 433-450, **DOI:10.1016/j.ijheatmasstransfer.2012.12.032**.

[22] Sarkar, S., Ganguly, S., Dalal, A., Saha, P., Chakraborty, S. (2013). Mixed convective flow stability of nanofluids past a square cylinder by dynamic mode decomposition. *International Journal of Heat and Fluid Flow*, vol. 44, p. 624-634, **DOI:10.1016/j.ijheatfluidflow.2013.09.004**.

[23] Rasekh, A., Ganji, D., Tavakoli, S. (2013). Numerical solutions for a nanofluid past over a stretching circular cylinder with non-uniform heat source. *Frontiers in Heat and Mass Transfer*, vol. 3, no. 4, p. 1-6, **DOI:10.5098/hmt.v3.4.3003**.

[24] Chamkha, A.J., Rashad, A.M., Aly, A.M. (2013). Transient natural convection flow of a nanofluid over a vertical cylinder. *Meccanica*, vol. 48, no. 1, p. 71-81, **DOI:10.1007/s11012-012-9584-8**.

[25] Sarkar, S., Ganguly, S., Dalal, A., Saha, P., Chakraborty, S. (2013). Mixed convective flow stability of nanofluids past a square cylinder by dynamic mode decomposition. *International Journal of Heat and Fluid Flow*, vol. 44, p. 624-634, **DOI:10.1016/j.ijheatfluidflow.2013.09.004**.

[26] Parezanovic, V., Monchaux, R., Cadot, O. (2015). Characterization of the turbulent bistable flow regime of a 2D bluffbody wake disturbed by a small control cylinder. *Experiments in Fluids*, p. 1-8, **DOI:10.1007/s00348-014-1890-6**.

[27] Bovand, M., Rashidi, S., Dehghan, M., Esfahani, J.A., Valipour, M.S. (2015). Control of wake and vortex shedding behind a porous circular obstacle by exerting an external magnetic field. *Journal of Magnetism and Magnetic Materials*, vol. 385, p. 198-206, **DOI:10.1016/j.jmmm.2015.03.012**.

[28] Araya, D., Dabiri, J. (2015). Transition to bluff body dynamics in the wake of vertical axis turbines. *68th Annual Meeting of the APS Division of Fluid Dynamics, Bulletin of the American Physical Society*, vol. 60, no. 21, Boston.

[29] Hossain, M.A. (1992). Viscous and Joule heating effects on MHD-free convection flow with variable plate temperature. *International Journal of Heat and Mass Transfer*, vol. 35, no. 12, p. 3485-3487, **DOI:10.1016/0017-9310(92)90234-J**.

[30] Hussam, W.K., Sheard, G.J. (2013). Heat transfer in a high Hartmann number MHD duct flow with a circular cylinder placed near the heated side-wall. *International Journal of Heat and Mass Transfer*, vol. 67, p. 944-954, **DOI:10.1016/j.ijheatmasstransfer.2013.08.081**.

[31] Burr, U., Barleon, L., Müller, U., Tsinober, A. (2000). Turbulent transport of momentum and heat in magnetohydrodynamic rectangular duct flow with strong sidewall jets. *Journal of Fluid Mechanics*, vol. 406, p. 247-279, **DOI:10.1017/S0022112099007405**.

[32] Yoon, H.S., Chun, H.H., Ha, M.Y., Lee, H.G. (2004). A numerical study on the fluid flow and heat transfer around a circular cylinder in an aligned magnetic field. *International Journal of Heat and Mass Transfer*, vol. 47, no. 19-20, p. 4075-4087, **DOI:10.1016/j.ijheatmasstransfer.2004.05.015**.

[33] Hussam, W.K., Thompson, M.C., Sheard, G.J. (2011). Dynamics and heat transfer in a quasi-two-dimensional MHD flow past a circular cylinder in a duct at high Hartmann number. *International Journal of Heat and Mass Transfer*, vol. 54, no. 5-6, p. 1091-1100, **DOI:10.1016/j.ijheatmasstransfer.2010.11.013**.

[34] Lotfi, R., Saboohi, Y., Rashidi, A.M. (2010). Numerical study of forced convective heat transfer of nanofluids: comparison of different approaches. *International Communications in Heat and Mass Transfer*, vol. 37, no. 1, p. 74-78, **DOI:10.1016/j.icheatmasstransfer.2009.07.013**.

[35] Manninen, M., Taivassalo, V., Kallio, S. (1996). On the Mixture Model for Multiphase Flow, *VTT Publications*, Espoo, p. 67.

[36] Schiller, L., Naumann, Z. (1935). A drag coefficient correlation, *Vdi Zeitung*, vol. 77, no. 318, p. 51.

[37] Karniadakis, G.E., Israeli, M., Orszag, S.A. (1991). High-order splitting methods for the incompressible Navier–Stokes equations. *Journal of Computational Physics*, vol. 97, no. 2, p. 414–443, **DOI:10.1016/0021-9991(91)90007-8**.

[38] Sommeria, J., Moreau, R. (1982). Why, how, and when, MHD turbulence becomes two dimensional. *Journal of Fluid Mechanics*, vol. 118, p. 507-518, **DOI:10.1017/S0022112082001177**.

[39] Sheard, G.J., Leweke, T., Thompson, M.C., Hourigan, K. (2007). Flow around an impulsively arrested circular cylinder. *Physics of Fluids*, vol. 19, no. 8, p. 083601, **DOI:10.1063/1.2754346**.

[40] Pothérat, A., Sommeria, J., Moreau, R. (2000). An effective two-dimensional model for MHD flows with transverse magnetic field. *Journal of Fluid Mechanics*, vol. 424, p. 75-100, **DOI:10.1017/S0022112000001944**

[41] Pothérat, A., Sommeria, J., Moreau, R. (2005). Numerical simulations of an effective two-dimensional model for flows with a transverse magnetic field. *Journal of Fluid Mechanics*, vol. 534, p. 115-143, **DOI:10.1017/S0022112005004350**.

[42] Pothérat, A. (2007). Quasi-two-dimensional perturbations in duct flows under transverse magnetic field. *Physics of Fluids*, vol. 19, no. 7, p. 074104, **DOI:10.1063/1.2747233**.

[43] Dousset, V., Pothérat, A. (2008). Numerical simulations of a cylinder wake under a strong axial magnetic field. *Physics of Fluids*, vol. 20, no. 1, p. 017104, **DOI:10.1063/1.2831153**.

[44] Karniadakis, G.E., Sherwin, S.J. (2005). *Spectral/hp Element Methods for Computational Fluid Dynamics*. Oxford University Press, New Delhi, **DOI:10.1093/acprof:oso/9780198528692.001.0001**.

[45] Sheard, G.J. (2011). Wake stability features behind a square cylinder: Focus on small incidence angles. *Journal of Fluids and Structures*, vol. 27, no. 5-6, p. 734-742, **DOI:10.1016/j.jfluidstructs.2011.02.005**.

[46] Patankar, S. (1980). *Numerical Heat Transfer and Fluid Flow*. CRC Press, New York.

[47] Esfandiary, M., Mehmandoust, B., Karimipour, A., Pakravan, H.A. (2016). Natural convection of Al2O3–water nanofluid in an inclined enclosure with the effects of slip velocity mechanisms: Brownian motion and thermophoresis phenomenon. *International Journal of Thermal Sciences*, vol. 105, p. 137-158, **DOI:10.1016/j.ijthermalsci.2016.02.006**.

[48] Buongiorno, J. (2006). Convective transport in nanofluids. *Journal of Heat Transfer*, vol. 128, no. 3, p. 240-250, **DOI:10.1115/1.2150834**.

[49] Ashorynejad, H., Sheikholeslami, M., Pop, I., Ganji, D. (2013). Nanofluid flow and heat transfer due to a stretching cylinder in the presence of magnetic field. *Heat and Mass Transfer*, vol. 49, no. 3, p. 427-436, **DOI:10.1007/s00231-012-1087-6**.

[50] Vegad, M., Satadia, S., Pradip, P., Chirag, P., Bhargav, P. (2014). Heat transfer characteristics of low Reynolds number flow of nanofluid around a heated circular cylinder. *Procedia Technology*, vol. 14, p. 348-356, **DOI:10.1016/j.protcy.2014.08.045**.

[51] Bing, R.T.H., Mohammed, H.A. (2012). Upward laminar flow around a circular cylinder using nanofluids. *Journal of Purity, Utility Reaction and Environment*, vol. 1, no. 9, p. 435-450.

[52] Etminan-Farooji, V., Ebrahimnia-Bajestan, E., Niazmand, H., Woozinesses, S. (2012). Unconfined laminar nanofluid flow and heat transfer around a square cylinder. *International Journal of Heat and Mass Transfer*, vol. 55, no. 5-6, p. 1475-1485, **DOI:10.1016/j.ijheatmasstransfer.2011.10.030**.

[53] Hussam, W.K., Thompson, M.C., Sheard, G.J. (2012). Optimal transient disturbances behind a circular cylinder in a quasi-two-dimensional magnetohydrodynamic duct flow. *Physics of Fluids*, vol. 24, p. 024105-1-024105-21, **DOI:10.1063/1.3686809**.

[54] Khan, W.A., Culham, J.R., Yovanovich, M.M. (2004). Fluid flow and heat transfer from a cylinder between parallel planes. *Journal of Thermophysics and Heat Transfer*, vol. 18, no. 3, p. 395-403, **DOI:10.2514/1.6186**.

[55] Bayat, H., Lavasani, A.M., Bolhasani, M., Moosavi, S. (2014). Numerical Investigation of Thermal-Hydraulic Performance of a Flat Tube in Cross-Flow of Air. *International Journal of Mechanical, Aerospace, Industrial, Mechatronic and Manufacturing Engineering*, vol. 8, no. 8, p. 1444-1447.

[56] Shur, M.L., Strelets, M.K., Travin, A.K., Spalart, P.R. (2015). Evaluation of Vortex generators for separation control in a transcritical cylinder flow. *American Institute of Aeronautics and Astronautics Journal*, vol. 53, no. 10, p. 2967-2977, **DOI:10.2514/1.J053851**.

[57] Ozdil, N.F.T., Akilli, H. (2015). Investigation of flow structure around a horizontal cylinder at different elevations in shallow water. *Ocean Engineering*, vol. 96, p. 56-67, **DOI:10.2514/1.J053851**.

[58] Oruc, V., Akilli, H., Sahin, B. (2016). PIV measurements on the passive control of flow past a circular cylinder. *Experimental Thermal and Fluid Science*, vol. 70, p. 283-291, **DOI:10.1016/j.expthermflusci.2015.09.019**.

[59] Kim, S., Wilson, P.A., Chen, Z.M. (2015). Large-eddy simulation of the turbulent near wake behind a circular cylinder: Reynolds number effect. *Applied Ocean Research*, vol. 49, p. 1-8, **DOI:10.1016/j.apor.2014.10.005**.

[60] Mao, X., Blackburn, H.M., Sherwin, S.J. (2015). Nonlinear optimal suppression of vortex shedding from a circular cylinder. *Journal of Fluid Mechanics*, vol. 775, p. 241-265, **DOI:10.1017/jfm.2015.304**.

[61] Venugopal, A., Agrawal, A., Prabhu, S.V. (2015). Spanwise correlations in the wake of a circular cylinder and a trapezoid placed inside a circular pipe. *Journal of Fluids and Structures*, vol. 54, p. 536-547, **DOI:10.1016/j.jfluidstructs.2014.12.008**.

[62] Kanaris, N., Albets, X., Grigoriadis, D., Kassinos, S. (2013). Three-dimensional numerical simulations of magnetohydrodynamic flow around a confined circular cylinder under low, moderate, and strong magnetic fields. *Physics of Fluids*, vol. 25, no. 7, p. 074102-1-074102-29, **DOI:10.1063/1.4811398**.

[63] Ong, M.C., Utnes, T., Holmedal, L.E., Myrhaug, D., Pettersen, B. (2010). Numerical simulation of flow around a circular cylinder close to a flat seabed at high Reynolds numbers using a k–ε model. *Coastal Engineering*, vol. 57, no. 10, p. 931-947, **DOI:10.1016/j.coastaleng.2010.05.008**.

[64] Hussam, W.K., Thompson, M.C., Sheard, G.J. (2012). Enhancing heat transfer in a high Hartmann number magnetohydrodynamic channel flow via torsional oscillation of a cylindrical obstacle. *Physics of Fluids*, vol. 24, no. 11, p. 113601-1-113601-16, **DOI:10.1063/1.4767515**.

[65] Malvandi, A., Ganji, D.D. (2014). Magnetic field effect on nanoparticles migration and heat transfer of water/alumina nanofluid in a channel. *Journal of Magnetism and Magnetic Materials*, vol. 362, p. 172-179, **DOI:10.1016/j.jmmm.2014.03.014**.

[66] Mahfouz, F.M., Badr, H.M. (2000). Forced convection from a rotationally oscillating cylinder placed in a uniform stream. *International Journal of Heat and Mass Transfer*, vol. 43, no. 11, p. 3093-3104, **DOI:10.1016/S0017-9310(99)00326-9**.

[67] Neild, A., Ng, T.W., Sheard, G.J., Powers, M., Oberti, S. (2010). Swirl mixing at microfluidic junctions due to low frequency side channel fluidic perturbations. *Sensors and Actuators B: Chemical*, vol. 150, no. 2, p. 811-818, **DOI:10.1016/j.snb.2010.08.027**.

[68] Frank, M., Barleon, L., Muller, U. (2001). Visual analysis of two-dimensional magnetohydrodynamics. *Physics of Fluids*, vol. 13, p. 2287-2295, **DOI:10.1063/1.1383785**.

[69] Meghanadhan, C.A., Sunil, A.S. (2016). An experimental study of vortex shedding behind a bluff body in a water channel.

International Journal of Engineering Research & Technology, vol. 5, no. 6, p. 701-707.

[70] Narasimhamurthy, V.D., Andersson, H.I., Pettersen, B. (2007). Direct numerical simulation of vortex shedding behind a linearly tapered circular cylinder. *IUTAM Symposium on Unsteady Separated Flows and their Control*, vol. 14, p. 201-211, **DOI:10.1007/978-1-4020-9898-7_17**.

[71] Kiya, M., Tamura, H., Arie, M. (1980). Vortex shedding from a circular cylinder in moderate-Reynolds-number shear flow. *Journal of Fluid Mechanics*, vol. 141, no. 4, p. 721–735, **DOI:10.1017/S0022112080001899**.

[72] Kwon, T.S., Sung, H.J., Hyun, J.M. (1992). Experimental investigation of uniform-shear flow past a circular cylinder. *ASME Journal of Fluids Engineering*, vol. 114, no. 3, p. 457-460, **DOI:10.1115/1.2910053**.

[73] Niggeschmidt, W. (1975). *Druckverlust und Warmeubergang bei fluchtenden, versetzten und teilversetzten querangestromten Rohrbundeln*. PhD thesis, University of Darmstadt.

[74] Hattori, N., Takahashi, T. (1993). Heat transfer from a single row of circular cylinders placed in the transverse direction of water flow. *Transactions of the Japan Society of Mechanical Engineers, Pt. B*, vol. 59, no. 568, p. 4064-4068, **DOI:10.1299/kikaib.59.4064**.

Strojniški vestnik - Journal of Mechanical Engineering 63(2017)4, 248-254
DOI:10.5545/sv-jme.2016.3898
Original Scientific Paper
Received for review: 2016-07-19
Received revised form: 2016-12-12
Accepted for publication: 2016-12-16
© 2017 Journal of Mechanical Engineering. All rights reserved.

Reliability Assessment of Bearings Based on Performance Degradation Values under Small Samples

Luosheng Qin – Xuejin Shen* – Xiaoyang Chen – Pandong Gao
Shanghai University, School of Mechatronic Engineering and Automation, China

It is difficult to obtain the lifetime data of a long lifetime bearing from a test with limited time. Therefore, to apply the method of reliability assessment based on lifetime data to the high reliability and long lifetime bearings would be impractical. The performance degradation data, which contains reliability information, could be used in the reliability assessment. However, the methods based on performance degradation data are often applied in a large sample situation. In this paper, a method suitable for a small-sample situation based on a distribution-based degradation model and a bootstrapping method combined with the Monte Carlo method (DDBMC) is proposed. This method is put forward to enlarge the sample size and estimate the distribution parameters. Then, the function between distribution parameters and time can be obtained by using the least square method. In this paper, the reliability of the ball bearings under a small sample is assessed to verify the proposed method. Finally, the proposed methodology was applied to assessing the reliability of bearings and shown to be efficient in the reliability assessment of bearings under small samples.

Keywords: bearings, distribution-based degradation, small sample, bootstrapping method, Monte Carlo method, reliability

Highlights

- *The reliability of bearings has been assessed based on the degradation data.*
- *Reliability of bearings has been revaluated by the distribution-based degradation method.*
- *Parameters of the distribution has been estimated under small samples.*
- *Parameters' degradation paths for bearings have been fitted for calculating the reliability function.*

0 INTRODUCTION

Bearings, a highly common and essential machine part, play a significant impact on machines' performance. Obviously, the lifetime of machines heavily depends on the lifetime of bearings. In recent years, the quality and reliability of the products have been increasingly emphasized. Douglas [1] pointed out the value of the reliability in electricity power. Zio [2] listed the old problems and new challenges in reliability engineering and gave some remarks on the future needs for the practice of it. Researchers have proposed various methods to assess the reliability of different products. Gao et al. [3] developed dynamic reliability models for mechanical components with a failure model of fatigue. Ognjanovic and Milutinovic [4] designed a methodology for automotive gearbox load capacity identification based on the requirement of reliability. Bicek et al. [5] inspected the most likely potential mechanical causes of failure modes for in-wheel motors. Rashid et al. [6] applied the influence diagram to establish the reliability model for a helicopter main gearbox lubrication system. The working situation of the products with high reliability, like long lifetime bearings, cannot be simply described with normal 1 and failure 0, however. It can be represented by the performance of the products during operating time. Therefore, the reliability assessment method based on performance degradation data has been developed. The performance degradation data of bearings has been applied in the reliability assessment in recent years. Support vector machine (SVM) and the Markov model were applied in the prediction of bearings' degradation process [7]. Zhang et al. [8] discussed how to choose the degradation feature of bearings to predict the remaining life of the bearings. Some other researchers [9] identified the degradation of bearings by the relevance vector machine. Many engineering and technical personnel and statistical scholars attempted to analyse products' reliability based on performance degradation data and achieved success in theoretical research and engineering application according to [10] and [11]. Pan [12] applied gamma processes in reliability assessment based on the degradation data of products.

In research studies that involve the content of reliability evaluation based on degradation data, the distribution-based degradation method is one that has been widely accepted. The distribution-based degradation method was taken into the reliability assessment, and satisfying results were obtained in literature [13] to [15]. The key step of the method is to calculate the estimation of the distribution parameters at every moment. However, the estimation method is suitable for large sample situations but is not entirely appropriate for small samples.

*Corr. Author's Address: P.O. Box 17, School of Mechatronic Engineering and Automation, Shanghai University, 149 Yanchang Road, Shanghai, China. shenxj@i.shu.edu.cn

Nowadays, the problem of small datasets is attracting increasing attention. Bootstrapping [16] is a good method to enlarge the sample sizes. Many engineers and scholars use it to raise the precision of the parameters' estimation. Structural reliability was assessed by applying the bootstrapping method, according to [17]. Li et al. [18] pointed out that the method was useful for statistics with an unknown distribution and datasets with small sample size. The Bootstrapping method and Monte Carlo simulation were applied to evaluating the uncertainty of failure rate estimation in engineering problems [19]. The Monte Carlo method is another widely used method in engineering and statistics. That method and fault tree analysis were applied to analysis of the reliability for a wastewater treatment plant [20]. The Monte Carlo simulation was also applied to the solution of the population balance equations, and the accuracy and the optimal sampling in Monte Carlo solutions of the equations have been discussed [21]. A multilevel Monte Carlo method was proposed to estimate the uncertainty in pore-scale and digital rock physics problems [22].

In this paper, a reliability assessment method, which is combined with the Monte Carlo method on the basis of distribution-based degradation method and bootstrapping method, is put forward to evaluate the reliability of bearings under small samples. To describe the method conveniently, the proposed method, i.e. reliability assessment method based on the distribution of distribution-based degradation method and bootstrapping method combined with Monte Carlo method, is called DDBMC. At the end of the paper, the proposed method was applied to assess the reliability of bearings. The DDBMC method can make full use of the performance degradation data and obtain relatively accurate results.

1 THE BASIC THEORY OF DDBMC

The distribution-based degradation method is widely used in reliability evaluation based on degradation data. The operation is simple and convenient for engineering applications, and the basic principle is described as follows.

Suppose there are n samples in the test, and a performance y during the test is recorded at every moment t_j ($j=1,2,...,m$, m is a positive integer), the matrix of performance degradation data is written as Eq. (1).

$$y=\begin{bmatrix} y_{1,1} & y_{1,2} & \cdots & y_{1,m-1} & y_{1,m} \\ y_{2,1} & y_{2,2} & \cdots & y_{2,m-1} & y_{2,m} \\ \vdots & \vdots & \cdots & \vdots & \vdots \\ y_{n-1,1} & y_{n-1,2} & \cdots & y_{n-1,m-1} & y_{n-1,m} \\ y_{n,1} & y_{n,2} & \cdots & y_{n,m-1} & y_{n,m} \end{bmatrix}. \quad (1)$$

The distribution hypothesis testing for each column of the matrix Eq. (1) should be carried out first. According to the common practice in the literature, the normal distribution function is widely selected. In this paper, the K-S hypothesis testing method is applied to verify whether the performance degradation data at every moment follow a normal distribution or not. After that, the corresponding parameters of the distribution function are estimated.

If the performance degradation data y at each time follows the normal distribution, the distribution parameters at each detection time t_j in Eq. (1) are calculated by applying Eq. (2).

$$\hat{\mu}_j=\frac{1}{n}\sum_{i=1}^{n}y_{ij},\quad \hat{\sigma}_j=\sqrt{\frac{1}{n-1}\sum_{i=1}^{n}(y_{ij}-\hat{\mu}_j)^2}, \quad (2)$$

where i represents the sample identification, $i=1,2,\ldots,n$, j represents the order of recording time, $j=1,2,\ldots,m$, $\hat{\mu}_j$ and $\hat{\sigma}_j$ refer to the parameter estimates of normal distribution.

When the parameters estimated at each moment were obtained, the optimal function between parameter and operating time could be easily evaluated by applying the least square method, and the optimal function of $\hat{\mu}_j$ and $\hat{\sigma}_j$ can be written as $\hat{\mu}(t_j)$ and $\hat{\sigma}(t_j)$. Then, the reliability estimation $\hat{R}(t_j)$ at any time t_j is:

$$\hat{R}(t_j)=\Phi\left(\frac{l-\hat{\mu}(t_j)}{\hat{\sigma}(t_j)}\right), \quad (3)$$

where l represents the products' performance degradation threshold and Φ refers to standard normal distribution function.

1.1 Estimation Method under Small Samples

The bootstrapping method combined with Monte Carlo method (BMC) is put forward to estimate parameters under small datasets. First, the Monte Carlo method is applied to simulate new data from the original data. After that, the bootstrapping method is applied to estimate the parameters.

The Monte Carlo method requires numbers that appear to be realizations of random variables.

Obtaining these numbers is the process called "generation of random numbers" [23]. A data-based random number simulation method is mentioned in [24] and the method could accurately obtain the variance of the sample. The process is expressed as follows:

a) Randomly choose a point, x_j, from the given sample.
b) Identify the m nearest neighbours of x_j (including x_j), $x_{j1}, x_{j2}, ..., x_{jm}$, and determine their mean, $\bar{x}_j$.
c) Generate a random sample, $u_1, u_2, ..., u_m$, from a uniform distribution with:
lower bound $1/m - \sqrt{3(m-1)/m^2}$ and
upper bound $1/m + \sqrt{3(m-1)/m^2}$.
d) Deliver the random variate

$$z = \sum_{k=1}^{m} u_k (x_{jk} - \bar{x}_j) + \bar{x}_j. \quad (4)$$

The simulation data at each moment t_j could be obtained by the computer according to the above steps. In this paper, m equals the original sample number, and the steps a) to d) are repeated for m times.

According to Eq. (4), estimation of parameters at every moment t_j can be referred as Eq. (5):

$$\hat{\mu}_{Mj} = \frac{1}{m}\sum_{i=1}^{m} z_i, \quad \hat{\sigma}_{Mj} = \sqrt{\frac{1}{m-1}\sum_{i=1}^{m}(z_i - \hat{\mu}_{Mj})^2}, \quad i = 1, 2, ..., m, \quad j = 1, 2, ..., n, \quad (5)$$

where m represents the simulation sample number, j represents the number of recording time, $j = 1, 2, ..., n$, $\hat{\mu}_{Mj}$ and $\hat{\sigma}_{Mj}$ refer to the normal distribution parameter estimates of simulated data.

According to the bootstrapping method, this process would be repeated for B times. In this paper, B is set as 10000, and B groups of $\hat{\mu}_{Mj(k)}$ and $\hat{\sigma}_{Mj(k)}$ ($k = 1, 2, ..., B$) are obtained at time t_j. The final estimation results of distribution parameters are calculated as shown in Eqs. (6) and (7).

$$\hat{\mu}_{BMj} = 2\hat{\mu}_{oj} - \frac{1}{B}\sum_{k=1}^{B}\hat{\mu}_{Mj(k)}, \quad (6)$$

$$\hat{\sigma}_{BMj}^{\ 2} = 2\hat{\sigma}_{oj}^{\ 2} - \left(\frac{1}{B}\sum_{k=1}^{B}\hat{\sigma}_{Mj(k)}\right)^2. \quad (7)$$

In Eq. (6), $\hat{\mu}_{oj}$ and $\hat{\sigma}_{oj}$ stand for the parameters of original samples and $k = 1, 2, ..., B$. Final estimation results of distribution parameters $\hat{\mu}_{BMj}$ and $\hat{\sigma}_{BMj}$ at every time are calculated by the method proposed. The reliability assessment method based on distribution of performance degradation values deems that distribution parameters are functions of time t, so the function expressions $\tilde{\mu}(t_j)$ and $\tilde{\sigma}(t_j)$ are easily gotten according to the estimation results $\hat{\mu}_{BMj}$ and $\hat{\sigma}_{BMj}$ of distribution parameters at every moment.

1.2 Analysis Process of DDBMC method

At every moment t_j, the test data, i.e. a column of the matrix as Eq. (1), often belongs to the same distribution function family. And parameters of the distribution can be easily estimated. In this paper, in order to solve the problem of small sample, the bootstrapping method combined with Monte Carlo method is introduced. The concrete process of this method is shown in Fig. 1.

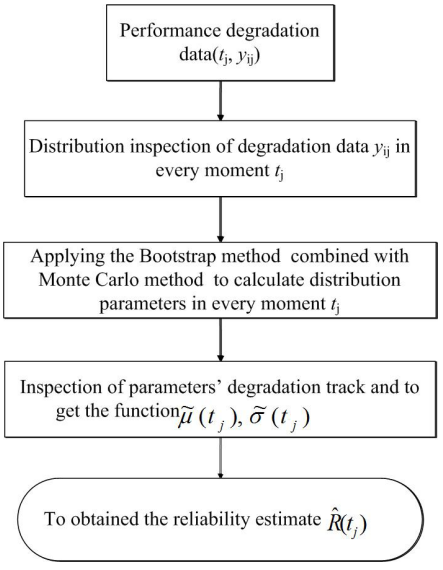

Fig. 1. *The flow chart of DDBMC method*

1.3 Validation of the Proposed Method

To verify the correctness and applicability of this method under a small sample situation, a set of bearings' degradation data is given. The data are analysed by applying the DDBMC method.

The test was carried out under the sample size $n = 7$, and the censoring time of the test was set at 4000 h. According to the requirements of the test, the axial load was set at 5 N, and the test speed was 58000 rpm. Before the formal test, the bearings were required to be run 3 hours under 1/2 test speed.

According to the requirements of the bearing manufacturer and customers, the test failure criterion was defined as: bearing radial vibration response exceeds 1.5 g, g stands for the gravity acceleration. Only when the above phenomenon was continuous, were the bearings confirmed to be failed. At the end of the test, five samples failed and only two were

survived. The operating time of the samples is listed in Table 1.

The lifetimes of the samples were assumed to follow the Weibull distribution. The traditional method, based on lifetime data and maximum likelihood estimation (MLE), was applied to the analysis of the data in Table 1. In Table 1, the status "F" stands for failure and the status "S" stands for survive. The Weibull distribution function is shown as follows.

$$F(x)=1-\exp\left(-\left(\frac{t}{\eta}\right)^{\beta}\right), \tag{8}$$

where β stands for the shape parameter, and η stands for the scale parameter. It is supposed that the operating time data is recorded as $t_{(1)}\leq t_{(2)}\leq\ldots\leq t_{(n)}$. The shape parameter and the scale parameter are calculated by the following equation [25]:

$$\begin{cases}\dfrac{1}{\beta}+\dfrac{\sum_{i=1}^{n}\lambda_i \ln t_i}{\sum_{i=1}^{n}\lambda_i}-\dfrac{\sum_{i=1}^{n}t_i^{\beta}\ln t_i}{\sum_{i=1}^{n}t_i^{\beta}}=0\\ \eta^{\beta}=\dfrac{\sum_{i=1}^{n}t_i^{\beta}}{\sum_{i=1}^{n}\lambda_i}\end{cases}. \tag{9}$$

In Eq. (9), if t_i stands for the lifetime (the status F), then $\lambda_i=1$, else $\lambda_i=0$. The MLE estimates of Weibull shape and scale parameters are 3.5699 and 3175.8909, respectively. Reliability estimation results are listed in Table 2 and shown in Fig. 2. In Table 2, "R" stands for the reliability estimation.

The bearings' vibration responses of the first 1300 h, which are recorded every 130 h, are listed in Table 3.

Hypothesis testing is put forward to verify the distribution of the data in Table 3. According to the K-S hypothesis testing method, under the condition of the significance level 0.05, the H value indicates whether to accept the hypothesis testing. $H=0$ refers to accepting it and $H=1$ refers to declining it. The results of Hypothesis testing show that the performance degradation data at every moment in Table 3 follow the normal distribution.

Table 1. *Operating times of the samples*

Sample No.	1	2	3	4	5	6	7
Status	F	F	F	F	F	S	S
Operating time [h]	1313	2288	2472	2506	3382	4000	4000

According to the vibration data in Table 3 and the DDBMC method, mean $\hat{\mu}_{BMj}$ and standard deviation $\hat{\sigma}_{BMj}$ of the samples at every moment are calculated, as shown in Table 4. An exponential model or a linear model are used to describe the degradation path of bearings, as suggested by [26] and [27]; the exponential model shows the better fit according to [28]. Next, $\hat{\mu}_{BMj}$ and $\hat{\sigma}_{BMj}$ are supposed to be fitted by the exponential function, and the functions are obtained as Eqs. (10) and (11).

Table 2. *The reliability estimation results of the first 1300 h by applying MLE*

t [h]	100	300	500	700	900	1100	1300
R	0.9999	0.9998	0.9986	0.9955	0.9890	0.9775	0.9596

Table 3. *Vibration responses of bearings [g]*

Time [h] \ Sample	1	2	3	4	5	6	7
0	0.0300	0.0870	0.0841	0.1825	0.0020	0.1163	0.0916
130	0.1850	0.4940	0.1484	0.9687	1.0516	0.4674	0.1134
260	0.2220	0.2870	0.1658	1.1680	0.9137	0.7572	0.1468
390	0.2565	0.3038	0.1585	1.1959	0.9469	0.7512	0.1195
520	0.1704	0.2750	0.1643	0.6521	1.5600	0.4170	0.1579
650	0.1900	0.8104	0.1453	1.0110	1.2832	0.6474	0.1725
780	0.2189	0.6368	0.1583	0.8428	0.9030	0.8203	0.1807
910	0.2044	0.5421	0.1885	0.5057	1.0055	0.2988	0.1894
1040	0.2244	0.6117	0.1466	0.5812	1.2964	0.5471	0.1458
1170	0.2256	0.4064	0.1825	0.3686	1.2808	0.6115	0.1338
1300	0.2305	0.3780	0.3574	0.5547	1.4624	0.7460	0.1433

$$\tilde{\mu}(t_j) = e^{0.00061t-1.2323}, \quad (10)$$

$$\tilde{\sigma}(t_j) = e^{0.00064t-.1.4095}. \quad (11)$$

Then taking Eqs. (10) and (11) into Eq. (3), and the reliability estimates are listed in Table 5 and plotted in Fig. 2.

As shown in Fig. 2, it can be found that the estimation results with the DDBMC method are close to the results estimated by MLE and tend to be conservative. This illustrates the applicability of the method under small sample and the advantages of the DDBMC method in reliability assessment based on performance degradation under small samples.

Table 4. *Sample mean and standard deviation of the vibration responses at different times [g]*

Time [h] \ Parameter	$\hat{\mu}_{BMj}$	$\hat{\sigma}_{BMj}$
0	0.0846	0.0635
130	0.4906	0.4218
260	0.5230	0.4543
390	0.5314	0.4676
520	0.4856	0.5516
650	0.6085	0.4955
780	0.5374	0.3701
910	0.4192	0.3253
1040	0.5070	0.4416
1170	0.4608	0.4336
1300	0.5540	0.4886

Table 5. *The reliability estimation results of the first 1300 h by applying DDBMC*

t [h]	700	900	1100	1300
R	0.9975	0.9907	0.9701	0.9363

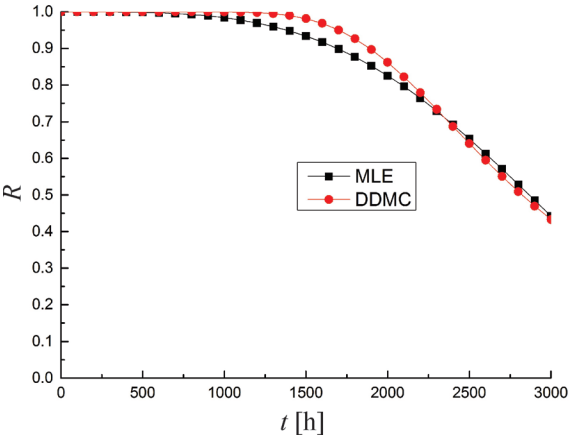

Fig. 2. *The reliability estimation comparison between MLE and DDBMC method*

2 RELIABILITY ANALYSIS OF BEARINGS

The DDBMC method is applied in assessing the reliability of bearings in this section. The test is carried out with the sample size $n=8$, and the censoring time is set at 4000 h. The test speed is 5100 rpm. According to the requirements of the bearing manufacturer and customers, the test failure criterion is defined as: bearings' vibration responses reach 6 dB higher than the initial values. The increased value of the bearings' vibration at every measurement point is recorded in Table 6.

Before processing the data in Table 6, the K-S hypothesis testing method is also applied. According to the K-S hypothesis testing method, the performance degradation data at the same moment follow the normal distribution.

According to the vibration data in Table 6 and the DDBMC method, mean $\hat{\mu}_{BMj}$ and and standard

Table 6. *The increased value of the bearings' vibration [dB]*

Time [h] \ Sample	1	2	3	4	5	6	7	8
447	1.17	0	0	0	0	0	0	0
1119	1.17	0.33	0	0	0	0	0	0
1503	0	0.33	2.58	0	0	0.37	0.53	1.99
1911	0	0	2.58	0	0	0.37	1.88	1.99
2511	0	0	2.58	0	1.1	0.37	0	0.27
2679	0	1.48	2.58	0	0	2.61	0.53	0
3015	1.17	0.33	1.12	0	0	0.37	1.88	1.99
3279	0	1.48	1.12	0	0	0.37	0	1.99
3687	1.17	0.34	1.12	0	2.3	0.37	0	1.99
3911	0	1.48	0	0	2.3	3.69	0	1.99
3983	0	0.34	0	0	1.1	3.69	0	0.27

deviation $\hat{\sigma}_{BMj}$ of the samples at every moment are listed in Table 7. The function expressions as Eqs. (12) and (13) are obtained from the results in Table 7.

$$\tilde{\mu}(t_j) = e^{0.00043t-1.6213}, \quad (12)$$

$$\tilde{\sigma}(t_j) = e^{0.00025t-0.6985}. \quad (13)$$

Next, by taking Eqs. (12) and (13) into Eq. (3), reliability estimates can be plotted in Fig. 3. Reliability estimates in the 5000 h are listed in Table 8.

As shown in Fig. 3, the rating life of the bearings is about 6720 h, which means the reliability of the bearings is 0.9 at about 6720 h under the test condition. It could also be found in Fig. 3 that the lifetime data is difficult to obtain in this situation while the proposed DDBMC method demonstrates effectiveness to solve the problem.

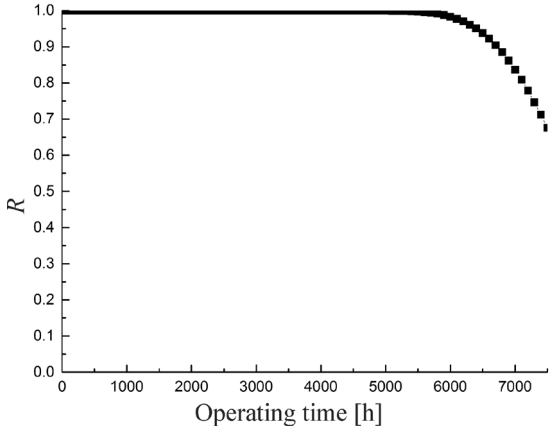

Fig. 3. *Reliability estimation of the bearings*

Table 7. *Sample mean and standard deviation of the vibration responses at different time [dB]*

Time [h] \ Parameter	$\hat{\mu}_{BMj}$	$\hat{\sigma}_{BMj}$
447	0.1455	0.4508
1119	0.1886	0.4508
1503	0.7273	1.0878
1911	0.8565	1.2025
2511	0.5410	0.9886
2679	0.9023	1.2713
3015	0.8623	0.8749
3279	0.6242	0.8735
3687	0.9087	0.9695
3911	1.1754	1.5375
3983	0.6737	1.3900

Table 8. *Reliability estimation results of the bearings*

t [h]	3500	4000	4500	5000
R	0.9999	0.9999	0.9988	0.9934

3 CONCLUSIONS

It is impractical to analyse the reliability of bearings based on lifetime data because of the difficulty of obtaining highly reliable bearing data. Reliability analysis based on performance degradation data solves the problem of reliability assessment without lifetime data, although, the existing performance degradation method cannot obtain the ideal results under small samples. In this paper, a method called DDBMC is proposed to solve this problem, and it is suitable for assessing the reliability of products with high reliability under small data sets.

In addition, the method of generating simulated data used in this article completely depends on the test sample data, which can simultaneously retain the original nature of the sample data and expand the original data. Finally, the results under small sample are close to the real situation.

To summarize, the DDBMC method can evaluate the reliability under small samples without lifetime data. However, it should be pointed out that the DDBMC method considers only the small sample problem and ignores the problem of little measurement point, which still needs further study.

4 ACKNOWLEDGEMENT

This work is carried out with financial support from the National twelfth five-year projects of China for science and technology under Contract D.50-0109-15-001 and D.71-0109-16-046.

5 REFERENCES

[1] Douglas, J. (1986). The value of reliability. *IEEE Power Engineering Review*. vol. 9, p. 5-9, **DOI:10.1109/MPER.1986.5527635**.

[2] Zio, E. (2009). Reliability engineering: old problems and new challenges. *Reliability Engineering & System Safety*, vol. 94, no. 2, p. 125-141, **DOI:10.1016/j.ress.2008.06.002**.

[3] Gao, P., Yan, S.Z., Xie, L.Y., Wu, J.N. (2013). Dynamic reliability analysis of mechanical components based on equivalent strength degradation paths. *Strojniški vestnik - Journal of Mechanical Engineering*, vol. 59, no. 6, p. 387-399, **DOI:10.5545/sv-jme.2012.541**.

[4] Ognjanovic, M., Milutinovic, M. (2013). Design for reliability based methodology for automotive gearbox load capacity identification. *Strojniški vestnik - Journal of Mechanical Engineering*, vol. 59, no. 5, p. 311-322, **DOI:10.5545/sv-jme.2012.769**.

[5] Biček, M., Gotovac, G., Miljavec, D., Zupan, S. (2015). Mechanical failure mode causes of in-wheel motors. *Strojniški vestnik - Journal of Mechanical Engineering*, vol. 61, no. 1, p. 74-85, **DOI:10.5545/sv-jme.2014.2022**.

[6] Rashid, H.S.J., Place, C.S., Mba, D., Keong, R.L.C., Healey, A., Kleine-Beek, W., Romano, M. (2015). Reliability model for helicopter main gearbox lubrication system using influence diagrams. *Reliability Engineering & System Safety*, vol. 139, p. 50-57, **DOI:10.1016/j.ress.2015.01.021**.

[7] Dong, S.J., Yin, S.R., Tang, B.P., Chen, L.L., Luo, T.H. (2014). Bearing degradation process prediction based on the support vector machine and Markov model. *Shock and Vibration*, vol. 2014, p. 1-14, **DOI:10.1155/2014/717465**.

[8] Zhang, B., Zhang, L.J., Xu, J.W. (2016). Degradation feature selection for remaining useful life prediction of rolling elements bearings. *Quality and Reliability Engineering International*, vol. 32, no. 2, p. 547-554, **DOI:10.1002/qre.1771**.

[9] Caesarendra, W., Widodo, A., Thom, P.H., Yang, B.S., Setiawan, J.D. (2011). Combined probility approach and indirect data-driven method for bearing degradation prognostics. *IEEE Transactions on Reliability*, vol. 60, no. 1, p. 14-20, **DOI:10.1109/TR.2011.2104716**.

[10] Lu, J.C., Meeker, W.Q. (1993). Using degradation measures to estimate a time-to-failure distribution. *Technometrics*, vol. 35, no. 2, p. 161-174, **DOI:10.2307/1269661**.

[11] Crk, V. (2000). Reliability assessment from degradation data. *Annual Proceedings of Reliability and Maintainability Symposium*, p. 155-161, **DOI:10.1109/RAMS.2000.816300**.

[12] Pan, Z., Balakrishnan, N. (2011). Reliability modeling of degradation of products with multiple performance characteristics based on gamma processes. *Reliability Engineering & System Safety*, vol. 96, no. 8, p. 949-957, **DOI:10.1016/j.ress.2011.03.014**.

[13] Li, C.Q. (1995). Computation of the failure probability of deteriorating structural systems. *Computers & Structures*, vol. 56, no. 6, p. 1073-1079, **DOI:10.1016/0045-7949(94)00947-2**.

[14] Yang, K., Xue, J.N. (1996). Continuous state reliability analysis. *Proceedings Annual of the Reliability and Maintainability Symposium*, p. 251–257.

[15] Chen, Y.X., Zeng, Z.G., Kang, R. (2012). Validation methodology for distribution-based degradation model. *Journal of System Engineering and Electronics*, vol. 23, no. 4, p. 553-559, **DOI:10.1109/JSEE.2012.00069**.

[16] Efron, B. (1979). Bootstrap methods: Another look at the Jackknife. *The Annals of Statistics*, vol. 7, no. 1, p. 1-26, **DOI:10.1214/aos/1176344552**.

[17] Chaves, I.A., Machado, P.D., Neto, A.C. (2014). Estimation of failure probability in corroded oil pipelines through Monte Carlo simulation method applying the Bootstrap technique. *International Journal of Applied Science and Technology*, vol. 4, no. 5, p. 141-152.

[18] Li, D.Q., Tang, X.S., Zhou, C.B., Phoon, K.K. (2015). Characterization of uncertainty in probabilistic model using bootstrap method and its application to reliability of piles. *Applied Mathematical Modeling*, vol. 39, no. 17, p. 5310-5326, **DOI:10.1016/j.apm.2015.03.027**.

[19] Kumar, B., Datta, D. (2010). Estimation of probability of failure using bootstrap methods. *International Conference on Reliability, Safety and Hazard*, p. 143-146, **DOI:10.1109/ICRESH.2010.5779532**.

[20] Taheriyoun, M., Moradinejad, S. (2015). Reliability analysis of a wastewater treatment plant using fault tee analysis and Monte Carlo simulation. *Environmental Monitoring and Assessment*, vol. 187, p. 1-13, **DOI:10.1007/s10661-014-4186-7**.

[21] Yu, X., Hounslow, M.J., Reynolds, G.K. (2015). Accuracy and optimal sampling in Monte Carlo solution of population balance equation. *AIChE Journal*, vol. 61, no. 8, p. 2394-2402, **DOI:10.1002/aic.14837**.

[22] Icardi, M., Boccardo, G., Tempone, R. (2016). On the predictivity of pore-scale simulations: Estimating uncertainties with multilevel Monte Carlo. *Advances in Water Resources*, vol. 95, p. 46-60, **DOI:10.1016/j.advwatres.2016.01.004**.

[23] Gentle, J.E. (2009). *Computational Statistics.* Springer, Dordrecht, **DOI:10.1007/978-0-387-98144-4**.

[24] Taylor, M.S., Thompson, J.R. (1986). A data based algorithm for the generation of random vectors. *Computational Statistics & Data Analysis*, vol. 4, no. 2, p. 93-101, **DOI:10.1016/0167-9473(86)90013-7**.

[25] Kahle, W. (1996). Estimation of the parameters of the Weibull distribution for censored samples. *Metrika*, vol. 44, no. 1, p. 27-40, **DOI:10.1007/BF02614052**.

[26] Shao, Y., Nezu, K. (2000) Prognosis of remaining bearing life using neural networks. *Proceedings of the Institution of Mechanical Engineers, Part I: Journal of Systems and Control Engineering*, vol. 214, no. 3, p. 217-230, **DOI:10.1243/0959651001540582**.

[27] Gebraeel, N., Lawley, M., Liu, R., Parmeshwaran, V. (2004) Residual life predictions from vibration-based degradation signals: A neural network approach. *IEEE Transactions on Industrial Electronics*, vol. 51, no. 3, p. 694-700, **DOI:10.1109/TIE.2004.824875**.

[28] Sotrisno, E., Oh, H., Vasan, A.S.S., Pecht, M. (2012). Estimation of remaining useful life of ball bearings using data driven methodologies. *IEEE Conference on Prognostics and Health Management*, **DOI:10.1109/ICPHM.2012.6299548**.

Strojniški vestnik - Journal of Mechanical Engineering 63(2017)4, 255-264
© 2017 Journal of Mechanical Engineering. All rights reserved.
DOI:10.5545/sv-jme.2016.3721 Original Scientific Paper
Received for review: 2016-05-08
Received revised form: 2016-08-06
Accepted for publication: 2016-12-07

An Experimental Investigation and Numerical Simulation in SPF of AA 5083 Alloy using Programming Logic Control Approach

Muthusamy Balasubramanian[1,*] – Pasupathy Ganesh[2] – Kalimuthu Ramanathan[3] – Velukkudi Santhanam Senthil Kumar[4]

[1]Anna University, University College of Engineering, India
[2]Anna University, Madras Institute of Technology, India
[3]Alagappa Chettiar College of Engineering and Technology, India
[4]Anna University, College of Engineering Guindy, India

A new programming logic control method is proposed to predict the pressure during the superplastic forming process with improved forming characteristics of AA 5083 alloy sheets. The method has produced a better uniformity thickness profile in a complex, multidimensional profile in comparison with existing methods. To optimize pressure during the forming process, it is possible to maintain an optimum strain rate. Accurate control of the magnitude and duration of forming pressure and, as a result, the achievement of uniform thickness distribution in the taper angle, die corner, entry regions, and micro-forming of the multidimensional dome has been proved in this paper. Profiles formed without significant wrinkles and necking have been obtained via the fine adjustment of the applied pressure. The experimentally obtained results, using a multidimensional dome profile, are compared with the finite element method (FEM) simulated results and both are found to be in good agreement. The influence of key factors such as strain rate sensitivity index and friction coefficient on the optimum pressure-time cycle and also on the thickness distribution of the profile have been investigated and optimized. Furthermore, the microstructure was examined in parent metal and superplastically formed components.

Keywords: superplastic forming, finite element method, programming logic control circuit, aluminium 5083 alloy, multidimensional dome

Highlights

- *A multistage multidimensional profile has been performed with a single blow forming operation.*
- *Optimum pressure time cycle was predicted to obtain uniform thickness distribution by using a newly proposed programming logic control method.*
- *Finite element modelling results were found to be fairly in agreement with the experimental results.*
- *Minimum forming time, forming pressure and uniform thickness profile obtained as a function of friction coefficient and strain rate sensitivity index.*
- *Obtained uniform thickness profile with a function of die entry radius, taper angle, die corner, and micro-forming regions.*

0 INTRODUCTION

Superplastic forming is an important technique that can be found in the aerospace industry, automobile exterior components and turbine blades, where various dimensions have to be created in a single blow-forming operation. In such situations, prior knowledge of multidimensional profile forming operations will be highly relevant and useful. Factors including uniform thickness distribution, prevention of excessive thinning and wrinkles in the final product assume paramount importance in any multidimensional superplastic forming process. For achieving uniform thickness distribution in a multidimensional profile, controlling pressure during the blow forming process is essential. In order to control the forming pressure, the strain rate needs to be maintained at an optimum value. Previously, different numerical methods were used for the prediction of optimal pressure cycle in a long rectangular box [1], circular cup [2], hemispherical dome [3], and cone cup of simple shape components [4]; these consumed more time for computation and experimentation; furthermore, material elongation with a genetic approach [5] consumes more time for computation and mutation. To make both theoretical prediction and experimentation faster, sophisticated modeling and simulation approaches have been used recently for studying superplastic forming behaviour.

Dutta and Mukherjee [6] have developed a simple pressure-time equation for superplastic forming under biaxial stress conditions to predict the required gas pressure to optimize the flow stress, strain rate and geometric properties of the sheet thus formed. Using the ABAQUS code, Jarraret et al. [7] have analysed high-temperature bulge forming of 5083 Al alloy by keeping the pressure constant but at different

*Corr. Author's Address: Department of Mechanical Engineering, University College of Engineering-Ramanathapuram, Tamil Nadu, India, annaunivbala76@gmail.com

levels and reported the ability of the model to predict deformation behaviour. Balasubramanian et al. [8] have optimized the uniform thickness distribution in different die radii domes (the parametric design models) and different die entry regions in a three-stage hemispherical dome with constant pressure method. Carrino et al. [9] have proposed a time incremental-loading process to maintain maximum strain rate during the pressure cycle. They have reported a decrease in forming time, better material flow, and uniform thickness distribution in a circular cup. Snippe and Meinders [10] have suggested the back-pressure method for obtaining maximum dome height in a spherical vessel and proposed improvements in leak tightness. Dezelak et al. [11] have analysed the effect of the twist spring back method for a metal sheet by using elastic-plastic shell elements in a finite element method (FEM) simulation. Hambli et al. [12] have used a constrain algorithm to predict the pressure cycle in 2D and 3D finite element analysis (FEA) models and found no significant difference between the results obtained from 2D and 3D FEA simulations of a simple conical cup.

Nituet et al. [13] have reported that a finite element simulation process was used to predict the forming characteristics with minimum forming time with high precision. Luckey et al. [14] have developed a pressure prediction algorithm under the average scheme method to maintain a target strain rate and reported that the scheme improves the thickness profile in single-stage rectangular components. Aoura et al. [15] have proposed the constant stress control method to predict the pressure cycle for superplastic forming processes. They have suggested this method to be a better one to maintain the optimum strain rate and to obtain a uniform distribution of thickness in axi-symmetric components. Jarrar et al. [16] have developed a constrained pressure prediction algorithm to predict optimum pressure, maintaining the maximum strain rate, and to obtain better thinning at different die entry regions of a mid-section of a rectangular pan. Based on a logarithmic pressure control algorithm to predict the pressure cycle and to maintain the maximum strain rate, Hojjati et al. [17] reported that forming time decreases with better thickness distribution in a conical cup when compared to the results obtained using the constant pressure control and constraint control algorithm methods. In these studies, the authors have focused on thickness distribution and minimum forming time, using components with simple shapes.

In this work, a programming logic control (PLC) system has been developed that can control the forming pressure accurately to maintain the strain rate as constant and closer to the optimum value throughout the blow forming process. Furthermore, the coding system also incorporates features that can improve the uniformity of the thickness profile in the taper angle, die entry, die corner and micro-forming regions of multidimensional components. The proposed PLC approach can be designed to change the amplitude of displacement and the time increment even while the forming process is underway, with the provision of interchanging the mode independently. This approach can also be more flexible in allowing sufficient time required for slow filling in corner regions, thereby eliminating the defects caused by otherwise fast filling. Using this coding system in this work, the effect of forming pressure, forming time, and uniformity of thickness with respect to the coefficient of friction, strain rate sensitivity index, and forming temperature have been investigated using a multidimensional dome.

1 EXPERIMENTAL PROCEDURE

Experimental validation of the proposed PLC approach for predicting the pressure cycle in superplastic forming (SPF) of an aluminium alloy, AA5083, is presented in this section. From the uniaxial hot tensile tests [8], the optimum forming temperature of AA 5083 was found to be 450 °C at a strain rate of 1.21×10^{-3} s^{-1} with the strain rate sensitivity index m of 0.39 and material constant, k, of 159.5 MPa s^{-m}. The chemical composition and mechanical properties of AA 5083 are given in Tables 1 and 2.

Table 1. *Chemical composition of AA 5083 alloy (% weight)*

Si	Fe	Cu	Mn	Mg	Cr	Zn	Ti	Al
0.128	0.185	0.001	0.171	2.96	0.052	0.051	0.023	Balance

Table 2. *Mechanical properties of AA 5083 alloy*

Tensile yield strength [MPa]	250
Ultimate tensile strength [MPa]	320
Shear strength [MPa]	185
Modulus of elasticity [GPa]	75
Shear modulus [GPa]	26.4
Poisson's ratio	0.3
Density [kg/m^3]	2650
Melting point [°C]	590 – 610
Thermal conductivity [W m^{-1} K^{-1}]	121

The SPF of the PLC process is shown in Fig. 1a and b. The air pressure flows into the switched adaptive control system and then is delivered to the

die cavity with constant or varying pressure. The system can automatically adjust and switch operating parameters according to changes of increment depending upon the forming height and temperature is maintained in the die cavity. Shown in Fig. 1a, the system mainly consists of a PLC control body and switched adaptive control body. The PLC control body includes the central processing unit (CPU) and pressure sensor.

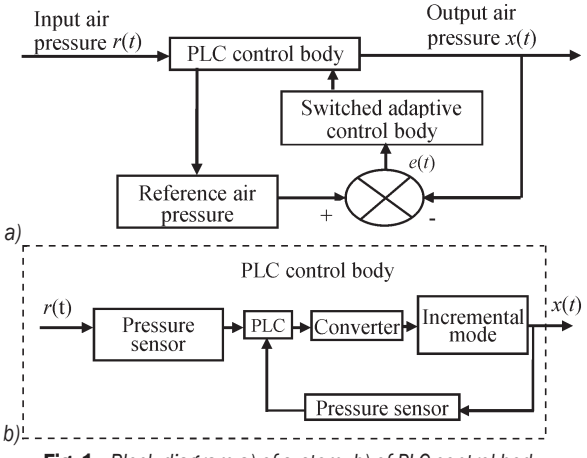

Fig. 1. *Block diagram a) of system; b) of PLC control body*

The PLC is the core controller of the system. It sets reference air pressure through its internal programs. The reference pressure is compared with real-time ones monitored by pressure transmitter to obtain the deviation. Then, based on the deviation and switched adaptive control algorithm, the PLC gives appropriate instructions to the converter. The pressure transmitter embedded analogue/digital (a/d) inverter can communicate directly with PLC via recommended standard. All the components constitute a stable closed-loop control system. The PLC control body block diagram as shown in Fig.1b,where the pressure incrementation is performed with programmed pressure profile.

The experimental setup for the SPF process with the PLC processing circuit is shown in Fig. 2. The setup consists of three major parts: the PLC processing circuit, the forming die, and the pressure regulator. In this experimental setup, the PLC circuit consists of a program interface circuit (PIC) with a microcontroller. It has simultaneous access to the program and data memory technology and integrates a number of the components of a microprocessor system on to a single chip (PIC 16F877). It is built into the CPU, memory, peripherals and other devices, such as timer module, to allow the microcontroller to perform tasks for certain time periods, a serial I/O port to allow data to flow between the controller and program interface circuit and an analogue/digital inverter to allow the microcontroller to accept analogue input data for processing.

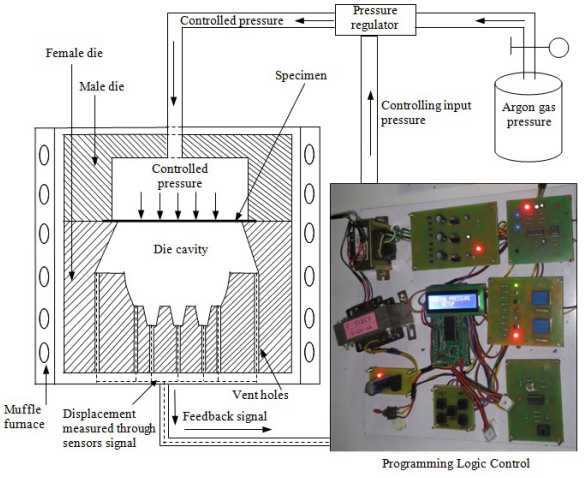

Fig. 2. *Experimental setup for PLC control in SPF process*

The PLC programme starts to function once the optimum temperature of 450 °C is reached. The set temperature (optimum experimental temperature) values are received from the temperature control unit, i.e. the PLC programme, starts to open the pressure control valve very slowly and controlling pressure passes on the surface of the blank. Next, the blank starts to be blow formed, the PLC circuit sensors measure the displacement of blank and send feedback to PLC programme. The PLC sensors measure every small positive incremental displacement value at different places of the die surface. The input pressure values are varying with respect to the movement of the blank into the die cavity.

The PLC coding was developed based on the die profile, that is, to release the high quantity of pressure when the blank moves through free regions and reduces the pressure values when the blank move towards die corner and micro forming regions in order to obtain smooth forming profiles. The pressure values are determined by the researcher, based on the die dimensions and fed into the input values through the PLC input key before starting the programme. The input values slowly vary during progress on because of slowly filling of blank in the die corner and micro forming regions thereby eliminating the defects because fast filling may lead to incomplete forming. Similarly, the PLC code was developed based on forming time mode condition.

The experimental process was started with controlling of pressure during forming with two

different mode conditions. In the first mode condition, pressure was regulated for every incremental displacement (x) of 0.1 mm during forming of the sheet in the die cavity. Each increment step, the movement was sensed by a sensor and fed back to the program to take appropriate decision. The x value of 0.1 mm displacement further was reduced to 0.05 mm, if the blank move towards the corner and micro forming regions. The process ran until the blank reached all regions. The displacement values of 0.1 mm and 0.05 mm are variable input parameters will modified to appropriate numerical value (with lower value of decimal point) before starting the program.

In the second mode condition, pressure will be regulated for every incremental time of t minute for movement of the blank during the forming of the sheet in to the die cavity. Each time (t) increment steps, the displacement of blank will be sensed by the sensor and feedback will be sent to the program. Further time interval reduced if the blank move towards a corner and micro-forming regions. The time incremental values are variable input parameters and change to any numerical value before starting the program; the appropriate numerical value will be changed when changing the shape of forming. This paper deals with displacement mode condition only.

The die setup consists of male and female dies. The female split die has different dimensions at different stages. The first stage dimensions were kept at a 110° inside taper angle with a top radius of 30 mm and a depth of 9 mm. In the second stage, the radius and depth were kept at 30 mm and 11 mm, respectively. Similarly, for the third stage, tapered grooves with a top radius of 3 mm, bottom radius of 1.5 mm and a depth of 2.5 mm were maintained. Finally, the radius at the centre was maintained at 2.5 mm. The die entry radii at the first (R_1), second (R_2) and third stages (R_3) were kept at 3 mm, 2 mm and 1.5 mm, respectively, as shown in Fig. 3.

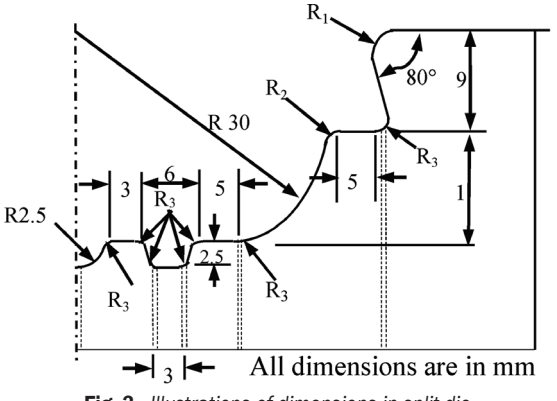

Fig. 3. *Illustrations of dimensions in split die*

A 72-mm diameter slot was provided in the female die with a depth of 1 mm. The entire die setup, consisting of both the male and female parts, was surrounded without any air gap by a band heater and the entire assembly was placed in a 100 kN hydraulic press under airtight conditions. The die setup was heated up to the optimum temperature [8] of 450 °C and maintained until the experiment was completed. The 72-mm diameter and 1.5 mm thick specimens were kept between the male and female parts.

a) *b)* *c)*

Fig. 4. *Experimentally formed components at different pressure control method of: a) constraint algorithm, b) logarithmic algorithm, and c) PLC*

Next, the variable argon gas pressure was applied by three different pressure control method such as logarithmic algorithm [17], constraint algorithm [18] and the newly proposed PLC method. The thickness distribution, forming time and pressure cycle are evaluated for forming components with a function of three different pressure control methods. The final formed components for different pressure control methods are shown in Fig. 4.

2 FINITE ELEMENT ANALYSIS

The blank and die configurations employed for FEM in ABAQUS 6.8 of the AA5083 alloy sheet with a multidimensional die profile are shown in Fig. 5. The circular blank with an initial thickness of 1.5 mm and a diameter of 72 mm was clamped tightly between the male and female dies using a 6-mm outer rim. Throughout the simulation, the sheet was fixed at the outside edge in order to avoid any possible slipping into the dies. A 3D finite element quarter model was created with the ABAQUS pre-processor and used to study the blow forming process in superplastic forming simulation. The geometry of the blank material was assumed to undergo visco-plastic [8] deformation and the die was assumed to be a discrete rigid body. The blank was meshed with the shell element [14] with 2752 nodes and the rigid die was meshed with R3D3 element with 3018 nodes. In numerical simulation process, the following material data are used. The modulus of elasticity is 75 GPa, Poisson's ratio of 0.3,

material constant is 159.5 MPa s^{-m}, optimum strain rate of 1.21×10^{-3} s^{-1}, strain rate sensitivity index of 0.39 and optimum temperature of 450 °C.

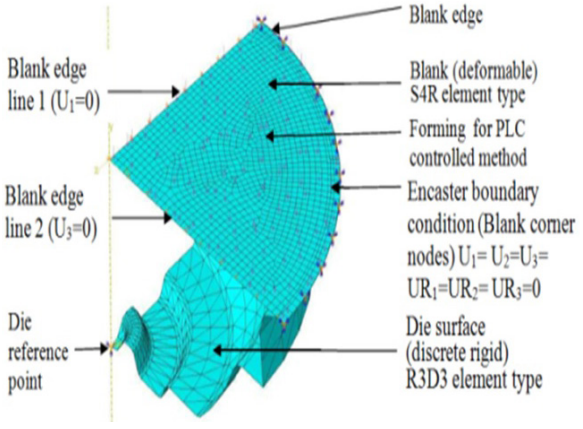

Fig. 5. *AA5083 alloy sheet with a multi-dimensional die profile*

The gas pressure was imposed on the top surface of the blank was kept at 450 °C. This caused the flow of the sheet into the bottom die cavity gradually. The PLC in FEM simulation was deployed to monitor and control the applied pressure with respect to forming time and displacement in order to maintain the optimum strain rate. Finite element simulations at different stages are shown in Fig. 6. Furthermore, the FEM simulation process was carried out with three different pressure control algorithm approaches.

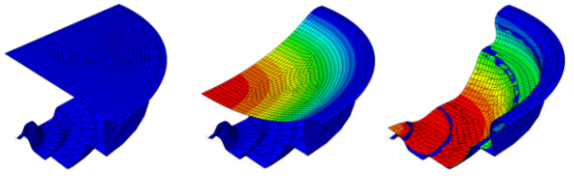

Fig. 6. *Finite element simulation process at different stages in PLC method*

3 RESULTS AND DISCUSSIONS

3.1 Prediction of Best Pressure Control Method with a Function of Forming Time and Pressure Cycle

The pressure applied during forming was controlled with accuracy and monitored by a PLC system in all the experiments. The same code has also been generated using the FEM model to predict the forming pressure at target strain rate conditions. The FEM results are compared with experimental values in terms of the pressure-time cycle relationship with target strain rate conditions as shown in Fig. 7. The results show that the FEM results are in good agreement with the experimental values at a maximum error of 2.1 %.

Fig. 7 shows the comparison of forming pressure as a function of forming time obtained using the PLC method along with the other two pressure control methods via experiment and FEM at a temperature of 450 °C. The newly developed PLC method and the experimental and FEM simulation results are in close agreement. Comparison of the latter has become imperative with the pressure prediction algorithms such as logarithmic algorithm [17] and constraint algorithm [18]. In a constraint algorithm method, the pressure was controlled by time incremental step from a minimum limit of 0.2 to a maximum level of 3 with different load magnitude, beyond this value the programme was abandoned and restarted according to the following load modifications:

$$\begin{aligned} &\text{If} \quad q_{\min} < 0.2 \quad \text{then} \quad p_{\text{new}} = 2\, p_{\text{old}} \\ &\text{If} \quad q_{\max} > 3 \quad \text{then} \quad p_{\text{new}} = 0.5\, p_{\text{old}}\ , \end{aligned}$$

where q is the ratio of maximum strain rate to target strain rate, p_{new} is the new pressure magnitude and p_{old} is the old pressure magnitude from the previous steps. If $0.2 < q > 3$, the increment is accepted, and the pressure is adjusted as follows.

$$\begin{aligned} &\text{If} \quad 0.2 < q < 0.5 \quad \text{then} \quad p_{\text{new}} = 1.5\, p_{\text{old}} \\ &\text{If} \quad 0.5 < q < 0.8 \quad \text{then} \quad p_{\text{new}} = 1.2\, p_{\text{old}} \\ &\text{If} \quad 0.8 \le q < 1.5 \quad \text{then} \quad p_{\text{new}} = 1\, p_{\text{old}} \\ &\text{If} \quad 1.5 \le q < 3 \quad \text{then} \quad p_{\text{new}} = 0.834\, p_{\text{old}}\ . \end{aligned}$$

The obtained pressure profile at each time increment is applied on the free region of the sheet during forming.

In a logarithmic algorithm method, the time incremental step has been modified in order to obtain the optimum strain rate. The pressure value is obtained for the next time increment by using the following correlation Eq. (1):

$$P_{n+1} = \left[1 - \ln\left(\frac{\dot{\varepsilon}_{\max}}{\dot{\varepsilon}_{\text{opt}}}\right)\right] P, \tag{1}$$

where $P(t)$ is the forming pressure needed at a time of t until $\dot{\varepsilon}_{\max}/\dot{\varepsilon}_{\text{opt}} > 2.72$ This predicts a negative pressure value if the value increases more than 2.72. In order to prevent this negative pressure, two provisions have been made. First, by choosing small time increment, a rapid change is prevented. Secondly, the applied pressure is reduced by a factor of 0.5 and the analysis is repeated in this manner until this negative pressure is resolved. However, in the PLC method, the pressure was controlled with a function of displacement of the blank in to the die cavity.

Hojjati et al. [17] have analysed the optimum pressure profile and thickness distribution using three different pressure levels (0.6 MPa, 0.8 MPa and 1 MPa) as well as constraint and logarithmic algorithms. They report that the logarithmic algorithm method gives better results for achieving uniform thickness distribution with minimum forming time. On comparing the results based on the existing algorithms with the results obtained using PLC, it can be clearly seen that the PLC process gives better results in a multi-dimensional profile, as evident in Fig. 7 and Table 2. Fig. 7 shows that the applied pressure gradually keeps increasing until the blank reaches the die surface beyond which it gradually decreases to achieve uniform thickness distribution in a multi-dome shape in all the three control processes.

Table 2. *Forming time obtained with different pressure control processes*

Pressure forming method	Time [min]		% of error	Forming pressure [MPa] at maximum level		% of error
	Exp	FEA		Exp	FEA	
Constraint algorithm	62	63.56	2.52	0.43	0.445	3.5
Logarithmic algorithm	57	58.14	2.0	0.45	0.462	2.7
PLC approach	51	52.12	2.2	0.39	0.398	2.1

In the constraint algorithm method, the applied pressure has a step-by-step magnitude increment process reflecting higher oscillations in the stress and therefore results in a variation in pressure profile in the die entry and corner regions with high pressure of 0.43 MPa and a forming duration of 62 minutes. The logarithmic algorithm method requires a higher pressure of 0.45 MPa with forming duration of 57 minutes to complete the profile with more oscillations in the stress. It reflects the variation in pressure profile in corner regions.

In the PLC approach, 0.39 MPa of maximum pressure level is needed to fill the die cavity within 51 minutes and the smooth pressure profile has been achieved, as evident in Fig. 7. In the PLC method, the forming time decreases because of greatly reduced oscillations and stress during forming at corners regions. Fig. 7 and Table 2, shows that the optimum (minimum) forming pressure 0.39 MPa, forming time of 51 minutes, and smooth pressure cycle have been obtained in the PLC method, compared to other pressure control methods. This is because the entire PLC pressure cycle method has been developed based on the forming height with respect to strain rate and a temperature. Furthermore, the PLC-based pressure cycle mechatronics approach will be designed and constructed to change the amplitude (very small) of displacement step during forming. This approach can also be more flexible and highly precise to regulate the flow of pressure for slow filling in corner regions, thereby eliminating oscillations and premature fracture.

3.2 Prediction of Best Pressure Control Method with a Function of Thinning Factor for Optimizing Thickness Distribution

The superplastic forming processes were carried out experimentally and numerically using constraint algorithm, logarithmic algorithm and PLC approach in a multistage multidimensional split die model, the and results of thickness distribution are shown in Fig. 8.

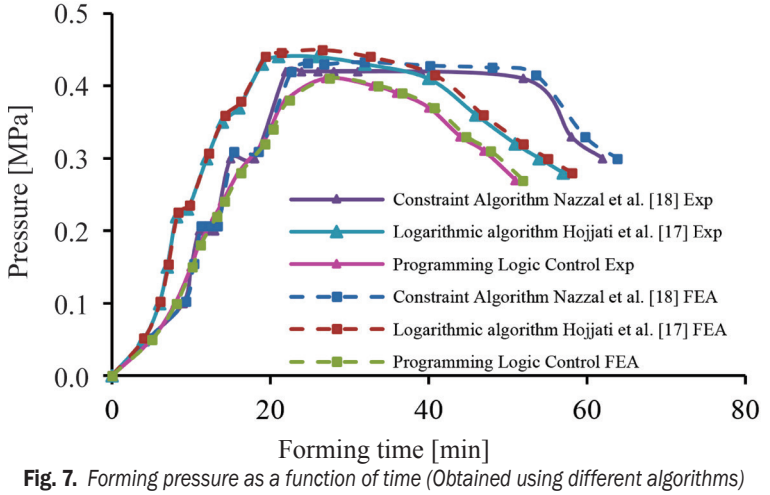

Fig. 7. *Forming pressure as a function of time (Obtained using different algorithms)*

The thickness distribution is shown as a function of distance from the centre of the split die in all these three different pressure control methods. The thinning factors [17] for all pressure control methods are shown in Table 3. The thinning factor values obtained from finite element model have been found to be very close to those obtained from actual experiments with a maximum error of 3 % in constraint algorithm method. The thinning factor with a function of different pressure control method by the FEA and the values obtained through the experiments are found to agree very well with a minimum percentage error as shown in Table 3.

Table 3. *Thinning factor in different pressure control method*

S. no	Pressure forming method	Thinning factor [%]		% of error
		Experiment	FEA	
1	Constraint algorithm	78.26	80.61	3.00
2	Logarithmic algorithm	80.40	82.41	2.50
3	PLC approach	88.41	89.96	1.75

The thinning factor [17] plays a vital role in predicting the uniformity of thickness in the formed profile with the highest value indicating more uniform thickness distribution in the product. Table 3 shows that the PLC approach has a higher thinning factor (88.41 %) value in comparison to the logarithmic algorithm (thinning factor 80.4 %) and the constraint algorithm (thinning factor 78.26 %). Furthermore, Fig. 8 shows that the PLC process has obtained optimum (minimum) thickness variation when compared to the constraint and logarithmic algorithm approaches. Therefore, the experimental results, helps understanding that; in this case, the uniform thickness has been achieved using the newly developed pressure control method of PLC approach.

In the fully formed component, more thickness variations were observed at the die entry, taper angle, die corner, hemispherical and micro-forming regions with the constraint algorithm method due to the maximum pressure magnitude interval step followed in this algorithm. Similarly, the use of the logarithmic algorithm method is also not so uniform in all the regions of the die due to the time step interval. However, in the PLC process, thickness distribution can be found to be very close to uniform (optimum thickness variation) in all the regions of the die, as evident from Fig. 8. The reasons for the even thickness distribution in this case could be the very small, and gradual increments possible either in displacement or in time, thereby reducing flow stress oscillations significantly, even in die corner regions.

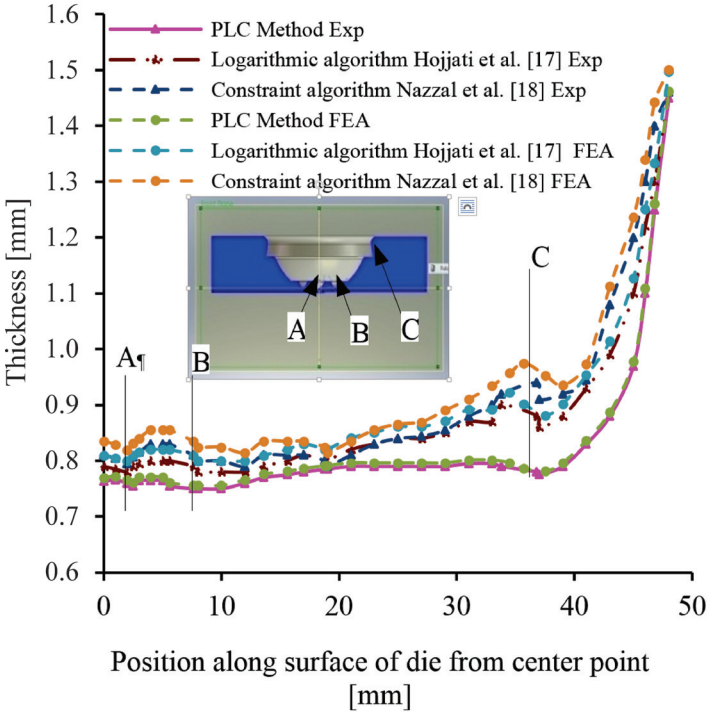

Fig. 8. *Thickness distribution along the die surface with different pressure control algorithm*

This approach can also be more flexible and highly precise to regulate the flow of pressure for slow filling in corner regions, thereby eliminating the defects because of otherwise fast filling. For this reason, the PLC approach has the best pressure prediction method to control the flow and strain rate throughout the process and obtained optimum thickness variation (uniform thickness distribution) in multiple curved regions.

3.3 Effect of Strain Rate Sensitivity Index on Thickness Distribution and Pressure Time Cycle

The strain rate sensitivity index (m) plays an important role in the SPF process, since it affects the forming pressure and strain rate. The influence of m values on the pressure-time cycle profile and thickness distribution is shown in Figs. 9 and 10. Fig. 9 clearly shows that a low value of strain rate sensitivity index (m = 0.3) leads to a dramatic increase in the forming pressure (1.43 MPa) required to fill the die cavity uniformly in a multi-dome profile. In contrast, an increase in the m (0.5) value increases the forming time (104 minutes) required to complete filling the cavity of the multidimensional profile, despite reports [4] and [20] which suggest that higher 'm' values produce a homogeneous thickness distribution in simple-shaped components. In the present PLC process, a significant variation in thickness is found during very low and very high 'm' values which can be seen in Fig. 10.

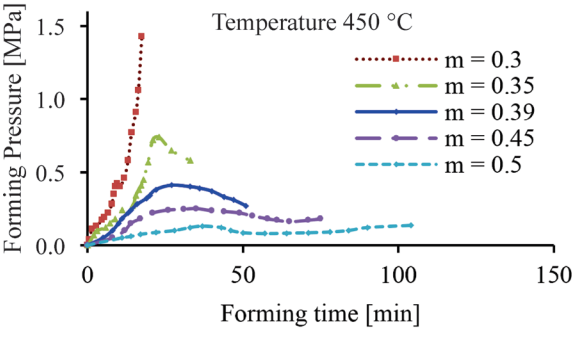

Fig. 9. *Influence of the m value on the pressure time cycle*

Figs. 9 and 10 show that at an optimum 'm' value of 0.39 filling the die cavity has been achieved with nominal (maximum) forming of pressure is 0.398 MPa and at a relatively short time of 52.12 minutes, which has also produced uniform thickness distribution in the complex profile. Moreover, with the optimum 'm' (0.39) value, the variation in the thickness profile in the die corner and entry regions is insignificant, as the optimal value results in greater resistance to neck formation and, therefore, good material flow [21] in the multiple curved die entry regions is ensured.

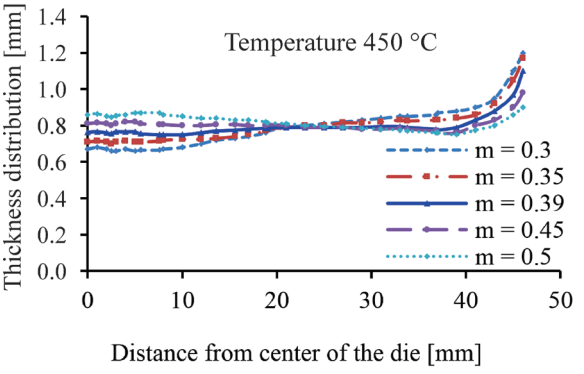

Fig. 10. Influence of the m value on the thickness distribution

3.4 Effect of Friction Coefficient on Thickness Profile

The coefficient of friction is an important factor that influences the forming pressure during superplastic forming. Most of the published works have focused on simple shapes, such as hemispherical, circular, cone, and also with a relatively simple rectangular die. In this work, the effect of the coefficient of friction on thickness variations in different die entry and die corner regions has been simulated using Coulomb's friction model [17] method in FEA and a complex with multi-dimensional profile. The SPF process is numerically simulated with coefficient of friction values of 0.0, 0.2, and 0.4 [16] and [17] and their effects on important parameters, such as thickness variations are studied and the results are reported in Fig. 11.

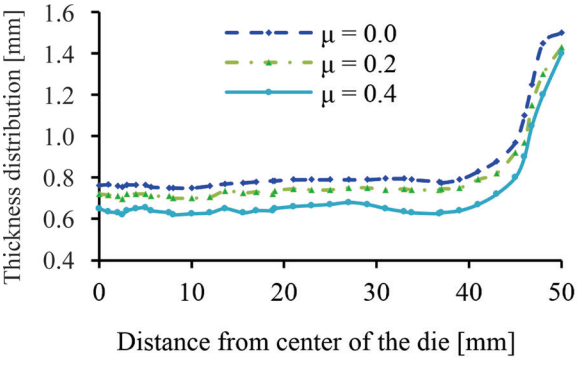

Fig. 11. *Thickness distribution along the die surface with different coefficient of friction using PLC method*

When the material starts flowing, the initial contact between the die and the blank takes place at the die entry point. Due to sliding under pressure,

the thickness of the profile varies as a function of the friction coefficient. The deviation in thickness distribution is high in the forming profile when the coefficient of friction is high. Fig. 11 shows that lower coefficient of friction results in uniform thinning at the die entry and the die corner regions. Higher coefficient of friction results in non-uniform thinning which in turn leads to higher deviation in thickness values in the die entry and corner regions. A higher value of friction coefficient also results in localized thinning in the profile in regions other than die entry regions of the dome. Lower values of friction coefficient lead to smooth material flow into the die cavity, obtained by controlling of applied pressure within the PLC, and result in uniform thickness distribution in die entry and corner regions of the profile. Therefore, using the PLC method, uniform thickness distribution has been predicted even for a multidimensional profile by keeping the coefficient of friction at a lower value, which further validates the utility of the approach.

3.5 Microstructure in Parent Metal of AA 5083 Aluminium Alloy

The optical microstructure analysis has been carried out in the parent metal at room temperature. The optical microstructures of the initial as-received material are shown in Fig. 12, which reveals coarse equiaxed grains.

Fig. 12. *Microstructure of parent metal*

3.6 Microstructure Analysis in Three-Stage Multi-dimensional Formed Component

The microstructure analysis has been carried out at four locations: taper angle corner point, die corner points and midpoint of micro-forming region of three stage multidimensional formed components obtained by using the PLC method at a temperature of 450 °C. The microstructure locations are shown in Fig. 13.

From Fig. 13, it is seen that the matrix shows elongated grains of Mg_2Si particles/grains in aluminium solid solution. The finest grain size could be seen in optical microstructures of superplastic formed components. Further microstructures in all the locations are identical and no stress affected microstructure could be seen. With the PLC method, the material flow at a very slow rate to fill the die corner regions, so there is no significant change in microstructure of the formed component.

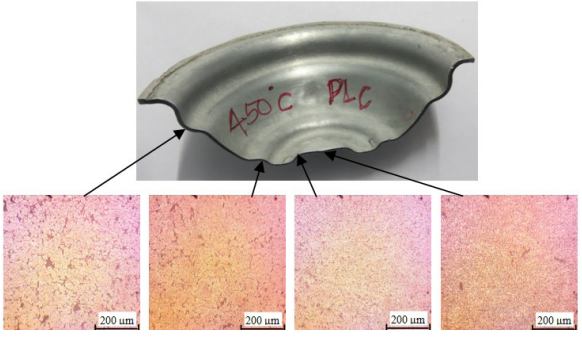

Fig. 13. *Microstructure at various points on formed profile by using PLC approach*

4 CONCLUSION

The PLC approach has been employed in the superplastic forming process of AA 5083 alloy in order to predict the optimum pressure required to improve the uniform thickness profile in multi-geometrical components. The pressure-time cycle, obtained based on this approach, has shown uniform thickness distribution in the multidimensional profile with minimum forming time when compared to the results obtained using constrained and logarithmic control algorithms. The finite element method has been used to ensure accurate control of the pressure into a multi-stage profile to improve the thickness profile without wrinkles. The pressure profile predicted by the FEM (ABAQUS) compared very well with the experimental results.

The developed PLC system is found to effectively control superplastic forming of the AA5083 alloy sheet into the cavity without any significant necking. Thickness distribution in the die entry and corner regions has been found to be uniform for a complex multidimensional profile, such as the one used in this work. The PLC circuit has also been found to be effective in adjusting the magnitude and duration of the pressure cycle, to optimize thickness quality, and to achieve wrinkle-free superplastic formed multidimensional components. The results reveal

FEM to be a very reliable method for analysing and optimizing the superplastic forming process by varying friction levels and strain rate sensitivity index both of which help to predict important parameters, such as thickness distribution, forming time, and pressure profile.

5 REFERENCES

[1] Ghosh, A.K., Hamilton, C.H. (1980). Superplastic forming of a long rectangular box section-analysis and experiment, processing modeling, fundamentals and application of metals. *Proceeding of American Society of Metals, Materials and Process*, p. 303-331.

[2] Rama, SC., Chandra, N. (1991). Development of a pressure prediction method for superplastic forming processes. *International Journal of Non-Linear Mechanics*, vol. 26, no. 5, p. 711-725, **DOI:10.1016/0020-7462(91)90022-L**.

[3] Luckey, S.G., Friedman, P.A., Xia, Z.C. (2004). Aspects of element formulation and strain rate control in the numerical modeling of superplastic forming. *Proceedings of advances in superplasticity and superplastic forming*. The Minerals, Metals and Materials Society, p. 371-380.

[4] Chen, Y., Kibble, K., Hall, R., Huang, X. (2001). Numerical analysis of superplastic blow forming of Ti-6Al-4V alloys. *Materials and Design*, vol. 22, no. 8, p. 679-685, **DOI:10.1016/S0261-3069(01) 00009-7**.

[5] Gusel, L., Rudolf, R., Brezocnik, M. (2015). Genetic based approach to predicting the elongation of drawn alloy. *International Journal of Simulation Modelling*, vol. 14, no. 1, p. 39-47, **DOI:10.2507/IJSIMM14(1)4.277**.

[6] Dutta, A., Mukherjee, AK. (1992). Superplastic forming: an analytical approach. *Journal of Material Science and Engineering: A*, vol. 157, no. 1, p. 9-13, **DOI:10.1016/0921-5093(92)90092-F**.

[7] Jarrar, F.S., Abu-Farha, F.K., Hector, L.G.Jr., Khraisheh, M.K.(2009). Simulation of high-temperature AA5083 bulge forming with hardening/softening material model. *Journal of Material Engineering Performance*, vol. 18, p. 863-870, **DOI:10.1007/S11665-008-9322-5**.

[8] Balasubramanian, M., Ganesh, P., Ramanathan, K., Senthil Kumar, V.S. (2015).Superplastic forming of a three-stage hemispherical 5083 Aluminium profile. *Strojniški vestnik – Journal of Mechanical Engineering*, vol. 61, no. 6, p. 365-373, **DOI:10.5545/sv-jme.2014.2178**.

[9] Carrino, L., Giuliano, G.,Napolitana, G. (2003). A posteriori optimisation of the forming pressure in superplastic forming processes by the finite element method. *Finite Element in Analysis and Design*, vol. 39, no. 11, p. 1083-1093, **DOI:10.1016/S0168-874X(02)00158-0**.

[10] Snippe, Q.H.C., Meinders, T. (2011). Mechanical experiments on the superplastic material ALNOVI-1, including leak information. *Journal of Material Science and Engineering: A*, vol. 528, no. 3, p. 950-960, **DOI:10.1016/j.msea.2010.09.075**.

[11] Dezelak, M., Stepisnik, A., Pahole, I., Ficko, M. (2014). Evaluation of twist springback prediction after an AHSS forming process. *International Journal of Simulation Modelling*, vol. 13, no. 2, p. 171-182, **DOI:10.2507/IJSIMM13(2)4.261**.

[12] Hambli, R., Potiron, A., Guerin, F., Dumon, B. (2001). Numerical pressure prediction algorithm of superplastic forming processing using 2D and 3D models. *Journal of Materials Processing Technology*, vol. 112, no. 1, p. 83-90, **DOI:10.1016/S0924-0136(01)00549-0**.

[13] Nițu, E., Iordache, M., Marincei, L., Charpentier, I., Le Coz, G., Ferron, G., Ungureanu, I. (2011). FE-modeling of cold rolling by in-feed method of circular grooves. *Strojniški vestnik -Journal of Mechanical Engineering*, vol. 57, no. 9, p. 667-673, **DOI:10.5545/sv-jme.2010.244**.

[14] Luckey, S.G.Jr., Friedman, P.A., Weinmann, K.J. (2007). Correlation of finite element analysis to superplastic forming experiments. *Journal of Materials Processing Technology*, vol. 194, no. 1-3, p. 30-37, **DOI:10.1016/j.jmatprotec.2007.03.122**.

[15] Aoura, Y., Boude, S., Santo, PD., Ouziz, L. (2011). Experimental validation of pressure cycle for superplastic forming of Ti–6Al–4V alloys. *International Journal of Research and Review in Mechatronics Design and Simulation*, vol. 1, no. 2, p. 32-36.

[16] Jarrar, F.S., Hector, L.G.Jr., Khraisheh, M.K., Bower, A.F. (2010). New approach to gas pressure profile prediction for high temperature AA5083 sheet forming. *Journal of Materials Processing Technology*, vol. 210, no. 6-7, p. 825-834, **DOI:10.1016/j.jmatprotec.2010.01.002**.

[17] Hojjati, M.H., Zoorabadi, M., Hosseinipour, S.J. (2008). Optimization of superplastic hydroforming process of Aluminium alloy 5083. *Journal of Materials Processing Technology*, vol. 205, no. 1-3, p. 482-488, **DOI:10.1016/j.jmatprotec.2007.11.208**.

[18] Nazzal, M.A., Khraisheh, M.K., Darras, B.M. (2004). Finite element modeling and optimization of superplastic forming using variable strain rate approach. *Journal of Materials Engineering and Performance*, vol. 13, no. 6, p. 691-699, **DOI:10.1361/10599490421321**.

[19] SenthilKumar, V.S., Viswanathan, D., Natarajan, S.(2006). Theoretical prediction and FEM analysis of superplastic forming of AA7475 aluminum alloy in a hemispherical die. *Journal of Materials Processing Technology*, vol. 173, no.3, p. 247251, **DOI:10.1016/j.jmatprotec.2005.04.112**.

[20] Li, G.Y., Tan, M.J.,Liew, K.M. (2004). Three-dimensional modeling and simulation of superplastic forming. *Journal of Materials Processing Technology*, vol. 150, no. 1-2, p. 76-83, **DOI:10.1016/j.jmatprotec.2004.01.023**.

[21] Cornfield, G.C., Johnson, R.H. (1970). The forming of superplastic sheet metal. *International Journal of Mechanical Science*, vol. 12, no. 6, p.479-490, **DOI:10.1016/0020-7403(70)90075-5**.

Strojniški vestnik - Journal of Mechanical Engineering 63(2017)4, 265-274
DOI:10.5545/sv-jme.2016.4264
Original Scientific Paper
Received for review: 2016-12-12
Received revised form: 2017-01-05
Accepted for publication: 2017-03-22
© 2017 Journal of Mechanical Engineering. All rights reserved.

A Surveillance of Direct-Firing System for Pulverized-Coal Using Statistically Treated Signals from Intrusive Electrostatic Sensors

Boštjan Jurjevčič – Andrej Senegačnik – Igor Kuštrin*
University of Ljubljana, Faculty of Mechanical Engineering, Slovenia

Operational surveillance of all vital parts of thermal power plants is nowadays more important than any time before due to requirements for their extremely flexible operation resulting from intermittent behaviour of renewable energy sources. New methods for online measuring of pneumatic transport provide new possibilities for control and early fault detection of coal grinding and conveying system in direct-fired power plant boilers. Arrays of intrusive electrostatic sensors are an attractive option due to their inexpensive application and good spatial sensitivity required in large rectangular ducts of pulverized-coal systems. In this study, statistically treated electrostatic signals are used for detection of unexpected change in operating regime of coal grinding and conveying. Model-based and model-free autocorrelation reduction techniques are used to reduce the inherent autocorrelation of data. Forming batch-means of data, a model-free autocorrelation reduction technique is proposed in combination with an autoregressive-integrated-moving-average (ARIMA) method. Residuals between real and ARIMA-model fitted data are entered into exponentially-weighted-moving-average (EWMA) control chart for statistical surveillance of the process. The robust and cost-effective measuring method accompanied with a simple and intuitive control scheme proves to be effective for early fault detection of the pulverized-coal preparation system.

Keywords: ARIMA model, control chart, fan mill, fault detection, pneumatic transport, statistical modelling

Highlights

- *Electrostatic method captures characteristics of gas-solid flow in the duct.*
- *Statistical process control uses electrostatic-sensors signals for monitoring of coal-grinding system.*
- *Successive autocorrelation reductions are employed: model-free and model-based.*
- *EWMA control chart of ARIMA-model residuals can detect unexpected coal-grinding regime changes.*

0 INTRODUCTION

Thermal power plants are nowadays forced to operate in extremely flexible mode [1] to help maintaining balance between the electricity production and consumption [2] and [3]. Flexibility of pulverized-coal direct-fired thermal power plant is limited by instability of combustion process at low boiler loads and sudden changes of coal composition. The need for measurement and control of every subsystem in the power plant to ensure stable operation and reduce emissions of harmful substances is necessary more than ever.

Characterization of pulverized coal pneumatic transport on its way from the mill to the furnace can provide important information and help improving the combustion [4] and [5]. Besides ensuring optimal pulverized-coal quantity and quality to burners, early detection of unexpected regime changes or faults is very welcome. Mill-overload condition is a very common and unwanted fault in pulverized-coal direct-fired steam boilers, which can cause large fluctuations in boiler's and consequently power plant's output [5] and [6]. Even a boiler trip can occur in the case of late or inappropriate intervention. Usually the danger of mill overloading is detected by observing the temperature of pulverized-coal-gas mixture exiting the mill [1] and [5]. Low temperature or increased gradient of temperature decrease of pulverized-coal-gas mixture are usually used as triggers for mill-overload condition alarms. Experience shows that this type of detection can often be misleading or late. Besides this, mill's differential pressure and measurements of mill-motor amperage, vibrations [6], [7] and energy balance of mill [8] are used for monitoring of grinding and conveying system. In fact, controlled variables mentioned above are only indirectly related to coal flow. Nowadays, several techniques can be applied for direct observation of mass flow, velocity, concentration of particles, etc. in pneumatic transport [9] and [10], which have a great potential to improve control of grinding and transport process [6]. However, in case of direct-fired boilers with pulverized coal all known methods have limited applicability.

An electrostatic measuring technique based on intrusive sensors tested numerically [11] and experimentally [4] and [12] accompanied with appropriate data acquisition system is a promising one. Direct contact of sensors and coal-particles enables quick and adequate characterisation of the two-phase flow. Various signal-processing methods in time and frequency domain need to be applied to measured signal time series generated by electrostatic

*Corr. Author's Address: University of Ljubljana, Faculty of Mechanical Engineering, Aškerčeva 6, 1000 Ljubljana, Slovenia, igor.kustrin@fs.uni-lj.si

sensors, since raw data itself do not explicitly reflect flow characteristics. Mean or root-mean-square values of the signal with an appropriate calibration are typically employed.

Statistical analysis and modelling of time series can be applied for early detection of unexpected fluctuations of pneumatic transport. Various techniques can be applied for modelling of fluctuating time series [13]. For non-deterministic, stochastic time series [14], linear modelling based on statistical approach can be more appropriate than non-linear. Control charts are able to distinguish between common and special causes in numerous industrial applications [15], [16] and are widely used in control systems of thermal power plants [17] and [18]. Traditional Shewhart's, cumulative-sum (CUSUM) and exponentially-weighted-moving-average (EWMA) control charts are frequently used in European power industry [19], [20] and can have better performance than non-standard charts [21] and [16]. CUSUM control chart weighs all past measurements equally. In order to detect sudden transients, frequent resetting of monitoring is inevitable. On the EWMA control chart, data is exponentially weighted. As data accumulate, the importance of past data diminishes. EWMA is therefore convenient for detection of quick transients while ignoring slow transients in non-stop operating processes. Furthermore, EWMA chart is simple and intuitive to implement and interpret [22] and [23].

The following sections describe the theoretical background of autocorrelation reduction and the basic principle of EWMA control charts. Afterwards, direct-firing system of a coal fired boiler is briefly described. An array of electrostatic sensors is implemented as a source of data for further processing. EWMA control chart of treated data was tested in the case of regime transitions of direct-firing system and finally employed for early detection of mill-overload situation.

1 THEORETICAL BACKGROUND

For statistical process control, the assumption of data being independent and identically distributed is essential [24] and [25]. In reality, this is practically never the case. When the normality assumption is violated to a slight or moderate degree, control charts will still work reasonably well [24]. In contrast, conventional control charts do not perform well if the observations exhibit even low levels of correlation over time. Specifically, they will give misleading results in the form of too many false alarms if the data are positively correlated [20] and [23]. Nowadays we are frequently dealing with autocorrelated data because modern equipment enables high frequency sampling. Less frequent sampling can reduce the autocorrelation, but it can cause majority of information being disregarded [23]. Methods for the reduction of autocorrelation are needed.

Monitoring of autocorrelated processes by calculating the means of small batches of data separated by skipped observations was proposed in [26]. Moreover, better performance can be achieved by calculating batch-means without skipping any observations [25].

Another option to treat autocorrelated data is the algorithmic statistical process control. This technique incorporates the monitoring of residuals i.e. differences between actual and fitted data using an appropriate statistical model [16] and [27]. Autoregressive-integrated-moving-average (ARIMA) models appear to be a reasonable choice due to their high flexibility and need for very few assumptions [28].

1.1 Model-Free Autocorrelation Reduction

Unweighted batch means control chart is a form of model-free approach. It was proposed by [25] to break successive sequential observations into batches with equal weights assigned to every point in the batch. From the original time series of voltages U_1, U_2, ..., U_n unweighted mean U_j of j^{th} batch can be calculated as:

$$U_j = \frac{1}{b}\sum_{i=1}^{b} U_{b(j-1)+i} \quad \text{for } j = 1,2,\ldots,m, \tag{1}$$

where b is the number of samples per batch. In [25] it is recommended to choose such a batch size that yields the autocorrelation to 0.1 at lag 1. If time series is highly autocorrelated, increasing the batch size cannot sufficiently reduce the autocorrelation in reasonable lag time.

1.2 Model-Based Autocorrelation Reduction

The proposed model-based approach uses the ARIMA method. It incorporates a linear, strictly statistical model and a subset of time series analysis, developed by Box et al. [29]. Integers p, d and q are referring to autoregressive (AR), integrated (I) and moving average (MA) parts of the model respectively. The ARIMA method offers a potential for treating the time series that cannot be adequately treated by using an AR or an MA methods alone. Many advantages of the

ARIMA method were found and support the adequacy of ARIMA especially for short term forecasting of time series. The ARIMA model can be written as:

$$\left(1-\sum_{k=1}^{p}\alpha_k L^k\right)(1-L)^d U_t=\left(1+\sum_{k=1}^{q}\beta_k L^k\right)\varepsilon_t+\tilde{\mu}, \quad (2)$$

for $t=1,2,\ldots,n$ with:

$$\tilde{\mu}=\mu-\alpha_1\mu-\ldots-\alpha_p\mu, \quad (3)$$

where U_t is a measured value at time t, μ is a mean of past measured values, α_1, …, α_p are real numbers, ε_t is a random error at time t, α_k are autoregression coefficients, β_k is a moving average coefficient, $(1–L)$ is a differentiator operator and L is a back shift operator. Past data U_1, U_2, U_3, …, $U_{t–1}$ are used to determine values of model parameters, Eqs. (2) and (3). Model is then used for calculation of surrogate (fitted) data $\hat{U}_t$. The residual e_t is calculated as:

$$e_t=U_t-\hat{U}_t. \quad (4)$$

The residuals e_t are approximately normally and independently distributed with zero mean and variance being constant [24].

1.3 EWMA Control Chart

While other control charts treat rational subgroups of samples individually, the EWMA chart tracks the exponentially-weighted-moving-average of all prior sample means. EWMA weights samples in geometrically decreasing order so that the most recent samples are weighted most highly, whereas the most distant samples are almost uninfluential [24]. According to EWMA, a smoothed exponentially weighted time series of calculated variables z_t is defined as:

$$z_t=\lambda\cdot e_t+(1-\lambda)z_{t-1}, \quad \text{for } t=1,2,\ldots,n, \quad (5)$$

where e_t is a residual at time t, and $0<\lambda\leq 1$ is a smoothing constant. Starting value z_0, which is required for calculation of z_1, is usually set to the mean of preliminary data. Lower λ provides higher degree of the smoothing. Upper control limit UCL_t (+) and lower control limits LCL_t (–) are calculated as:

$$CL_t=\pm k\sigma_{e,t}\sqrt{\frac{\lambda}{2-\lambda}\left[1-(1-\lambda)^{2t}\right]}, \quad (6)$$

for t = 1, 2, ..., n, where k is a control limit factor and $\sigma_{e,t}$ is a standard deviation of measured time series $e_1, e_2, \ldots, e_t$. Because the expression in square brackets with increasing number of samples converges to 1, UCL_t and LCL_t approach constant values.

EWMA control chart can be applied to the sequence of residuals that are not autocorrelated if a model is properly chosen [27]. Either Shewhart or EWMA control charts of measured data can be employed for detection of regime change. In order to cover all regimes and simultaneously detect transitions between different regimes, it is more convenient to apply residuals instead of measured data into the control chart. Consequently, the control limits do not change at every change of regime, which is the case in conditional monitoring. The use of ARIMA residuals as EWMA inputs additionally reduces the autocorrelation and covers all regimes of operation.

2 DESCRIPTION OF MEASURING PRINCIPLE AND DATA PROCESSING

The method was employed and validated on a lignite grinding system of a 345 MW power plant with direct-firing system. Each of the six fan/impact-type mills feeds pulverized lignite to the four burner nozzles. The grinding system is shown in Fig. 1. Operating parameters are adjusted by changing the feeder and the mill rotational speed (Table 1). The pulverized-lignite conveying duct is physically divided into four partitions.

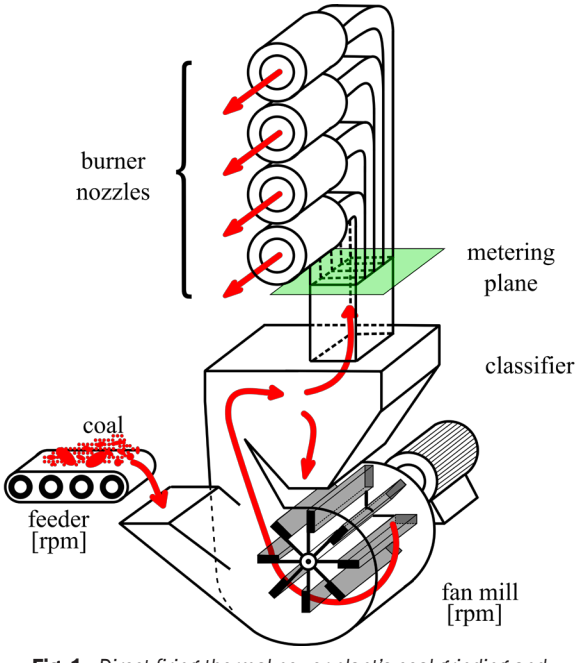

Fig. 1. *Direct-firing thermal power plant's coal grinding and conveying system with burner nozzles*

Table 1. *Operating regimes of fan mill and coal feeder*

Operating points	M457 F71	M457 F140	M487 F70	M486 F140
n_{mill} [rpm]	457	457	487	486
n_{feeder} [rpm]	71	140	70	140

Each partition leads to one of the four burner nozzles. The metering plane indicates the location where the electrostatic sensors are mounted.

The measuring system consists of eight rod-type electrostatic sensors: two sensors per one burner nozzle (Fig. 2). The system is described in detail in **[4]** and **[5]**.

The signals of electrostatic sensors depend on the mass flow, the velocity, the electrical properties, the chemical composition of the particles and the dimensions of the sensors **[4]** and **[30]**. These relations have been used as a measuring principle for the velocity, the mass flow and the concentration of solid particles in many industrial applications. In this particular case, only the mass flow and the velocity of the particles can change rapidly enough to be qualified as a sudden transient. All other variables can be assumed being constant or at least very slowly changing. Each sensor is a source of its respective voltage time series. Therefore, the voltage time series sourced by each sensor can be written as:

$$U_{u,t} = \sqrt{C \cdot v^4{}_{u,t} \cdot q_{m,u,t}} \quad t = 1,2,\ldots,n, \tag{7}$$

where v and q_m are the particles' velocity and mass flow and C is the constant comprising all other less influential variables. Subscripts u and t refer to particular electrostatic sensor and time of sampling respectively. For further analysis, a time series of average voltage of all sensors u_1 to u_8 is used:

$$U_t = \frac{1}{8}\sum_{u=1}^{8} U_{u,t}, \quad \text{for } t = 1,2,\ldots,n. \tag{8}$$

Time intervals between individual coal particle collisions to the electrostatic sensor are very short. For meaningful electrostatic-mass-flow or electrostatic-concentration measurements, which use the signals of the same sensors but they are not covered by this study, high sampling rate is required. Fluctuations of two-phase flow caused by more or less dense particle clusters are slower. Furthermore, combustion system response to certain occurrences and the operator ability to take actions are even slower. Therefore, high sample rates are needed to assess the characteristics of the pulverized-coal pneumatic transport. Frequent sampling causes neighbouring data to be highly autocorrelated which is undesirable for statistical analysis that requires the data to be independent **[16]** and **[24]**. In order to cover different time scales with minimal discard of information and at the same time reduce the autocorrelation, we propose the subsequent model-free and model-based autocorrelation reduction according to the following procedure:

- calculation of batch means of past measured voltages (model-free autocorrelation reduction),
- fitting of ARIMA model to the sequence of batch means and calculation of residuals i.e. differences between measured and ARIMA-model fitted voltages (model based autocorrelation reduction),
- EWMA control chart analysis of residuals.

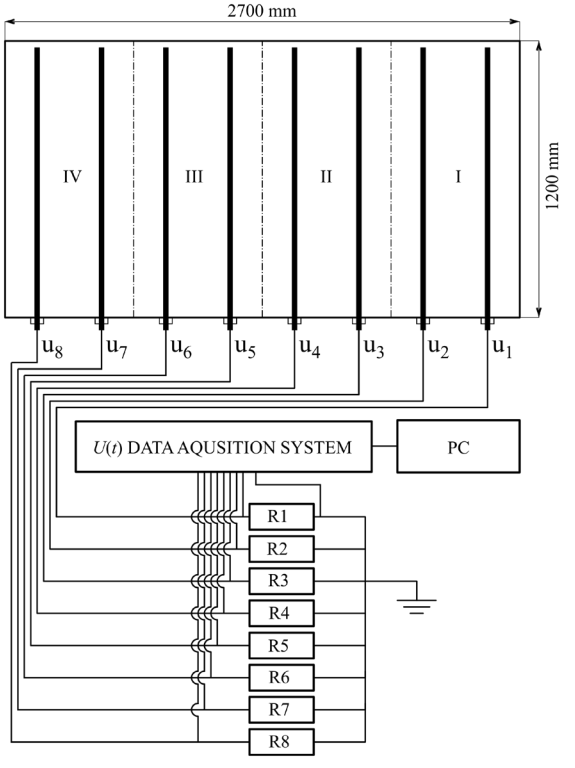

Fig. 2. *Cross-section of the duct in the metering plane with four partitions (I – IV) and installation positions for rod-type sensors with measuring scheme*

For the purpose of this analysis, two different types of transient situations are analysed:

- transitions between different operating regimes (Table 1),
- occurrence of mill overload condition.

The four operating regimes are described and commented in detail in **[4]**. In Table 1 feeder rotational speed is annotated by "F" and mill rotational speed by "M". Mill-overload condition is described and commented in detail in **[5]**.

The total duration of the four operating regimes and accompanying transitions was 4 hours. Voltages were measured with a sample rate of 1000 Hz. Two sets of data were archived:

- set of raw data: using temporary recorder,
- set of smoothed data: using power plant's installed data-acquisition and control system (DCS).

Smoothing was done by calculation the moving averages of five last means of batches each containing 1000 readings.

The total duration of the mill overload condition and its resolving was approximately 60 minutes. Only set of smoothed data was archived during this event using plant DCS.

The measurements acquired during the four regimes (Table 1) and the transitions between them were used for adjusting the parameters of batch-means and ARIMA techniques. The measurements acquired during the mill-overload condition were used to verify the response of the proposed method to the development of a realistic and unwanted transient.

3 RESULTS AND DISCUSSION

3.1 Time Series Analysis

Fig. 3a shows 100-s interval of non-smoothed reduced voltage time series (Eq. 8) and smoothed time series acquired from electrostatic sensors in operating regime M486 F140. Coal-particles' collisions to the sensor and their moving through the sensing area are causing highly fluctuating stochastic signal. Smoothed time series is the moving average of five batch-means with batch size *b* equal 1000.

Power spectral density, as one of the most popular approach for fluctuating-time-series analysis, was applied to interval of the non-smoothed voltage time series as is shown in Fig. 3b. A broad peak in power occurs at relatively low frequencies (lower than 1 Hz) and then power slightly decreases towards higher frequencies. At approximately 40 Hz the power starts to decrease more rapidly. Lower frequency fluctuations of the reduced voltage time series are caused by alternate motion of denser and diluter clusters of coal particles. The distinctive low frequencies for electrostatic measurements in two-phase gas-solid flow are in compliance with other studies [11].

Autocorrelation function (Fig. 3c) evidently shows that the neighbouring data are highly correlated. Autocorrelation factor at lag 1 is 0.99. The slowly decreasing autocorrelation function has a concentration of power spectral density in the lowest frequencies, which is in accordance with findings in [31].

3.2 Autocorrelation Analysis and Autocorrelation Reduction

High autocorrelation of the data is in stark contrast to data randomness that is an underlying assumption for statistic control of process. Autocorrelation needs to be reduced to an acceptable level. Approximately 95 % of the sample autocorrelations should fall

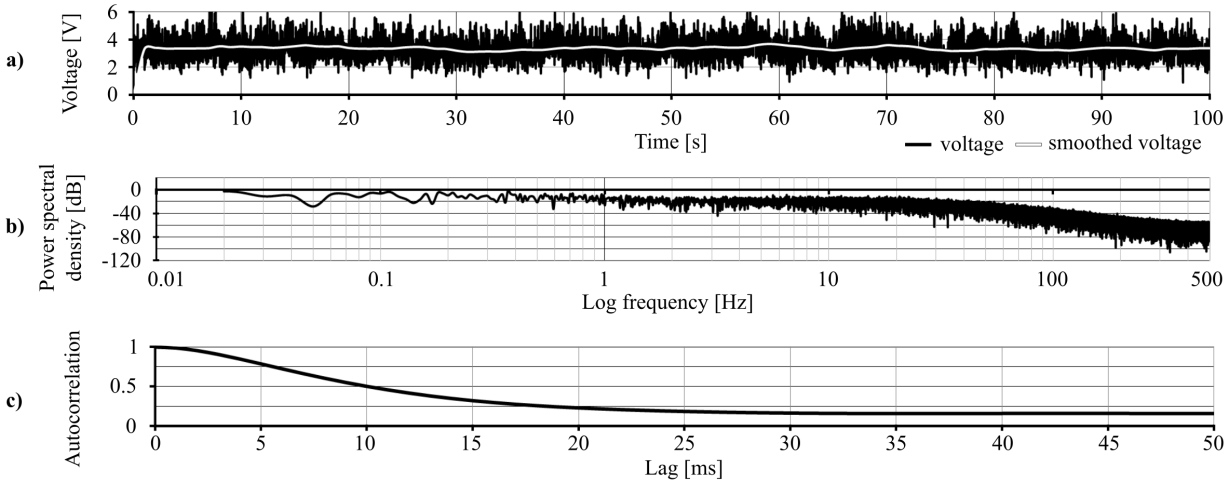

Fig. 3. *a) Segment of non-smoothed and smoothed reduced voltage time series, b) power spectral density and c) autocorrelation plot of the reduced non-smoothed voltage for the operating regime M486 F140*

between the bounds $\pm 1.96/n^{1/2}$ since 1.96 is the 0.975 quantile of standard normal distribution [31].

Unweighted batch-means technique of autocorrelation reduction was applied. Autocorrelation functions for raw and smoothed reduced time series in the operating regime M486 F140 are shown on Fig. 4. The solid line refers to the time series of raw data before automatic smoothing (section 2: set of raw data).

Other lines refer to the reduced time series after the automatic smoothing. The long-dashed line shows autocorrelation function of automatically smoothed average time series before autocorrelation reduction (section 2, set of smoothed data, $b = 1$).

The short-dashed line, the dotted-line and dash-dotted-line show autocorrelation functions for different degrees of autocorrelation reduction based on means of batches with $b = 5$, $b = 10$ and $b = 30$ respectively. The smoothed time series has slightly lower autocorrelation factor at lag = 1 than the raw-data time series. They both display high degree of autocorrelation and need autocorrelation reduction before being a suitable input to control chart. The autocorrelation reduction increases with increasing b, which is in accordance with [25]. It should be noted that for raw data lag = 1 corresponds to 1 ms, for batch size $b = 1$ lag = 1 corresponds to 1 s, for batch size $b = 5$ lag = 1 corresponds to 5 s, etc.

Different operating regimes with their distinct velocities, mass flows and mean particles' sizes in pneumatic transport have significant influence on autocorrelation. Fig. 5 shows autocorrelation functions for smoothed reduced time series with $b = 10$ for different operating regimes. Regimes at the higher feeder speed, i.e. higher mass flow, (M457 F140 and M486 F140) display higher degree of autocorrelation. Higher concentration of particles causes smoother flow, higher self-similarity in time and consequently higher autocorrelation. At the same feeder speed, regimes with the higher rotational speed of the mill display lower autocorrelation of data (M486 F140 vs M457 F140) due to more turbulent flow.

Even after application of batch means reduction technique, the autocorrelation is still too high for the assumption of randomness for all the observed operating regimes. The lowest autocorrelation factor at lag = 1 and $b = 10$ equals 0.29 and belongs to regime M487 F70.

Additional technique for reduction of autocorrelation is required. ARIMA models may be a suitable solution for highly autocorrelated data with predominantly low frequencies [31] and [29]. If model parameters are set correctly, the residuals of time series model can have negligible autocorrelation [24] and [25]. Table 2 comprises the results of different ARIMA model parameters p, d and q. The ARIMA parameters were determined iteratively according to Akaike information criterion for finite samples (AICc). AICc is one of frequently used criterions [32]. The lowest AICc number indicates the best fitted model to data.

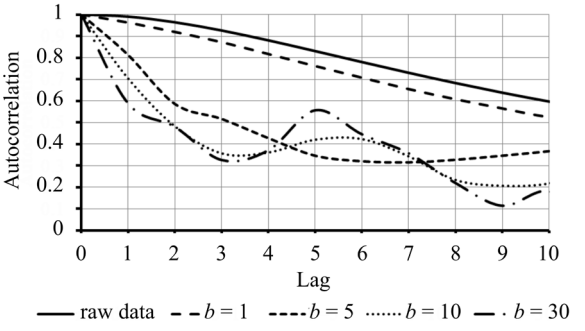

Fig. 4. *Autocorrelation functions of raw and smoothed reduced time series with different batch sizes b for operating regime M486 F140*

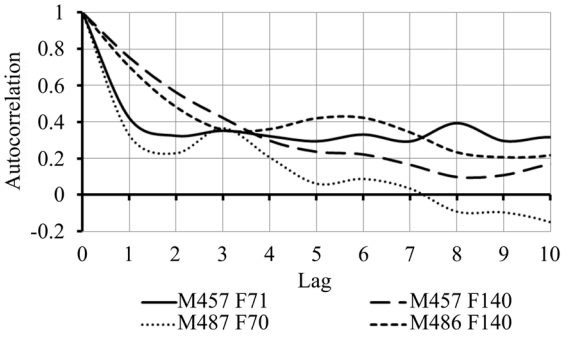

Fig. 5. *Autocorrelation functions of batch-means of smoothed reduced time series, with b=10 for various operating regimes*

Since different parameter values of ARIMA model were obtained for different operating regimes (Table 2) it would be more convenient to find a universal model that fits all regimes. For this purpose, average values of parameters of ARIMA models for all operating regimes for each batch size were calculated (third row for each batch size). The second row contains AICc values of best-fit ARIMA models for respective regimes. The fifth row contains AICc values of universal ARIMA model using nearest integers of average parameters of respective ARIMA models. Comparison of AICc values shows that the use of universal model is justifiable since it provides satisfactory results and simplifies the calculation procedure.

Preceding batch-means autocorrelation reduction with larger b reduces the values of ARIMA model parameters.

3.3 Results of EWMA Control Chart Analysis

The smoothed reduced time series were used for the analysis i.e. second type of data set (section 2). As mentioned above, the sets of data archived during transitions between operating regimes were used to choose the appropriate settings for autocorrelation reduction and control charts. Afterwards, the set of data archived during the mill-overload condition was used to verify the performance of the method during realistic unexpected fault in coal grinding and conveying system.

Table 2. *ARIMA parameters and AICc values at the specific operating regimes and the surrogate model for various batch sizes*

	Batch size b	Operating regime			
		M457 F71	M457 F140	M487 F70	M486 F140
p,d,q	1	3,1,1	3,1,3	4,1,3	1,1,1
AICc (p,d,q)		-4927	-5585	-4709	-4920
avg p,d,q		2.75, 1.00, 2.00			
integer avg p,d,q		3, 1, 2			
AICc (integer avg p,d,q)		-4933	-5569	-4660	-4937
p,d,q	5	3,1,2	1,0,2	3,1,2	1,1,2
AICc (p,d,q)		-602	-892	-697	-716
avg p,d,q		2.00, 0.75, 2.00			
integer avg p,d,q		2, 1, 2			
AICc (integer avg p,d,q)		-603	-883	-694	-714
p,d,q	10	1,1,1	1,0,0	0,1,1	2,1,1
AICc (p,d,q)		-275	-352	-266	-283
avg p,d,q		1.00, 0.75, 0.75			
integer avg p,d,q		1, 1, 1			
AICc (integer avg p,d,q)		-275	-346	-264	-283
p,d,q	30	0,1,1	1,0,0	1,0,0	0,1,1
AICc (p,d,q)		-120	-102	-117	-94
avg p,d,q		0.50, 0.50, 0.50			
integer avg p,d,q		1, 1, 1			
AICc (integer avg p,d,q)		-118	-96	-110	-92

3.3.1 EWMA Control Chart of Transitions Between Operating Regimes

Besides the ARIMA residuals and EWMA of ARIMA residuals, the reduced voltage time series with b = 10 is also plotted in Fig. 6 to illustrate the transitions between operating regimes. Smoothed residuals lying above the upper control limit (UCL) and below the lower control limit (LCL) are marked with red circles. Red circles only occur during transitions (A, B, C and D) and could be used as alarm for transients.

Table 3 shows effect of different input parameters to EWMA process control on the occurrence of alarms. Different batch sizes of model-free autocorrelation reduction and the corresponding universal ARIMA model from Table 2 were analysed along with different values of smoothing constant λ for EWMA in the range 0.05 to 0.5. The range of smoothing constant was chosen according to guidelines in [21]. Alarms appearing during stable operating regimes as well as in during transitions A, B, C and D were observed. Alarms occurring during the stable operating regime were denominated as false.

Table 3. *EWMA control chart settings for alarms detection during operation in different regimes with control limit factor k equal to 3*

	b	λ	Number of alarms in transition				Number of all alarms	Number of false alarms
			A	B	C	D		
ARIMA (3,1,2)	1	0.05	6	0	0	2	11	3
		0.10	12	0	0	6	28	10
		0.20	15	3	0	11	62	36
		0.30	15	1	0	11	83	56
		0.40	15	1	0	10	86	60
		0.50	10	1	1	13	100	75
ARIMA (2,1,2)	5	0.05	9	4	0	4	17	0
		0.10	13	8	0	8	29	0
		0.20	22	6	1	9	38	0
		0.30	20	4	0	8	34	2
		0.40	18	3	0	8	30	1
		0.50	18	2	0	7	30	3
ARIMA (1,1,1)	10	0.05	2	7	2	0	11	0
		0.10	6	6	1	4	17	0
		0.20	7	5	2	5	19	0
		0.30	9	5	1	5	20	0
		0.40	10	4	1	5	20	0
		0.50	10	2	0	4	17	1
ARIMA (1,1,1)	30	0.05	0	0	0	0	0	0
		0.10	1	3	0	0	4	0
		0.20	1	3	1	1	6	0
		0.30	2	2	1	1	6	0
		0.40	2	2	1	2	7	0
		0.50	3	2	0	2	7	0

The number of false alarms and total sum of all alarms decrease at higher batch size b. From this point of view, larger b is a better choice. The most robust smoothing constant is 0.2. Using this value, no falls alarms during stable regimes and at least one true alarm in transition C occur for all batch

sizes. Average run length (ARL) is usually used for strictly mathematical evaluation of statistical process control scheme [23]. Lower smoothing constant λ provides larger ARL values. When λ approaches zero, ARL approaches infinity [22]. Our findings are in accordance with [23] and [24] where the range of smoothing constant was proposed to be $0.05 < \lambda < 0.25$ and is usually set to 0.2.

3.3.2 EWMA Control Chart of Mill-Overload Condition

The chosen settings were tested using data archived during the unexpected mill-overload condition. This event is one of many archived by existing plant control system. All archived occurrences of mill-overload condition are very similar and lead to the same conclusions.

Fig. 7 shows EWMA control chart with $\lambda = 0.2$ for residuals of 10-s batch-means model-free and ARIMA (1, 1, 1) model-based autocorrelation reductions carried out consecutively. Relative reduced voltage time series with batches of 10 s is shown on the lower section of the chart together with relative values of the classifier temperature, pulverized-coal velocity and the rotational speeds of feeder and mill rotor. Zero represents the lowest and unity represents the highest value of a respective variable. A lower control limit (LCL) of classifier temperature is set to 175 °C. It is used for mill-overload detection with plant DCS. More details about measuring these parameters can be found in [5].

Two periods are marked on the chart. Period A covers the coal accumulation in the mill because the mill was unable to properly grind and transport the coal to the burner nozzles. During this period voltage, pulverized coal velocity and classifier temperature decreased rapidly indicating obstructed grinding and transporting of the pulverized coal. Operator intervened i.e. reduced the feeder speed when the temperature crossed the temperature LCL.

During period B the feeder speed was slightly increased along with tree-step increase of mill rotational speed which enabled the mill to grind and transport the accumulated coal to the burners. The classifier temperature and pulverized coal velocity returned back to higher levels indicating that grinding and transporting is back to normal. The pulverized-coal velocity was higher than in the period preceding the event because of lower coal mass flow. It must be noted that, despite lower coal mass flow, the voltage is higher than in the period preceding the event due to dominant effect of pulverized-coal velocity on the voltage (Eq. 1), [4]. EWMA control chart points out 12 alarms during period A.

The first EWMA alarm occurred approximately 2.5 minutes prior to temperature alarm which is crucial for the operator. Early EWMA alarms allow less radical manual interventions and consequently alleviate stress situations for both personnel and power

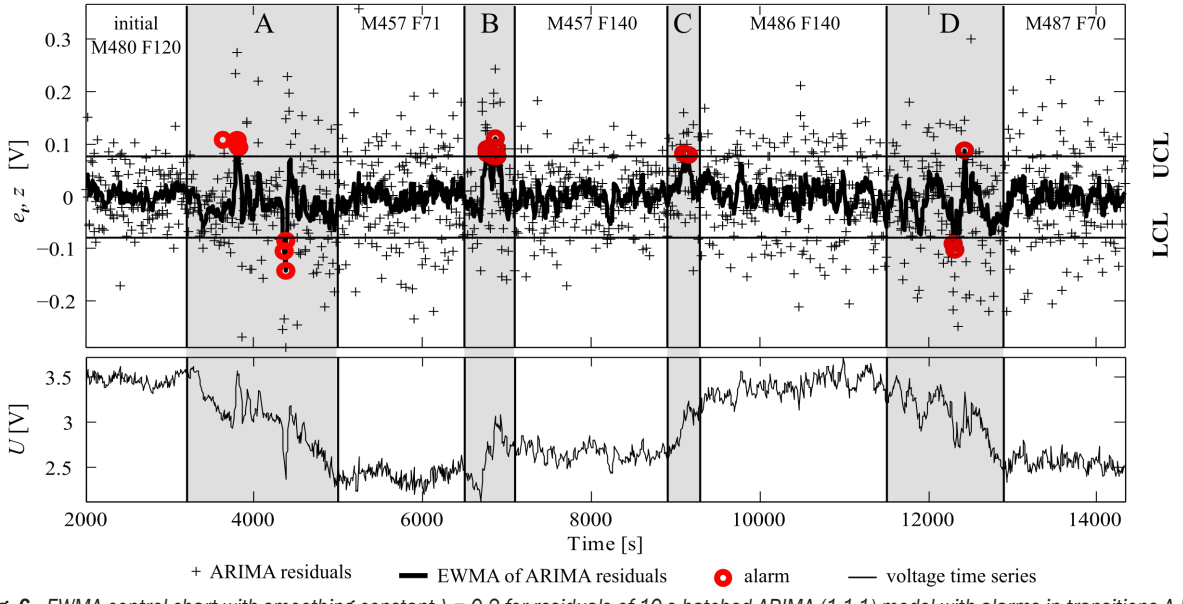

Fig. 6. *EWMA control chart with smoothing constant λ = 0.2 for residuals of 10-s-batched ARIMA (1,1,1) model with alarms in transitions A-D and reduced-smoothed voltage time series with b = 10 through all the operating regimes*

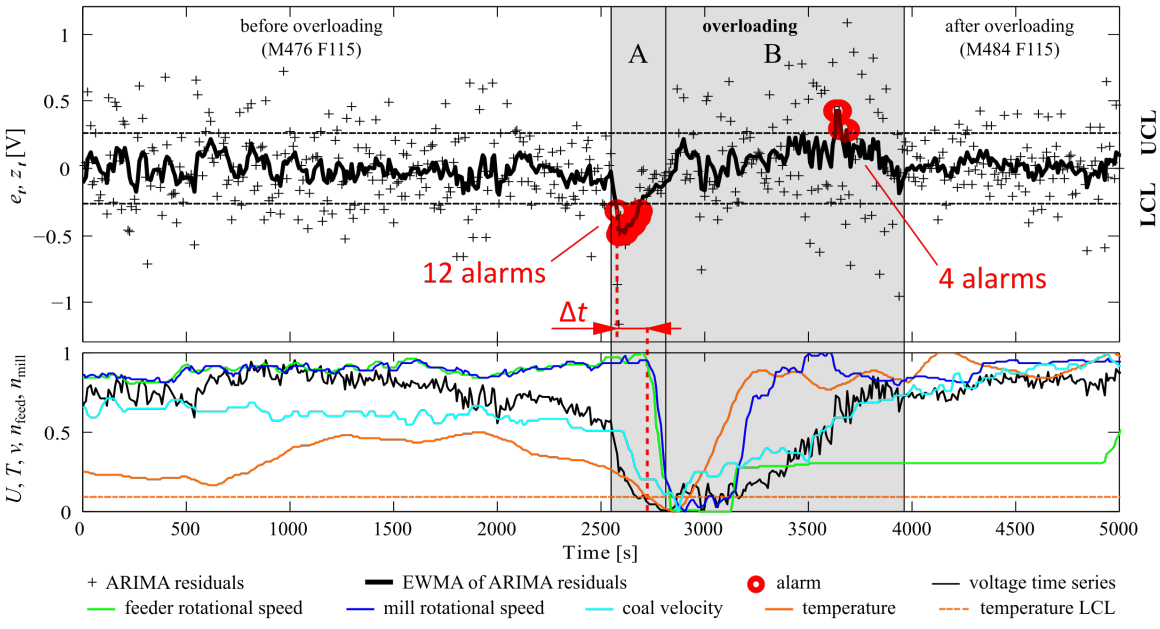

Fig. 7. *EWMA control chart for overloaded mill and time series of voltage, feeder rotational speed, mill rotational speed, coal velocity, temperature in classifier and temperature lower control limit*

plant system. Thus, sudden changes in combustion process can be prevented and consequently emission of harmful substances reduced. During period B four alarms occurred.These alarms are not considered false because they indicated actual sudden changes in operating regime caused by manual interventions.

4 CONCLUSION

The array of eight rod-type intrusive electrostatic sensors with accompanying instrumentation was employed in power plant's direct-fired boiler for measurements in pneumatic transport of pulverized coal. The archived voltage time series were statisticaly analysed. The most important conclusions regarding the use of electrostatic method for online measurements of pneumatic transport characteristics accompanied by statistical treating of measured signals are:

- The electrostatic measurement is robust and accurate enough to generate data which can be used for online statistical control of pneumatic transport.
- The inherent autocorrelation of acquired data needs to be reduced before statistic process control is applied. The combined model-free and ARIMA-model-based technique proved to be suitable for efficient autocorrelation reduction.
- EWMA control chart is simple to integrate into existing power plants' data acquisition and control systems for detection of potentially hazardous faults of coal-milling and conveying system. The batch size of data-batch-means variation was used to fine-tune and optimize the performance of EWMA control chart.
- Uncomplicated installation of electrostatic rod sensors with data acquisition system and simple control scheme of statistically treated data proved to be effective for early fault detection.

The presented technique proved to be applicable for early detection of mill-overload condition, which is only one of many potential faults of coal grinding and conveying systems. Other faults like unintentional increase of coal layer thickness caused by a foreign object, corrosion and abrasion induced feeder-base-plate perforations or extreme slugging of hot recirculated-flue-gas ducts can also be detected by using this method. This particular method is able to trigger a reliable alarm few minutes earlier than other techniques that are traditionally used for detection of this kind of faults. This improvement is very important for thermal power plants continuously operating in load-following mode.

5 REFERENCES

[1] Mercangoez, M., Poland, J. (2011). Coal Mill Modeling for Monitoring and Control. *IFAC Proceedings Volumes*, vol. 44, no. 1, p. 13163–13166, **DOI:10.3182/20110828-6-IT-1002.01144**.

[2] Starkloff, R., Alobaid, F., Karner, K., Epple, B., Schmitz, M., Boehm, F. (2015). Development and validation of a dynamic simulation model for a large coal-fired power plant. *Applied Thermal Engineering*, vol. 91, p. 496-506, **DOI:10.1016/j.applthermaleng.2015.08.015**.

[3] Corn, M., Černe, G., Papič, I., Atanasijević-Kunc, M. (2014). Improved integration of renewable energy sources with the participation of active customers. *Strojniški vestnik - Journal of Mechanical Engineering*, vol. 60, no. 4, p. 274-282, **DOI:10.5545/sv-jme.2013.1199**.

[4] Jurjevčič, B., Senegačnik, A., Drobnič, B., Kuštrin, I. (2015). The characterization of pulverized-coal pneumatic transport using an array of intrusive. *IEEE Transactions on Instrumentation and Measurement*, vol. 64, no. 12, p. 3434-3443, **DOI:10.1109/TIM.2015.2465731**.

[5] Kustrin, I., Lenart, J. (2015). Electrostatic sensors on a lignite - fired boiler for continuously monitoring the distribution and velocity of pulverized coal. *VGB Powertech*, no. 7, p. 33-37.

[6] Agrawal, V., Panigrahi, B.K., Subbarao, P.M.V. (2014). Review of control and fault diagnosis methods applied to coal mills. *Journal of Process Control*, vol. 32, p. 138-153, **DOI:10.1016/j.jprocont.2015.04.006**.

[7] Doukovska, L., Vassileva, S. (2013). Knowledge-based mill fan system technical condition prognosis. *WSEAS Transactions on Systems*, vol. 12, no. 8, p. 398-408.

[8] Odgaard, P.F., Mataji, B. (2007). Fault detection in coal mills used in power plants. *IFAC Proceedings Volumes*, vol. 39, no. 7, p. 177-182, **DOI:10.3182/20060625-4-CA-2906.00036**.

[9] Yan, Y. (2001). Guide to the flow measurement of particulate solids in pipelines, *International Journal of Storing, Handling and Processing Powder*, vol. 13, no. 4, p. 343-352.

[10] Blondeau, J., Kock, R., Mertens, J., Eley, A.J., Holub, L. (2016). Online monitoring of coal particle size and flow distribution in coal-fired power plants: Dynamic effects of a varying mill classifier speed. *Applied Thermal Engineering*, vol. 98, p. 449-454, **DOI:10.1016/j.applthermaleng.2015.12.113**.

[11] Zhe, K., Xiao-lei, W., Shu-jiang, Z. (2013). Study on the spatial filtering and sensitivity characteristic of inserted electrostatic sensors for the measurement of gas-solid two-phase flow parameters. *Flow Measurement and Instrumentation*, vol. 30, np. 26-33, **DOI:10.1016/j.flowmeasinst.2012.10.001**.

[12] Shao, J., Krabicka, J., Yan, Y. (2010). Velocity Measurement of pneumatically conveyed particles using intrusive electrostatic sensors. *IEEE Transactions on Instrumentation and Measurement*, vol. 59, no. 5, p. 1477-1484, **DOI:10.1109/TIM.2010.2040960**.

[13] Potočnik, P., Strmčnik, E., Govekar, E. (2015). Linear and neural network-based models for short-term heat load forecasting. *Strojniški vestnik – Journal of Mechanical Engineering*, vol. 61, no. 9, p. 543-550, **DOI:10.5545/sv-jme.2015.2548**.

[14] Jurjevčič, B. (2017). The nonlinear analysis of time series from intrusive-electrostatic sensors for gas-solid-flow characterization, yearbook, Department of Energy Engineering, Faculty of Mechanical Engineering, Ljubljana.

[15] Zhao, Y., Wang, S., Xiao, F. (2013). A statistical fault detection and diagnosis method for centrifugal chillers based on exponentially-weighted moving average control charts and support vector regression. *Applied Thermal Engineering*, vol. 51, no. 1-2, p. 560-572, **DOI:10.1016/j.applthermaleng.2012.09.030**.

[16] Kandananond, K. (2014). Guidelines for applying statistical quality control method to monitor autocorrelated processes. *Procedia Engineering*, vol. 69, p. 1449-1458, **DOI:10.1016/j.proeng.2014.03.141**.

[17] Graham, D.P., Salway, G. (2015). *Electricity Supply Industry - IED Compliance Protocol for Utility Boilers and Gas Turbines*, E.ON Technologies, Ratcliffe.

[18] Kisić, E., Petrović, V., Jakovljević, M., Đurović, Ž. (2013). Fault detection in electric power systems based on control charts. *Serbian Journal of Electrical Engineering,* vol. 10, no. 1, p. 73-90, **DOI:10.2298/SJEE1301073K**.

[19] Graham, D. (2010). European Power Industry Experience of EN14181, *VGB powertech*, vol. 90, no. 1-2, pp. 83–94.

[20] Deeskow, P., Steinmetz, U., Hay, M. (2008). Datamining und statistische Prozesskontrolle zur zustandsorientierten Instandhaltung. *VGB powertech*, vol. 88, no. 10, p. 84-87.

[21] Apley, D.W., Cheol Lee, H. (2003). Design of exponentially weighted moving average control charts for autocorrelated processes with model uncertainty. *Technometrics*, vol. 45, no. 3, p. 187-198, **DOI:10.1198/004017003000000014**.

[22] Lazariv, T., Okhrin, Y., Schmid, W. (2015). Behavior of EWMA type control charts for small smoothing parameters. *Computational Statistics & Data Analysis*, vol. 89, p. 115-125, **DOI:10.1016/j.csda.2015.03.010**.

[23] Lucas, J.M., Saccucci, M.S. (1990). Exponentially Moving weighted schemes: control average and enhancements properties. *Technometrics*, vol. 32, no. 1, p. 1-12, **DOI:10.1080/00401706.1990.10484583**.

[24] Montgomery, D. (2009). *Introduction to Statistical Quality Control*, 6th ed. John Wiley and Sons Ltd., Chichester.

[25] Runger, G.C., Willemain, T.R. (1996). Batch-means control charts for autocorrelated data. *IIE Transactions*, vol. 28, no. 6, p. 483-487, **DOI:10.1080/07408179608966295**.

[26] Alwan, L.C., Radson, D. (1992). Time-series investigation of subsample mean charts. *IIE Transactions*, vol. 24, no. 5, p. 66-80, **DOI:10.1080/07408179208964246**.

[27] Russo, S.L., Camargo, M.E., Fabris, J.P. (2012). Applications of Control Charts Arima for Autocorrelated Data. *Practical Concepts of Quality Control*, Nezhad, M.S.F. (ed.), *InTech*, p. 31-53, **DOI:10.5772/50990**.

[28] Ho, S.L., Xie, M. (1998). The use of ARIMA models for reliability forecasting and analysis. *Computers & Industrial Engineering*, vol. 35, no. 1-2, p. 213-216, **DOI:10.1016/S0360-8352(98)00066-7**.

[29] Box, G.E.P., Jenkins, G., Reinsel, G.C. (2008). *Time Series Analysis: Forecasting and Control*, 4th ed., Wiley, Hoboken, **DOI:10.1002/9781118619193**.

[30] Zhang, J. (2012). Air-solids flow measurement using electrostatic techniques, *Electrostatics*, Canbolat, H. (ed.), InTech, Rijeka, p. 61-80, **DOI:10.5772/35937**.

[31] Brockwell, P.J., Davis, R.A. (2002). *Introduction to Time Series and Forecasting*, 2nd ed., Springer, New York, **DOI:10.1007/b97391**.

[32] Burnham, K.P., Anderson, D.R. (2013). *Model Selection and Multimodel Inference: A Practical Information-Theoretic Approach*, 2nd ed., Springer, New York, **DOI:10.1007/b97636**.

Strojniški vestnik - Journal of Mechanical Engineering 63(2017)4, 275-283
© 2017 Journal of Mechanical Engineering. All rights reserved.
DOI:10.5545/sv-jme.2016.4012 Original Scientific Paper
Received for review: 2016-08-30
Received revised form: 2016-12-02
Accepted for publication: 2016-12-16

Failure Analysis of the Multi-Level Series Rotary Seal Device under High-Pressure Water

Zenghui Liu[1,2] – Changlong Du[1,*] – Songyong Liu[1] – Hongxiang Jiang[1]
[1] China University of Mining & Technology, School of Mechatronic Engineering, China
[2] Monash University, Department of Civil Engineering, Australia

High-pressure water jets are used to assist roadheaders in breaking hard rock. The failure life of the high-pressure rotary seal (HPRS) is significant, due to how it affects the safety and efficiency of the roadheader. Here we investigate the mechanical behaviour of the HPRS with a series of experiments. Single-level rotary seal device based studies were conducted to investigate the effect of seal forms, materials, operating pressure and spindle speed on friction torque and leakage. The best seal form from the three kinds of forms was chosen to test the failure life of the multi-level series rotary seal device and the relationships between the operating pressure, spindle speed, temperature, leakage and failure life were analysed. The failure life of rotary seals from Levels 1 to 4 was observed to be 15, 11, 5, and 4 days respectively. The increase in temperature of Levels 1 and 2 was perceived to be slow at the beginning phase of the test, while it rose sharply until the failure occurred, whereas in the case of Levels 3 and 4 it was instantaneous.

Keywords: failure analysis, rotary seal, mechanical testing, wear, high pressure

Highlights

- *The material and seal forms have significance effect on the friction torque.*
- *The leakage increases with operating pressure and lower spindle speed.*
- *Failure life of seal from Levels 1 to 4 is 15, 11, 5 and 4 days, respectively.*
- *The rate of increase in temperature of Levels 1 and 2 is slow in the beginning followed by a sharp rise.*

0 INTRODUCTION

With the increase in energy demand, the demand for coal remains high throughout the world. Coal accounts for around 70 % of the energy consumed in China, while the total demand for coal is increasing every year. Roadway excavation is the first step in coal mining, and the wear of the cutting mechanism of the roadheader is crucial in this process, which has a considerable impact on the reliability of the equipment. The wide use of water jets in mining, petroleum drilling, machine, civil construction, gas drainage, and cleaning operations has suggested that the cutting force and the wear of cutter, as well as the dust produced in the cutting process, can be reduced with the assistance of water jets [1]. As shown in Fig. 1, since the motors drive the cutting head and shaft through the transmission while the rotary seal device remains fixed to the gearbox, the seal between the water jet and the drive shaft is a rotary seal during the cutting process. In order to break rock effectively, the water jet is usually at high pressure [2], which increases the difficulty of the rotary seal. Therefore, the sealing performance and failure life of the high-pressure rotary seal (HPRS) have a significant influence on the rock breaking process of the roadheader.

There has been significant research by many researcher and engineers on rotary seals and high-pressure seals. For example, to obtain an effective tool for predicting the leakage and the dynamic response of honeycomb seals, Saba et al. [3] reviewed the bulk flow model and explored its sensitivity to different hypotheses. Plath et al. [4] conducted an experimental study of rotary shaft lip-type seals and surveyed the torque variation with rotary speed and temperature. Stolarski and Tucker [5] obtained the variations in squeeze force and operating pressure across O-rings, followed by an analysis of the relationship between frictional force and gauge pressure in various types of O-ring seals at the commencement of the linear motion of the shaft.

Bistrazy et al. [6] conducted endurance and friction characteristic tests on U-ring seals and reported the critical operating seal parameters under different design and working conditions by measuring the friction force and leakage endurance curves. They also analysed the effect of increased operating pressures on the friction force increment under reciprocating motion. Kim and Shim [7] used the Mooney-Rivlin model to study the contact force and thermal behaviour of radial lip seals as a function of the contact interface. Wang and Liu [8] explored the creep behaviour and sealing performance of the inner casing of a supercritical steam turbine. The stiffness and damping coefficients of the oil seals were evaluated by Baheti and Kirk [9] using the perturbation

*Corr. Author's Address: China University of Mining & Technology, Xuzhou, China, duclhxj @cumt.edu.cn.

technique; eigenvalue analysis was performed to study the dynamic stability of the compressor rotor. While establishing the numerical model of the O-ring used in the compensatory configuration of the mechanical seal, Li et al. [10] also obtained the Von-Mises stress and contact stress of the O-ring. These researchers performed experiments on a high-frequency failure machine and a water-lubricated O-ring tester to obtain the results of friction force.

Liao et al. [11] investigated the elasto-hydrodynamic lubrication characteristics of the O-ring seal using friction and wear testers, both numerically and experimentally. In their study, the efficiency of the fluid-solid interaction derived from experimental results reinforced their numerical fluid-solid interaction model constructed by analysing the fluid lubrication, contact mechanics, asperity contact and elastic deformation. Yang and Salant [12] and [13] demonstrated the usefulness of simulation in the selection of reciprocating seals. The numerical predictions in the study disclosed that the performance of the O-ring is inferior to that of a U-cup seal. Wiznera et al. [14] performed investigations based on 2D measurements of five equally-distributed areas of the ring to prove the effectiveness of the seal. Yamabe et al. [15] performed pressure cycle tests at hydrogen pressures ranging from 10 MPa to 70 MPa and ambient temperatures ranging from 30 °C to 100 °C to analyse the fracture behaviour of O-rings. The effects of O-ring seals on the effective area of the oil-operated pressure balance were investigated by Woo et al. [16] using two-piston cylinder assemblies in the pressure range of 100 MPa to 300 MPa. Nishimura [17] conducted high-pressure (up to 70 MPa) hydrogen pressurisation-decompression cycle tests on O-rings to investigate the fracture behaviour of O-rings.

The above studies have applied various experiments and simulations, resulting in fruitful achievements as references for the present work. In the previous studies discussed above, information about friction torque and force with rotary speed, temperature and operating pressure, and the elasto-hydrodynamic lubrication in various types of seals were the focus., the failure life test of the rotary seal under high pressure, especially the multi-level series rotary seal has received little attention to date.

Therefore, the experimental analysis of HPRS mechanical behaviour is investigated in this paper, which reports the results of experiments on single-level rotary seal devices to investigate the effect of seal forms, materials, operating pressure and spindle speed on friction torque and leakage. The best seal form was determined and chosen to further test the failure life of the multi-level series rotary seal device, and the relationships between the operating pressure, spindle speed, temperature, leakage and failure life were analysed.

1 EXPERIMENTAL

To test the failure life of the rotary seal, an experimental set-up for HPRS was designed, and experiments were conducted. Fig. 2 shows a detailed description of the experimental set-up. As the power producer, the motor is controlled by the PLC program [18]. To ensure a high axiality, the bearing seat has a cylindrical surface that matches well the shell of the rotary seal device and is bolted with the shell by six bolts. The torque/speed transducer is installed between the motor and the bearing seat, and two couplings are used to combine the above three facilities. The water in the reservoir is pumped and transformed to high-pressure water, and then the pressurized water is

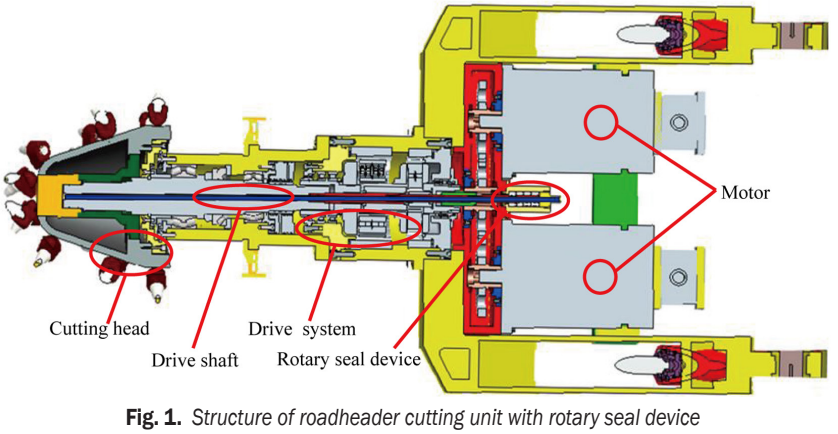

Fig. 1. *Structure of roadheader cutting unit with rotary seal device*

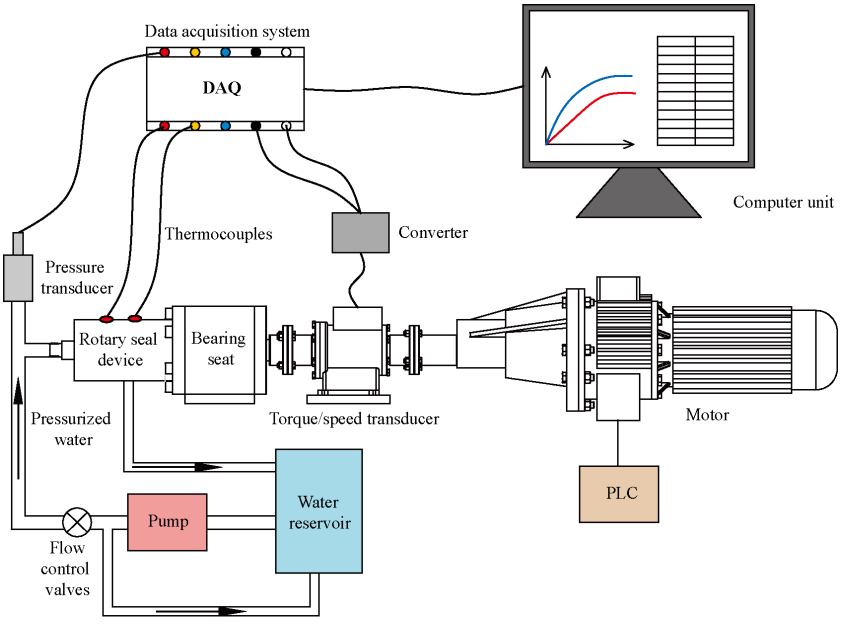

Fig. 2. *Schematic of HPRS set-up*

streamed through the flow control valves to the inlet of the rotary seal device and the pressure transducer, and the superfluous pressurized water is directed back to the reservoir.

A USB data acquisition system (DAQ), consisting of numerous transducers, a DAQ card, and a computer unit, is used to monitor a range of parameters during the experimental process. The DAQ card includes sixteen independent channels and monitors. In the experiments, the excitation voltage measurement range is from -10 V to 10 V and the data sampling rate is adjustable up to 250,000 Hz. The pressure transducer JNBP-30 processes the water pressure signal to the voltage signal and sends it to the DAQ card directly. The thermocouple placed in the rotary seal device monitors the temperature of the seal rings and sends it to the DAQ card. Because the output signals of the torque/speed transducer are pulse signals, a converter is connected to the torque/speed transducer to convert the pulse signals to the voltage signals and send them to the DAQ card. Then, the analysable digital data is sent to the computer unit and displayed there.

The rotary seal device is the key unit of the whole set-up. According to the installation position and the size of rotary seal device shown in Fig. 1, the multiple-level rotary seal is designed to be of four levels, as shown in Fig. 3.

Based on the relative motion between the seal and the mechanical parts, there are two kinds of seal: static and dynamic. The high-pressure water flows from the inlet in the joint, then through the flow channels in the joint and the shaft, and finally to the outlet in the shell. The joint is bolted to–the shell, and since there is no relative motion among the joint, shell and seal chambers, the common O-rings were adopted as the static seal. While the shaft rotates and the seal chambers are static, the dynamic seal is implemented from the rotary seal rings. With the function of the static seal ring and the rotary seal ring, the high-pressure water flows to the outlet successfully. Because the dynamic seal can be broken more easily than the static seal, and the higher the water pressure, the worse the sealing effect may be, our work mainly focused on the mechanical behaviour and failure life of the HPRS [19]. The diameter of the shaft is 25 mm, and for monitoring the temperatures of the rotary seal rings, thermocouples are placed in holes 2 mm from the rotary seal rings and shaft. During the experimental process, all the leakage holes were open at first, and once the leakage rate of the first leakage hole rose to the prescribed value, the first leakage hole was plugged by the screw plug, allowing the high-pressure water to flow to the second-level rotary seal ring, and the leakage ran out from the second leakage hole. By analogy, the failure of the whole rotary seal unit followed when the leakage of the fourth leakage hole rose to the prescribed value.

During the experimental process, the motor was started first, and the speed was adjusted to the

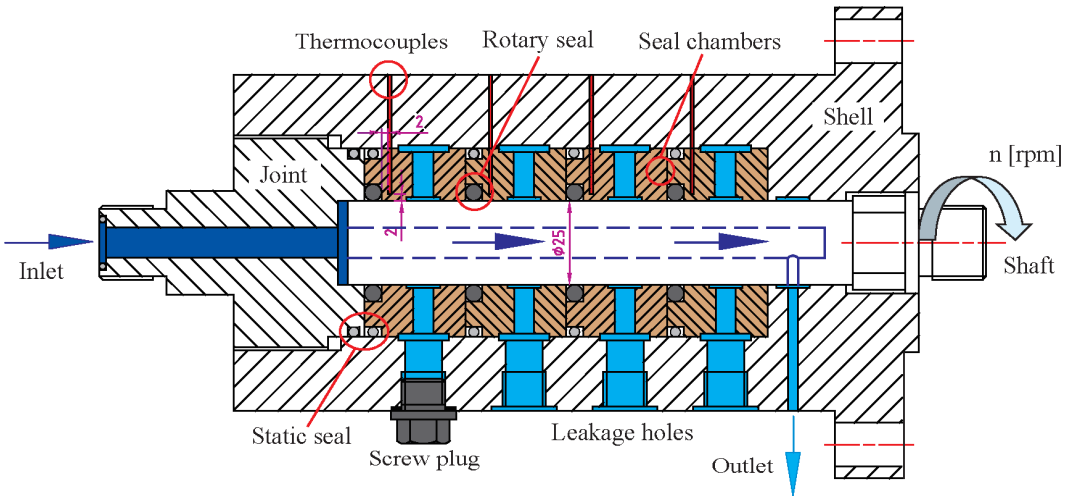

Fig. 3. *Schematic of the HPRS device*

required value. After the motor running smoothly, the pump was started, and the pressure is adjusted to reach the required value. Then the experimental data were collected and stored in the computer. After the completion of a group of tests, the speed of the motor and the pressure of water were adjusted slowly, and when the motor and pump were once again running smoothly, a new group of tests was started. When the tests were finished, the pressure of pump decreases firstly, afterwards the pump and the motor were turned off.

2 RESULTS

2.1 Analysis of the Single-Level Rotary Seal Device

In order to test the failure life of the multi-level series rotary seal device efficiently, the mechanical behaviour of the single-level rotary seal was analysed first, so that the best rotary seal form could be chosen for the failure life test. During the process of the single-level rotary seal test, the seal chambers of Levels 2, 3 and 4 were installed with the shell without rotary seals to test the effect of a series of parameters on the HPRS performance.

For the HPRS, the most common forms are the O-ring seal and the tooth slip ring combined seal. Fig. 4 represents the cross-section geometries of the three seals. Fig. 4a shows the common nitrile butadiene rubber (NBR) O-ring seal, Fig. 4b is the common NBR O-ring coated with polytetrafluoroethylene (PTFE), and Fig. 4c is the combined seal, which consists of a NBR O-ring and a PTFE tooth slip ring. In this study, the internal diameter of the three seals was 25 mm, and the cross-section diameter of the three O-rings was 3.53 mm. To study the effect of seal form and material on friction torque, the speed of the motor was set at 50 rpm, which is the speed of the roadheader under actual working conditions, and the pressure of the pump was adjusted to 40 MPa, which is the highest demand based on the design.

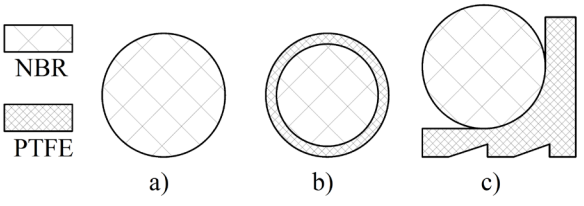

Fig. 4. *Cross-section geometries of the three seals: a) common O-ring seal; b) coated O-ring seal; c) combined seal*

Fig. 5 shows the friction torque curves of different seals under the same conditions. According to the calculations, the mean friction torque of the three seals was 6.31 N·m, 5.68 N·m and 5.02 N·m, respectively. It should be noted that the curves changed periodically, and each cycle length matches well the speed of the shaft, which indicates that the contact pressure of the seals changed with the rotation of the shaft because of the tiny deviation of the coaxial and the uneven deformation of the seals during the squeezing process. Compared with the coated O-ring seal, the amplitude of the common NBR O-ring seal was larger, due to the different material properties of the NBR and the PTFE. The Young's modulus of the NBR was smaller, which resulted in the larger uneven deformation. However, the friction coefficient of the NBR was larger, and the amplitude and the mean

value of the common NBR O-ring seal were larger. This established that the material has a significant effect on friction torque. A comparison of Figs. 4b and 4c indicates that the seal form has a small effect on the changing trend of the friction torque, but has a great effect on the mean value of the friction torque. The mean value of the combined seal was smaller than the coated O-ring seal, which demonstrates that the mechanical behaviour of the combined seal works better.

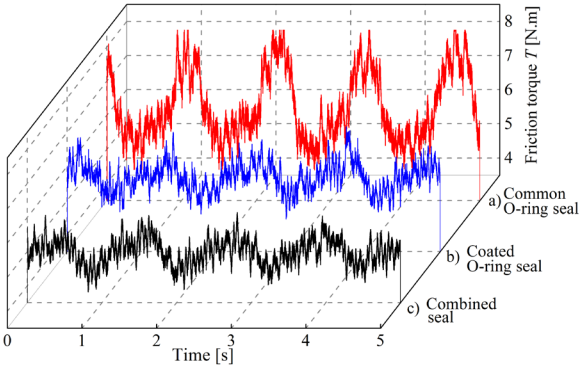

Fig. 5. *Friction torque curves of different seals*

Depending on the actual working conditions of the roadheader, if the water flows all around the tunnelling working surface will cause great trouble, so it is important to control the leakage rate of the rotary seal. In addition, leakage affects the rock breaking efficiency by reducing the pressure of the water jet. Therefore, the maximum leakage allowed was defined as 50 mL/h, based on the design of the rotary seal device.

Fig. 6 shows the curves of leakage under different operating pressures, where the solid lines are the three seal types in a static condition, and the dash lines are the three seal types at 50 rpm spindle speed. The leakages of both common O-ring seals and coated O-ring seals increased the operating pressure, while the leakages of the combined seals decreased with the operating pressure. This can be attributed to the different deformations of seals under different operating pressures. As the O-ring in the combined seal had the smaller deformation compared with the O-ring seal, the leakages of combined seals were higher than those of the O-ring seals under 0.5 MPa operating pressure. For the combined seal, the higher the ΔP, the greater the deformation of the O-ring. This could cause the higher contact pressure between the tooth slip ring and the shaft, resulting in smaller leakage. However, for the O-ring seal, the higher ΔP may cause greater deformation of the O-ring, but the O-ring could be twisted easily and even overturned when the deformation was great enough, and then the leakage then increased with ΔP. For the common O-ring seal, both the static leakage and dynamic leakage under 40 MPa operating pressure were beyond the allowed maximum leakage of 50 ml/h. Therefore, the common O-ring seal is not suitable for a rotary seal device under high pressure.

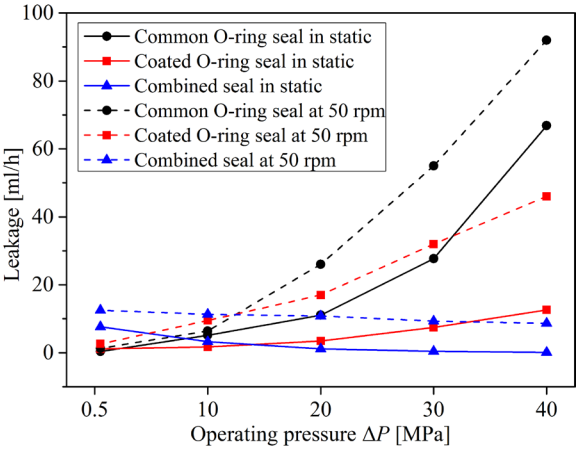

Fig. 6. *Effect of operating pressures on leakage*

Fig. 7 represents the variations of leakages of the three seal types with different spindle speeds under 40 MPa operating pressure. It shows that the variation trends of the curves are not obvious. The leakages increase speed at lower spindle speed, and then remain almost unchanged with any further increase in speed. The reason is that the faster speed causes the water to be pushed into the contact zone easily, resulting in the easy formation of the lubrication film.

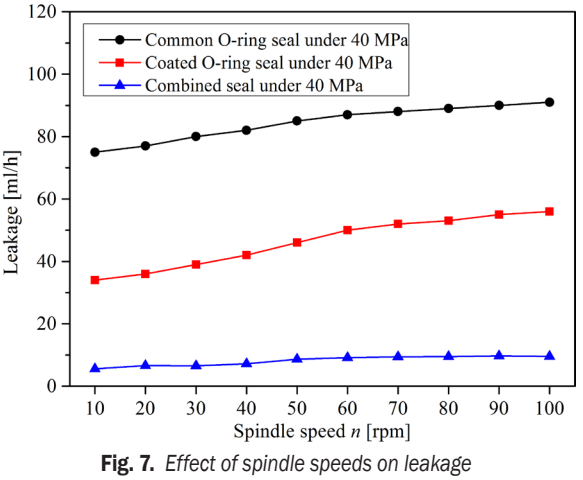

Fig. 7. *Effect of spindle speeds on leakage*

When the spindle speed reached 70 rpm, the lubrication film formed was quite effective, not only

reducing the wear but also the leakage, as the leakage changed slightly with the higher spindle speed. Moreover, the leakage of the common O-ring seal and coated O-ring seal changed within 75 ml/h to 90 ml/h and 35 ml/h to 60 ml/h, respectively, while the leakage of the combined seal was around 10 ml/h. The leakage of the combined seal was the smallest among the three seal types.

2.2 Analysis of the Combined Seal in Multi-Level Series Rotary Seal Device

From above analysis, it is evident that the sealing effect of the combined seal is best, because of its smaller friction torque, greater contact pressure and smaller leakage. As a result, the combined seal was chosen to conduct the failure life test of the multi-level series rotary seal device. The rotary seal test-bed and a schematic of the rotary seal device are shown in Figs. 2 and 3, and the inner structure of the multi-level series rotary seal device is shown in Fig. 8. The rotary seal device has four levels, the rotary seals were the combined seals, the static seals were the common O-ring seals, the seal chambers were made of brass, and the shaft was made of stainless steel.

According to Lingerkar [18], the operating pressure and the shaft sliding velocity have a great influence on the performance of the rotary seal. Figs. 9 and 10 show the temperatures and leakages of rotary seal level 1 at 50 rpm spindle speed under operating pressures of 10 MPa, 20 MPa, 30 MPa and 40 MPa. The temperatures were measured by placing thermocouples 2 mm from the rotary seal rings and shaft, as shown in Fig. 3.

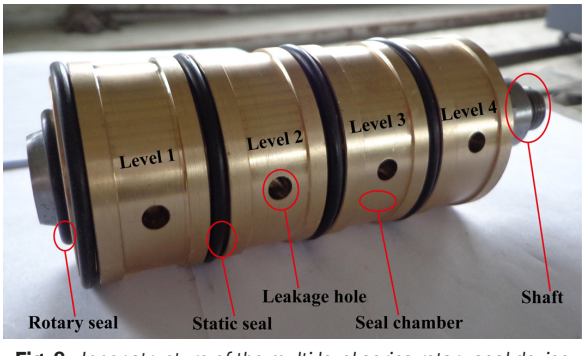

Fig. 8. *Inner structure of the multi-level series rotary seal device*

Fig. 9 shows that the trends of temperatures under different operating pressures are similar; the temperature increases quickly for the first several hours, and then the rate of increase slows. However, the temperature in all cases remains high under higher operating pressure. For example, after 10 hours of testing, the temperatures under 10 MPa, 20 MPa, 30 MPa and 40 MPa were 31 ºC, 34 ºC, 38 ºC and 43 ºC, respectively. The reason may be that the higher the ΔP, the greater the contact pressure between the tooth slip ring and the shaft, which in turn results in higher temperatures.

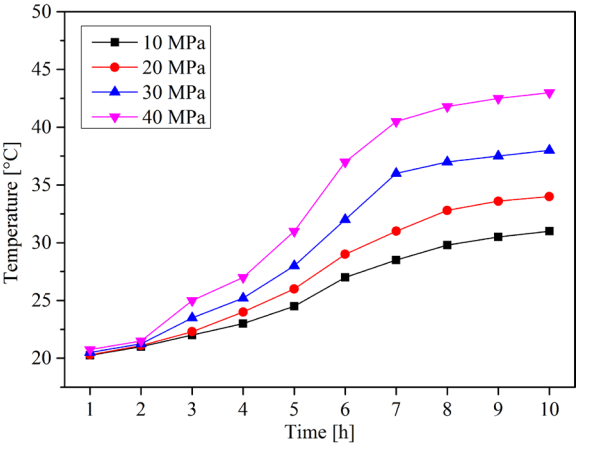

Fig. 9. *Temperatures of seals under different operating pressures*

Fig. 10 shows that the leakages under each operating pressure remained at steady states within the 10 hours, because the seals were well lubricated and worked well during that period. Meanwhile, the leakages in all cases persisted less for relatively higher operating pressure. The reason may be that the higher the ΔP, the greater the contact pressure between the tooth slip ring and the shaft, causing less leakage, as shown in Fig. 6.

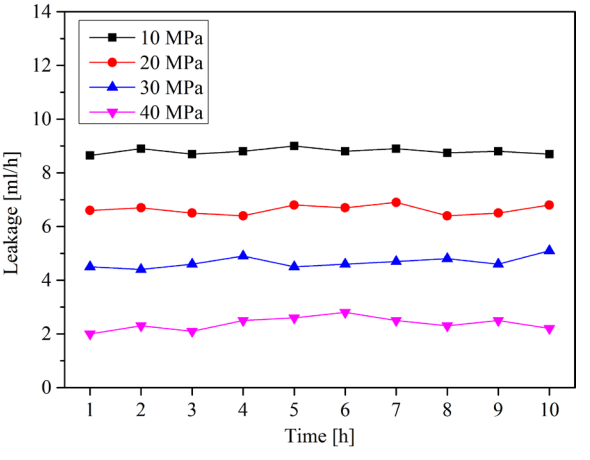

Fig. 10. *Leakages of seals under different operating pressures*

Fig. 11 presents a series of experimental temperature curves at different spindle speeds under

the operating pressure of 40 MPa. It was observed that the temperature rises sharply at the beginning of the test, and then increases slowly, and some temperature curves at lower spindle speeds gradually tend to reach a steady state with sliding time. Moreover, the temperature in all cases remains higher under relatively higher spindle speeds. For example, after 10 hours of testing, the temperature at 50 rpm was 43 ºC, and the temperature increased to 82 ºC when the spindle speed was 100 rpm. The reason is that the faster the speed, the more frictional heat at the contact zone is generated, and the higher the temperature remains.

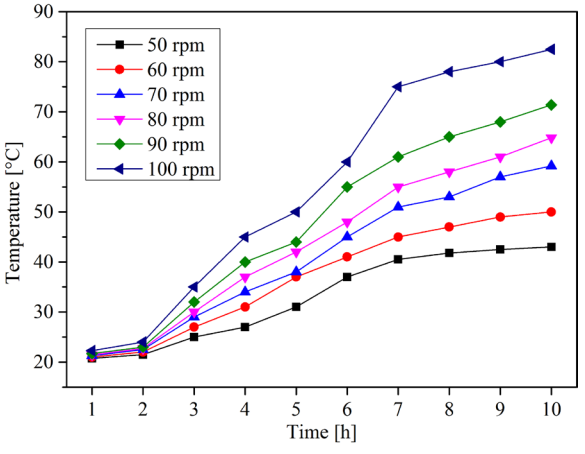

Fig. 11. *Temperatures of seals at different spindle speeds*

Fig. 12 shows that the leakages at each spindle speed remained at a steady state within the 10 hours, because the seals were well lubricated and working well. Meanwhile, the leakages remained less at relatively lower speeds, but there was little difference in the leakages for the speeds of 70 rpm to 100 rpm. The reason is shown in Fig. 6.

Based on the actual working conditions of roadheaders, excavation and support are alternative modes of operation, and as the roadheader is in a shutdown state during the support process, the whole working time of the roadheader is approximately 10 hours a day. Moreover, since comprehensive inspections, maintenance and repairs of roadheaders are commonly conducted once a month, the expected life of a multi-level series rotary seal device is at least 30 days. The rated speed of the roadheader is around 50 rpm, but the speed is sometimes set at 100 rpm to break hard rock. Therefore, the spindle speed of the motor was set at 100 rpm during this test, and the motor ran from 8 am to 6 pm every day to make a total of 10 hours a day. The temperature was measured three times at 6 pm every day, and the average values were recorded, and these are shown in Fig. 13. Meanwhile, the leakages were collected from 5 pm to 6 pm every day, and the values are presented in Fig. 14.

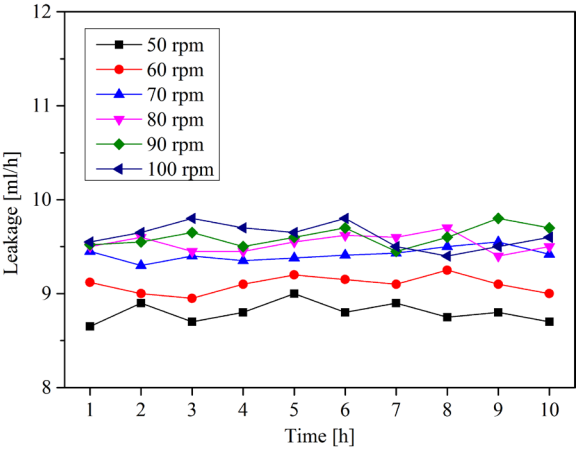

Fig. 12. *Leakages of seals at different spindle speeds*

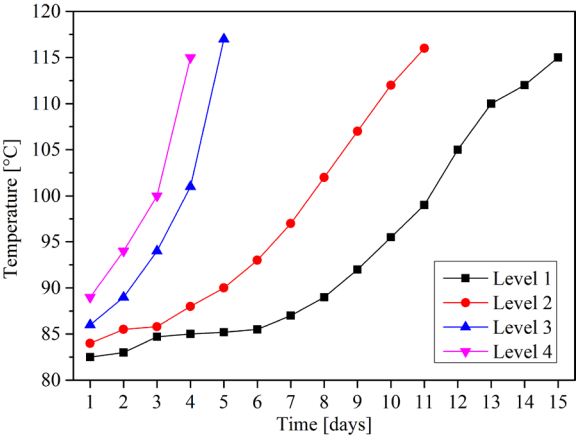

Fig. 13. *Failure life and temperature of each level rotary seal*

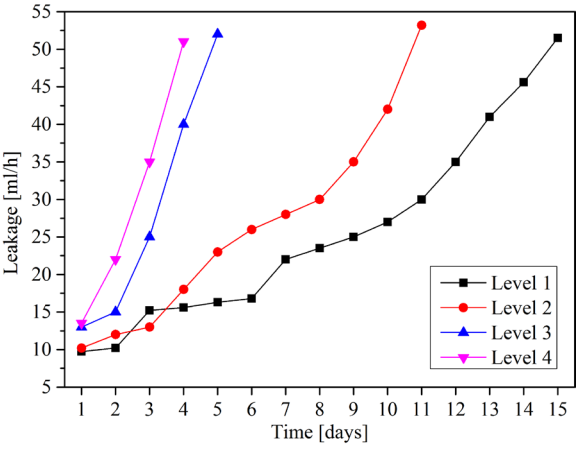

Fig. 14. *Failure life and leakage of each level rotary seal*

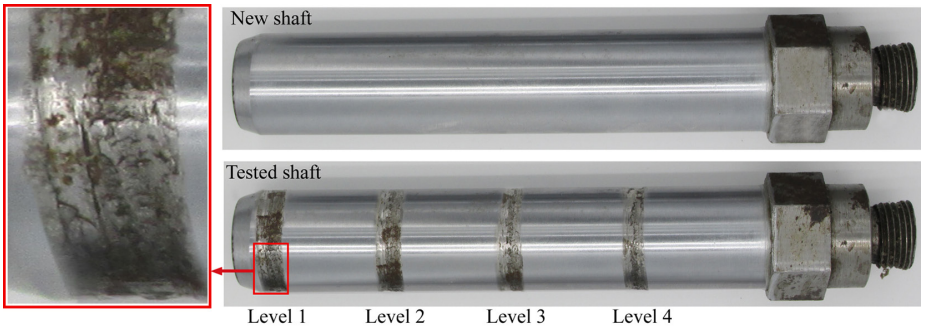

Fig. 15. *Comparison of the shaft before and after failure*

As shown in Figs. 13 and 14, the failure life of the rotary seal from Level 1 to Level 4 was 15 days, 11 days, 5 days and 4 days, respectively. The temperatures of all levels rise with time, but the temperature of Levels 1 and 2 increase slowly in the beginning phase of the test and then go up sharply until their failure, while the temperature of Levels 3 and 4 rise instantaneously. The trends of the leakage curves are similar to the temperature curves. For Level 1, the seal performance at the interface between the tooth slip ring and the shaft was quite good for the first two days of the test, and then the rotary seal advanced to a stable period during the 3rd to 6th day, which was the best period. The tooth slip ring is usually made of PTFE, and some is generated because of the continuous friction and wear at the interface. Some PTFE dross may be discharged with the leakage, while other such dross may remain at the interface, which will in turn increase the frictional coefficient and frictional heat, and even damage the shaft, generating some metal dross. It is a vicious cycle that the accumulative high frictional heat damages the tooth slip ring and the shaft, while the dross from the damaged tooth slip ring and shaft increase the frictional heat at the interface. Therefore, both the temperature and leakage increased gradually from the 7th day to 15th day when the leakage was beyond 50 ml/h.

According to Fig. 3, once the leakage hole of Level 1 was plugged by the screw plug, the high-pressure water could flow to the rotary seal ring of Level 2, and some dross could flow to the interface of the Level 2 directly. Therefore, the curves of Level 2 have no stable period compared with Level 1, and the failure life is shorter than that of Level 1. Fig. 14 shows the comparison of the shaft before and after failure. It was observed that the damage at the interface of Level 1 was the most serious, while the damage of level 4 was the slightest. The reason is that the friction at the interface of Level 1 will continue constantly because of the poor thermal conductivity property and the great thermal expansion coefficient of PTFE. Therefore, more PTFE and metal dross from Levels 1 and 2 may flow to the interface of Levels 3 and 4, and then the temperature and leakage increase sharply as shown in Figs. 14 and 15, which cause the fast failure of the rotary seal.

The whole failure life of the multi-level series rotary seal device was found to be 35 days, well beyond the expected life. Most of the time, the speed of the shaft was around 50 rpm, not 100 rpm during the working process. As a result, the actual failure life of the four-level rotary seal device under working conditions would be longer than 35 days, and the extra life can be regarded as safety assurance. However, for the multi-level series rotary seal device, the series is not the best, because the failure life of the later level was too short in comparison with the earlier level. The suggested series for rotary seal devices similar to that described in this paper is three or four levels.

3 CONCLUSIONS

In this study, we have successfully employed experimental analyses to investigate the seal performance and failure analysis of the multi-level series rotary seal device. The following conclusions can be drawn.

Experimental analyses of the single-level series rotary seal device indicate that the mechanical behaviour of the combined seal is better than that of the O-ring seal. The leakages of O-ring seals increase with the operating pressure, while the leakages of combined seals decrease with the operating pressure. In addition, the leakage increases with speed at lower spindle speed, and then reaches a value after which it remains almost unchanged with any further increase in speed.

The combined seal was chosen to conduct failure life test of the multi-level series rotary seal device, and it was found that the failure life of rotary seals from Level 1 to Level 4 is 15 days, 11 days, 5 days and 4 days, respectively. The temperatures of all the levels rise with time, but the temperatures of Levels 1 and 2 increase slowly at the beginning of the test and then rise sharply until their failure, while the temperature of Level 3 and Level 4 rise instantaneously. Furthermore, the trends of the leakage curves are similar to those of the temperature curves.

4 ACKNOWLEDGEMENTS

This paper is jointly supported by the Priority Academic Program Development of Jiangsu High Education Institute of China, the National Natural Science Foundation of China (No. 51375478) and the China Postdoctoral Science Foundation funded project (No. 2015M581880).

5 REFERENCES

[1] Liu, X., Liu, S., Li, L., Cui, X. (2015). Experiment on conical pick cutting rock material assisted with front and rear water jet. *Advances in Materials Science and Engineering*, Article ID 506579, **DOI:10.1155/2015/506579**.

[2] Jiang, H., Du, C., Zheng, K., Liu, S. (2015). Experimental research on the rock fragmentation load of water jet-assisted cutting head. *Tehnički vjesnik – Technical Gazzete*, vol. 22, no. 5, p. 1277-1285, **DOI:10.17559/TV-20141020152601**.

[3] Saba, D., Forte, P., Vannini, G. (2014). Review and upgrade of a bulk flow model for the analysis of honeycomb gas seals based on new high-pressure experimental data. *Strojniški Vestnik - Journal of Mechanical Engineering*, vol. 60, no. 5, p. 321-330, **DOI:10.5545/sv-jme.2014.1835**.

[4] Plath, S., Mayer, S., Wollesen, V. M. (2016). Friction torque of a rotary shaft lip type seal-a comparison between test results and finite element simulation. *Mechanics*, vol. 54, no. 4, p. 55-59.

[5] Stolarski, T.A., Tucker, M. (1996). Frictional performance of an O-ring type seal at the commencement of linear motion. Tribology Letters, vol. 2, no. 4, p. 405-416, **DOI:10.1007/BF00156912**.

[6] Bisztray-Balku, S. (1999). Tribology of elastomeric and composite reciprocating hydraulic seals. Periodica Polytechnica. Engineering. *Mechanical Engineering*, vol. 43, no. 1, p. 63-80.

[7] Kim, C.K., Shim, W.J. (1997). Analysis of contact force and thermal behaviour of lip seals. Tribology International, vol. 30, no. 2, p. 113-119, **DOI:10.1016/0301-679X(96)00030-8**.

[8] Wang, W., Liu, Y. (2015). Analysis of the sealing performance and creep behavior of the inner casing of a 1000 MW supercritical steam turbine under bolt relaxation. *Engineering Failure Analysis*, vol. 57, p. 363-376, **DOI:10.1016/j.engfailanal.2015.08.012**.

[9] Baheti, S.K., Kirk, R.G. (1999). Analysis of high pressure liquid seal ring distortion and stability using finite element methods. *Journal of Tribology*, vol. 121, no. 4, p. 921-926, **DOI:10.1115/1.2834156**.

[10] Li, S.X., Cai, J.N., Zhang, Q.X., Jie, L., Gao, J.J. (2010). Performance Analysis of O-ring Used in Compensatory Configuration of Mechanical Seal. *Tribology*, vol. 30, no. 3, p. 308-314. (in Chinese)

[11] Liao, C., Huang, W., Wang, Y., Suo, S., Liu, Y. (2013). Fluid-solid interaction model for hydraulic reciprocating O-ring seals. *Chinese Journal of Mechanical Engineering*, vol. 26, no. 1, p. 85-94, **DOI:10.3901/CJME.2013.01.085**.

[12] Yang, B., Salant, R.F. (2008). Numerical model of a tandem reciprocating hydraulic rod seal. *Journal of Tribology*, vol. 130, no. 3, p. 032201, **DOI:10.1115/1.2908924**.

[13] Yang, B., Salant, R.F. (2011). Elastohydrodynamic lubrication simulation of O-ring and U-cup hydraulic seals. *Proceedings of the Institution of Mechanical Engineers, Part J: Journal of Engineering Tribology*, vol. 225, no. 7, p. 603-610, **DOI:10.1177/1350650110397236**.

[14] Wizner, M., Jakubiec, W., Starczak, M. (2011). Description of surface topography of sealing rings. *Wear*, vol. 271, no. 3-4, p. 571-575, **DOI:10.1016/j.wear.2010.04.036**.

[15] Yamabe, J., Koga, A., Nishimura, S. (2013). Failure behavior of rubber O-ring under cyclic exposure to high-pressure hydrogen gas. *Engineering Failure Analysis*, vol. 35, p. 193-205, **DOI:10.1016/j.engfailanal.2013.01.034**.

[16] Woo, S.Y, Lee, Y.J, Choi, I.M, Kim, B.S, Shin, H.H. (2002). Effects of the O-ring used for sealing in high-pressure balances on measurements of pressure. *Measurement Science and Technology*, vol. 13, no. 8, p. 1353-1358, **DOI:10.1088/0957-0233/13/8/325**.

[17] Nishimura, S. (2014). Fracture behaviour of ethylene propylene rubber for hydrogen gas sealing under high pressure hydrogen. *International Polymer Science and Technology*, vol. 41, no. 6, p. 360-366.

[18] Lingerkar, K., Khonsari, M.M. (2010). On the effects of sliding velocity and operating pressure differential in rotary O-ring seals. *Proceedings of the Institution of Mechanical Engineers, Part J: Journal of Engineering Tribology*, vol. 224, no. 7, p. 649-657, **DOI:10.1243/13506501JET755**.

[19] Handrasekaran, C. (2009). *Rubber Seals for Fluid and Hydraulic Systems*. William Andrew, Norwich.

Vsebina

Strojniški vestnik - Journal of Mechanical Engineering
letnik 63, (2017), številka 4
Ljubljana, april 2017
ISSN 0039-2480

Izhaja mesečno

Razširjeni povzetki (extended abstracts)

Strojniški vestnik - Journal of Mechanical Engineering 63(2017)4, SI 33
© 2017 Strojniški vestnik. Vse pravice pridržane.
Prejeto v recenzijo: 2016-09-28
Prejeto popravljeno: 2017-01-30
Odobreno za objavo: 2017-02-20

Validacija numerične metode na primeru optimizacije pečniškega prostora z uporabo numeričnih izračunov in eksperimentalnih preizkusov

Uroš Kokolj[1,*] – Leopold Škerget[2] – Jure Ravnik[2]

[1] Gorenje, d.d., Razvojno kompetenčni center kuhalni aparati – Velenje, Slovenija
[2] Univerza v Maribor, Fakulteta za strojništvo, Slovenija

Optimizacija izdelkov in tehnologij je in bo v naslednjih letih ena od glavnih aktivnosti proizvajalcev različnih izdelkov. Ker so klasični postopki optimizacije izdelkov z eksperimentalnimi meritvami časovno in stroškovno zelo potratni, prihajajo v ospredje napredna inženirska orodja, kot so numerični izračuni. V obravnavanem primeru se je za potrebe izboljšave funkcionalnih lastnosti pečenja uporabil že predhodno razvit 3D časovno odvisen numerični model, ki omogoča napovedovanje stopnje porjavelosti piškotov.

Izvedla se je validacija numeričnega modela na primeru optimizacije pečenja pečice, kjer je bil cilj izboljšati enakomernost pečenja. Obstoječi numerični model, ki temelji na računalniški dinamiki tekočin, se je nadgradil s temperaturno odvisnimi lastnostmi zraka in piškotov. S pomočjo numeričnih izračunov se je preverilo šest različnih izvedb pokrova ventilatorja.

Numerični izračuni so se izvedli s pomočjo računalniškega programa ANSYS CFX. Za pokrov ventilatorja, ki je na podlagi numeričnih izračunih pokazal najboljše rezultate, se je izvedla preverba s pomočjo eksperimentalnih preizkusov peke piškotov. Eksperimentalni preizkusi so se izvedli na obstoječem in na izboljšanem pokrovu ventilatorja po standardu EN 60350-1.

Pri iskanju najboljše izvedbe pokrova ventilatorja smo upoštevali dva kriterija. Prvi kriterij se navezuje na največjo razliko v stopnji porjavelosti piškotov, ki je predstavljena kot vrednost $R_{y\,max} - R_{y\,min}$. To je tudi kriterij, ki bi ga uporabnik izpostavil kot preveliko razliko v zapečenosti, saj se pojavljajo lokalni minimumi in maksimumi. Drugi kriterij je bila ocena enakomerne porjavelosti po celotnem nivoju, ki je predstavljena s standardnim odklonom polja σ, stopnje porjavelosti R_y. Glede na rezultate numeričnih izračunov in glede na navedena kriterija za ocenjevanje in izbiro najboljšega pokrova ventilatorja smo prišli do zaključka, da najboljše rezultate po obeh kriterijih da pokrov izvedbe b). Poleg najnižje razlike v stopnji porjavelosti 13,46 % ima tudi najmanjši standardni odklon polja porjavelosti 2,99. Po izvedenih numeričnih izračunih različnih pokrovov ventilatorja smo izvedli funkcionalni preizkus pečenja piškotov z izvedbo korigiranega pokrova ventilatorja b). Na podlagi eksperimentalnih rezultatov lahko zaključimo, da poda izboljšana izvedba pokrova ventilatorja b), ki je bila pridobljena s pomočjo numeričnih izračunov, boljše rezultate funkcionalnosti pečniškega prostora kot osnovna oblika pokrova ventilatorja a). Izboljšana izvedba pokrova ventilatorja b) je tako zmanjšala razliko med največjo in najmanjšo stopnjo porjavelosti $R_{y\,max} - R_{y\,min}$ za 25,9 % in izboljšala enakomernost porjavelosti σ za 22,7 %.

Tako numerični kot eksperimentalni rezultati so pokazali, da izboljšan pokrov ventilatorja zagotovi boljše rezultate enakomernosti pečenja. Iz ugotovitev lahko zaključimo, da so numerični izračuni zelo dobro napovedali izboljšavo pokrova ventilatorja, ki smo jo preverili z eksperimentalnimi meritvami, s čimer smo potrdili uporabo numeričnega modela za napovedovanje stopnje porjavelosti za aplikativno uporabo na pečniških prostorih. Uporaba numeričnega modela bo v praksi pomenila velik časovni in finančni prihranek v primerjavi s klasičnimi razvojnimi postopki priprave prototipov in izvajanja različnih eksperimentalnih meritve. Uporaba numeričnega modela za napovedovanje stopnje porjavelosti se bo tako lahko uporabila pri razvoju novih pečniških prostorov in novih generacij izdelkov.

Ključne besede: računalniška dinamika tekočin, pečenje, pečica, prenos toplote, piškoti, optimizacija

*Naslov avtorja za dopisovanje: Gorenje, d.d., Razvojno kompetenčni center kuhalni aparati – Velenje, Partizanska 12, 3320 Velenje, Slovenija, uros.kokolj@gorenje.com

Strojniški vestnik - Journal of Mechanical Engineering 63(2017)4, SI 34
© 2017 Strojniški vestnik. Vse pravice pridržane.
Prejeto v recenzijo: 2016-12-04
Prejeto popravljeno: 2017-02-16
Odobreno za objavo: 2017-03-13

Sistem nastavljivega podajnega prijemala na pnevmatično mišico za montažna opravila

Tudor Deaconescu* – Andrea Deaconescu
Transilvanska univerza v Brasovu, Romunija

Snovanje novega prijemala se začne s pravilno definicijo zahtevanih funkcionalnih lastnosti. Zahteve glede sile, togosti/podajnosti, gibljivosti in števila prostostnih stopenj so odvisne od namena uporabe prijemala. Pri nalogah, ki zahtevajo varno prijemanje, je mogoče občutno zmanjšati tveganje poškodb na prijetem predmetu z dodatnimi zaznavali ali z ustrezno zasnovo krmiljenja. Alternativa dodatnim zaznavalom so izvršni členi z variabilno togostjo (VSA), znani tudi kot nastavljivi podajni izvršni členi (ACA). Uporaba nastavljivih podajnih izvršnih členov zagotavlja prilagajanje prijemala dejanskim okoliščinam pri delu, ki se lahko razlikujejo od projektiranih.

V članku je predstavljena inovativna konstrukcijska rešitev sistema prijemala, ki jo je mogoče pritrditi na industrijskega robota za montažna opravila. Osnova konstrukcije prijemala je linearna pnevmatična mišica kot izvršni člen ter prenos gibanj prek mehanizma z zobato letvijo.

Z uporabo pnevmatične mišice v prijemalu je zagotovljena lahka in fleksibilna konstrukcija za varno rokovanje s predmeti. Podajnost je posebna lastnost pnevmatične mišice, ki omogoča varno prijemanje predmetov brez poškodb. Nastavljiv podajni izvršni člen deluje v območju med dvema skrajnima mejama: togostjo za točno pozicioniranje in podajnostjo, kjer je bolj kot točnost pomembna varnost gibanja. Navdih za razvoj pnevmatičnih mišic prihaja od bioloških sistemov. Prilagodljiva podajnost pnevmatičnih mišic je dosežena z zvezno nastavljivo togostjo.

Predlagano prijemalo je asimetričen sistem z dvema čeljustma in zobniškim mehanizmom za prenos moči. Asimetrija prijemala izhaja iz asimetrične namestitve pnevmatične mišice glede na os simetrije prijetega predmeta ter omogoča vgradnjo proporcionalnega tlačnega regulatorja v telo prijemala.

V članku je predstavljen diagram zgradbe sistema prijemala, konstrukcija in diagram krmiljenja pnevmatike. Podajnost celotnega sistema se spreminja z zveznim prilagajanjem zračnega tlaka.

Eksperimentalni del raziskave je bil osredotočen na vedenje celotnega sestava, določanje sile čeljusti in podajnosti sistema. Velikost sile ni odvisna le od tlaka, temveč tudi od smeri vzpostavljanja tlaka (povečevanje/napihovanje ali zmanjševanje/praznjenje). Rezultati eksperimentov so pokazali močno histerezo sile.

Z meritvami je bila ugotovljena nelinearna odvisnost med silo in odmikom sistema prijemala. Sistem ima torej nastavljivo podajnost in je primeren za montažna opravila.

Eksperimenti so pokazali, da se z odpiranjem čeljusti in naraščanjem tlaka zmanjšuje togost in povečuje podajnost. Odzivni čas sistema na spremembe obremenitev je daljši, manjša pa je tudi točnost. Pri nalogah, kjer togost sistema ni tako pomembna, je glavna zahteva varno rokovanje s prijetim predmetom, zmožnost povečevanja podajnosti s tlakom pa je v vsakem primeru prednost.

Pri montažnih opravilih, kjer sestavni deli niso idealno poravnani, tovrsten podajni sistem omogoča prilagajanje danim okoliščinam ter montažo brez uničenja sestavnih delov.

Sledi zaključek, da so pnevmatične mišice s svojim specifičnim vedenjem zanimiva konstrukcijska izvedenka sodobnega prijemala.

Ključne besede: montaža, podajnost, prijemala, manipulatorji, pnevmatične mišice, togost

*Naslov avtorja za dopisovanje: Transilvanska univerza v Brasovu, 29 Eroilor Bd., Brasov, Romunija, tdeacon@unitbv.ro

Strojniški vestnik - Journal of Mechanical Engineering 63(2017)4, SI 35
© 2017 Strojniški vestnik. Vse pravice pridržane.
Prejeto v recenzijo: 2016-12-12
Prejeto popravljeno: 2017-02-06
Odobreno za objavo: 2017-02-14

Indeks uspešnosti za obtekanje telesa v kanalu z MHD-nanofluidom pri visokih vrednostih Re

Kozhikkatil Sunil Arjun* – Rakesh Kumar
Indijski inštitut za tehnologijo, Oddelek za strojništvo, Indija

Cilj predstavljene študije je preučitev razmerja med velikostjo in položajem valja, jakostjo magnetnega polja, Reynoldsovim številom, volumskim deležem nanodelcev in indeksom uspešnosti za kvazi dvodimenzionalno obtekanje krožnega valja v pravokotnem kanalu, pri čemer ti parametri vplivajo na tokovne lastnosti vrtinčne sledi, odlepljanje ter sile upora in vzgona. Preučen je tudi vpliv magnetnega polja na prisilno konvekcijo ob valju. V enačbi o ohranitvi momenta je prezrt vpliv vzgona in tok je obravnavan kot nestisljiv tok s konstantnimi termodinamičnimi in transportnimi lastnostmi Newtonske tekočine.

Mnoge tehnične aplikacije na tem področju z visokimi hitrostmi in v visoko turbulentnih režimih je zelo težavno modelirati in nujne so numerične simulacije. Večina računskih modelov v literaturi zaradi enostavnosti in sprejemljive točnosti uporablja dve enačbi za popis turbulence. Razpoložljivi podatki o obtekanju krožnega valja v kanalu z MHD-nanofluidom so skopi. Izpuščeni so členi, ki popisujejo vpliv viskozne disipacije in Joulove toplote in privzeto je, da je inducirano magnetno polje zanemarljivo. Enačba volumskega deleža je rešena za sekundarno fazo. Uporabljen je večfazni Eulerjev model zmesi v dimenzijski obliki. Hitrost fluida ob vseh trdnih stenah je enaka nič, tok na vhodu v kanal brez valja pa je popolnoma razvit. Na izhodu je privzet konstanten referenčni tlak, ničelni hitrostni gradient v toku pa je šibko privzet z obravnavo difuzijskega člena momentne enačbe po Galerkinu. Za sklopitev tlaka in hitrosti je bil uporabljen algoritem SIMPLE. Za ohranitev časovne natančnosti sheme tretjega reda je na Dirichletovih mejnih hitrostih uveljavljen Neumannov pogoj višjega reda za tlačni gradient. Cilinder je toplotno izoliran.

Simulacije so bile izvedene v paketu ANSYS FLUENT 15.0. Za diskretizacijo vodilnih tokovnih in energijskih enačb v prostoru je bila uporabljena metoda vozliščnega spektralnega elementa, za časovno integracijo pa shema tretjega reda na podlagi vzvratnega odvajanja.

Indeksi uspešnosti so bili v vseh primerih večji od ena, s čimer je dokazana možnost izboljšanja prenosa toplote v obravnavanem toku. Najboljše rezultate je dala postavitev cilindra s količnikom vrzeli od 0,75- do 1,25-kratnika premera, s 100-odstotnim izboljšanjem indeksa uspešnosti pri največjem količniku zapiranja. Enak trend je bil ugotovljen za vse količnike zapiranja. Največji indeks uspešnosti je bil vedno dosežen pri količniku vrzeli ena, in sicer pri vseh količnikih zapiranja. Domneve o kvazi dvodimenzionalni naravi modela so potrjene. Za območjem postavitve valja od začetka kanala do desetkratnika premera valja navzdol po toku, v katerem je bilo ugotovljeno postopno povečevanje indeksa uspešnosti, indeks spet pada. Najboljši indeks uspešnosti 2,43 je bil zabeležen pri postavitvi valja na mesto 10 premerov navzdol po toku pri Re = 3000 in jakosti magnetnega polja Ha = 20 s količnikom zapiranja 0,4 ter količnikom položaja in količnikom vrzeli 1. Vrednosti Nu v študiji so bile primerjane s predhodno objavljenimi analitičnimi in eksperimentalnimi podatki in ugotovljeno je bilo popolno ujemanje, ki potrjuje zanesljivost predlaganega modela. Vrtinčna sled je bila tesno povezana s temperaturnimi linijami.

Za morebitno dodatno izboljšanje prenosa toplote bi bilo treba opraviti še simulacije za vrednosti Re nad 3000, količnik zapiranja nad 0,4, volumske koncentracije nanodelcev nad 2 % in postavitev valja več kot 10 premerov navzdol po toku.

Kot zastojno telo v toku MHD-nanofluida pri višjih Reynoldsovih številih je bil uporabljen krožni valj. Podan je predlog idealnega položaja valja glede na količnik zapiranja, položaja in vrzeli. Z numeričnimi simulacijami in pridobljenimi napovedmi kvazi 2D-modela je bil potrjen potencial za izboljšanje prenosa toplote. Dosežena je bila zelo velika izboljšava indeksa uspešnosti ob upoštevanju vpliva vrednosti Re, Ha in φ na tok v pravokotnem kanalu.

Ključne besede: računalniška dinamika tekočin, izboljšan prenos toplote, zastojno telo, krožni valj, magnetohidrodinamika

*Naslov avtorja za dopisovanje: Indijski inštitut za tehnologijo, Oddelek za strojništvo, (ISM), Dhanbad, Indija, arjun@mece.ism.ac.in

Strojniški vestnik - Journal of Mechanical Engineering 63(2017)4, SI 36
© 2017 Strojniški vestnik. Vse pravice pridržane.
Prejeto v recenzijo: 2016-07-19
Prejeto popravljeno: 2016-12-12
Odobreno za objavo: 2016-12-16

Vrednotenje zanesljivosti ležajev na podlagi podatkov o degradaciji zmogljivosti iz malih vzorcev

Luosheng Qin – Xuejin Shen* – Xiaoyang Chen – Pandong Gao
Univerza v Šanghaju, Šola za mehatroniko in avtomatizacijo, Kitajska

Zanesljivost ležajev, ki so vgrajeni v praktično vsak stroj, je pomembna za uspešno delovanje izdelka. Zanesljivo pridobivanje podatkov o življenjski dobi ležajev je težavna naloga, a podatki o degradaciji zmogljivosti na srečo vsebujejo tudi informacije o zanesljivosti. Zanesljivost izdelkov je tako mogoče vrednotiti na podlagi podatkov o degradaciji zmogljivosti.

Obstoječe metode pa običajno zahtevajo velike vzorce in zato je namen tega prispevka vrednotenje zanesljivosti ležajev na podlagi podatkov iz malih vzorcev. Za razrešitev problema je predlagana mešana uporaba metode degradacije na osnovi porazdelitve ter metode Bootstrap v kombinaciji z metodo Monte Carlo (na kratko DDBMC).

Metoda degradacije na osnovi porazdelitve je predlagana za vrednotenje zanesljivosti ležajev iz podatkov o degradaciji zmogljivosti, metodi Bootstrap in Monte Carlo pa sta kombinirani za ocenitev parametrov porazdelitve degradacije pri manjših podatkovnih nizih. Metoda Monte Carlo je bila uporabljena za ustvarjanje naključnih vzorcev iz originalnih vzorcev. Posebna metoda ustvarjanja po Taylorju in Thompsonu je primerna za ocenjevanje parametrov porazdelitve pri malih podatkovnih nizih. Metoda Bootstrap je bila uporabljena za ponovno vzorčenje ustvarjenih vzorcev in pridobitev novih vzorcev.

Parametri novih vzorcev in originalnih vzorcev v vsakem trenutku so bili ocenjeni po metodi največje verjetnosti. Končni rezultati so bili nato pridobljeni z združitvijo parametrov novih in originalnih vzorcev za vsak trenutek. Parametrom porazdelitve podatkov o degradaciji v vsaki merilni točki so bile nato določene ustrezne poti degradacije po metodi najmanjših kvadratov. Končno je bila razrešena še funkcija zanesljivosti ležajev s pretvorbo poti degradacije parametrov porazdelitve v standardno porazdelitveno funkcijo.

Pri eksperimentalnem preizkusu ležajev so bili rezultati ocene zanesljivosti po metodi DDBMC kombinirani z rezultati, izračunanimi po oceni največje verjetnosti (MLE) s podatki o življenjski dobi preizkušenih ležajev. Ugotovljeno je bilo, da je metoda DDBMC primerna za ocenjevanje zanesljivosti ležajev s podatki o degradaciji iz malih vzorcev. Na podlagi eksperimentalnih primerov je bilo ugotovljeno, da je metoda DDBMC uporabna za vrednotenje zanesljivosti ležajev s podatki o degradaciji iz malih vzorcev.

Metoda DDBMC tako omogoča preizkušanje življenjske dobe ležajev na malih vzorcih, v krajšem času in z nižjimi stroški. Metoda DDBMC omogoča vrednotenje zanesljivosti ležajev na malih vzorcih in brez podatkov o življenjski dobi. Omeniti pa je treba, da metoda DDBMC ne upošteva problema manjšega števila merilnih točk, ki zahteva dodatno pozornost.

Ključne besede: ležaji, degradacija na podlagi porazdelitve, mali vzorec, metoda Bootstrap, metoda Monte Carlo, zanesljivost

*Naslov avtorja za dopisovanje: Univerza v Šanghaju, Šola za mehatroniko in avtomatizacijo, p,p. 17, 149 Yanchang, Shanghai, Kitajska, shenxj@i.shu.edu.cn

Strojniški vestnik - Journal of Mechanical Engineering 63(2017)4, SI 37
© 2017 Strojniški vestnik. Vse pravice pridržane.
Prejeto v recenzijo: 2016-05-08
Prejeto popravljeno: 2016-08-06
Odobreno za objavo: 2016-12-07

Eksperimentalna raziskava in numerična simulacija superplastičnega preoblikovanja zlitine AA 5083 s programirljivim logičnim krmilnikom

Muthusamy Balasubramanian[1,*] – Pasupathy Ganesh[2] – Kalimuthu Ramanathan[3] – Velukkudi Santhanam Senthil Kumar[4]

[1] Univerza Anna, Univerzitetni tehniški kolidž, Indija
[2] Univerza Anna, Tehniški inštitut Madras, Indija
[3] Kolidž za inženiring in tehnologijo Alagappa Chettiar, Indija
[4] Univerza Anna, Tehniški kolidž Guindy, Indija

Superplastično preoblikovanje je pomembna tehnologija, primerna za izdelavo delov raznih dimenzij v eni sami preoblikovalni operaciji in z možnimi aplikacijami v letalski in vesoljski industriji ter v proizvodnji zunanjih delov avtomobilov in turbinskih lopatic. Pomembno vlogo v vsakem procesu večdimenzijskega superplastičnega preoblikovanja imajo dejavniki kot so enakomerna porazdelitev debeline, preprečevanje čezmernega tanjšanja in končni izdelki brez gub. Enakomerna porazdelitev debeline pri večdimenzijskem profilu je nujna za nadzor tlaka med preoblikovanjem. Pogoj za nadzorovanje tlaka med preoblikovanjem je tudi optimalna hitrost obremenjevanja.

Predlagana je nova metoda za napovedovanje tlaka med procesom superplastičnega preoblikovanja pločevine iz zlitine AA 5083 s programirljivim logičnim krmilnikom (PLC). Metoda zagotavlja boljši profil enakomerne debeline na kompleksnem večdimenzijskem profilu kot obstoječa metoda. Za optimizacijo tlaka med procesom preoblikovanja je potrebna optimalna hitrost preoblikovanja. Točen nadzor nad velikostjo in trajanjem preoblikovalnega tlaka zagotavlja enakomerno porazdelitev debeline na vstopu orodja, v vogalu, na konusu in v območjih mikropreoblikovanja večdimenzijske kupole. Predstavljen je tudi poizkus preiskave superplastičnega preoblikovanja zlitine AA 5083 v tristopenjsko večdimenzijsko kupolo. Lastnosti preoblikovanja, kot so debelina polov, porazdelitev debeline, povprečna debelina, faktor tanjšanja in čas preoblikovanja, so bile preučene kot funkcije tlaka preoblikovanja, koeficienta trenja in indeksa občutljivosti na hitrost preoblikovanja. Tristopenjski postopek superplastičnega preoblikovanja je bil opravljen eksperimentalno in simuliran po metodi končnih elementov (MKE) s paketom ABAQUS. Spremembe profila debeline so bile izmerjene eksperimentalno in z analizo MKE na vstopu orodja, v vogalu orodja, na konusu in v območjih mikropreoblikovanja s tremi različnimi metodami nadzora tlaka: z algoritmom z omejitvami, logaritmičnim algoritmom in novo metodo s PLC-jem. Tlak je bil optimiziran za enakomerno porazdelitev debeline v območju vstopa orodja, v vogalu orodja, na konusu ter v območjih mikropreoblikovanja, vse pa z najkrajšim časom preoblikovanja.

Rezultati opravljenih eksperimentov po metodi PLC so odlični in material je bil v dobrem stiku s površino orodja s skoraj dokončno obliko tristopenjskega večdimenzijskega profila in z enakomerno porazdelitvijo debeline brez gubanja na vstopu orodja, v vogalu, na konusu in v območjih mikropreoblikovanja. Za primerjavo z eksperimentalnimi rezultati je bila opravljena simulacija po MKE s paketom ABAQUS. Rezultati metode končnih elementov se dobro ujemajo z eksperimentalnimi rezultati glede enakomerne porazdelitve debeline, časa preoblikovanja, tlaka preoblikovanja in stika s površino. Časovni cikel tlaka, pridobljen s tem pristopom, zagotavlja enakomerno porazdelitev debeline v večdimenzijskem profilu z minimalnim časom preoblikovanja (51 min) v primerjavi z rezultati algoritma z omejitvami (62 min) in logaritmičnim vodenjem (57 min). Za točen nadzor nad tlakom pri večstopenjskem profilu in izboljšanje profila debelosti brez gub je bila uporabljena metoda končnih elementov. Profil tlaka, napovedan po MKE (v paketu ABAQUS), se dobro ujema z rezultati eksperimentov.

Razviti sistem PLC učinkovito vodi superplastično preoblikovanje pločevine iz zlitine AA5083 v gnezdu brez pomembnejših zožitev. Porazdelitev debeline na vstopu v orodje in v vogalu je enakomerna tudi pri kompleksnem večdimenzijskem profilu, kot je bil uporabljen pri tem delu. Vezje PLC tudi učinkovito uravnava velikost in trajanje tlačnega cikla za optimizacijo kakovosti debeline in superplastično preoblikovanje večdimenzijskih komponent brez gub. MKE je zelo zanesljivo orodje za analizo in optimizacijo procesov superplastičnega preoblikovanja s spreminjanjem ravni trenja in indeksa občutljivosti na hitrost obremenjevanja, ki pomagata napovedovati pomembne parametre, kot so porazdelitev debeline, čas preoblikovanja in tlačni profil. V prihodnje bo treba preučiti še velikost zrn in mikrostrukturo preoblikovanih komponent v območjih mikropreoblikovanja.

Ključne besede: superplastično preoblikovanje, metoda končnih elementov, programirljiv logični krmilnik, aluminijeva zlitina 5083, večstopenjska večdimenzijska kupola

*Naslov avtorja za dopisovanje: Univerza Anna, Univerzitetni tehniški kolidž,Tamil Nadu, Indija, annaunivbala76@gmail.com

Strojniški vestnik - Journal of Mechanical Engineering 63(2017)4, SI 38
© 2017 Strojniški vestnik. Vse pravice pridržane.
Prejeto v recenzijo: 2016-12-12
Prejeto popravljeno: 2017-01-05
Odobreno za objavo: 2017-03-22

Nadzor kurjave s sprotno pripravo premogovega prahu z uporabo statistično obdelanih signalov elektrostatičnih merilnih sond

Boštjan Jurjevčič – Andrej Senegačnik – Igor Kuštrin*
Univerza v Ljubljani, Fakulteta za strojništvo, Slovenija

Namen raziskave je bil razviti učinkovito in robustno metodo za sprotno spremljanje karakteristik pnevmatskega transporta premogovega prahu od mlina do šob gorilnika v realnih obratovalnih pogojih. Med drugim naj bi omogočala pravočasno zaznavanje stanja preobremenjenosti mlina.

Zaradi nestanovitne proizvodnje električne energije s sončnimi in vetrnimi elektrarnami se zahteva vse bolj fleksibilna proizvodnja električne energije s termoelektrarnami. Istočasno se zahteva, da so izpusti škodljivih snovi in učinkovitost proizvodnje s termoelektrarnami znotraj dopustnih meja. Za kakovostno in stabilno zgorevanje je nujno, da se na vseh šobah gorilnikov stalno vzdržuje optimalno masno razmerje med premogovim prahom in zgorevalnim zrakom in da ne prihaja do občasnih preobremenitev mlinov za premog. Preobremenitve ventilatorskih mlinov, ki se uporabljajo za mletje lignita in rjavega premoga, so pogost pojav. Posledice prepozno zaznane preobremenitve mlina se odražajo v nedopustnem nihanju pretoka, temperature in tlaka pare, ki jo proizvaja kotel, še nekaj časa po razbremenitvi mlina. V najslabšem primeru lahko pride tudi do prekinitve proizvodnje pare. Trenutno se za zaznavanje preobremenitve mlinov uporablja merjenje temperature zmesi premogovega prahu in nosilnih plinov na izstopu iz mlina. Prehitro padanje temperature in prenizka temperatura prašne zmesi sta znak preobremenjenosti mlina. Izkušnje kažejo, da je ta metoda sicer uporabna, a običajno nekoliko prepozno sproži opozorilo.

V raziskavi so bile uporabljene elektrostatične merilne sonde in ustrezen elektronski sistem za zapisovanje in obdelavo njihovih signalov. Zaradi velikih presekov prahovodnih kanalov ni primerna uporaba toku nevsiljenih elektrostatičnih zaznaval, ki so vgrajena v stene kanalov in imajo zato omejeno zmožnost zaznavanja karakteristik toka oddaljenega od sten kanalov. Za reprezentativno merjenje je bilo potrebno uporabiti sonde, ki so potekale skozi kanal vzporedno ena z drugo v ravnini pravokotni na tok. Signali so bili merjeni s frekvenco 1000 Hz. Frekvenca je bila izbrana glede na predhodne preizkuse tako, da se je z zmerno količino izmerkov dovolj natančno posnel časovni potek signalov. Surove časovne vrste izmerkov so bile nato obdelane s statističnimi metodami za zmanjševanje avtokoreliranosti med sosednjimi izmerki. Zaporedno sta bili uporabljeni dve metodi: tvorjenje neuteženih povprečij podskupin zaporednih izmerkov, kot metoda zmanjševanja avtokoreliranosti brez modeliranja in nato še metoda, ki sloni na ARIMA (Autoregressive Integrated Moving Average) modelu. Odstopki med izmerki in modeliranimi vrednostmi ARIMA modela vstopajo v EWMA (Exponentially Weighted Moving Average) kontrolni diagram, ki služi za statistični nadzor procesa.

Analiza je pokazala, da je predlagana metoda statistične obdelave surovih izmerkov elektrostatičnih zaznaval zelo primerna za zaznavanje nenadnih hitrih sprememb pnevmatskega transporta in zaradi tega tudi za zgodnjo detekcijo preobremenjenosti mlina. Opozorilni signali predlagane metode so zanesljivi in zgodnejši v primerjavi z opozorilnimi signali, ki se sprožijo na podlagi merjenja temperature prašne zmesi na izstopu iz mlina.

Predlagana metoda vključuje uporabo elektrostatičnih merilnih sond, ki so vrinjene v kanal in podvržene abraziji ter jih je zato potrebno redno menjavati. Časovni razmik med zamenjavami zaznaval je odvisen od odpornosti materiala sond in abrazivnosti premogovega prahu. Nastavitve ARIMA modela in EWMA kontrolnega diagrama niso univerzalne in jih je potrebno optimizirati za vsak objekt.

Uporaba ARIMA modela in EWMA kontrolnega diagrama je pogosto predstavljena v literaturi in je uporabna za nadzor mnogih procesov. V tej raziskavi sta prvič uporabljeni v povezavi z zaznavanjem motenj v pnevmatskem transportu premogovega prahu od ventilatorskega mlina do gorilnikov. Predlagana metoda omogoča pravočasno zaznavanje in posledično preprečevanje stanj preobremenjenosti mlinov za premog, kar omogoča stabilnejše obratovanje velikih parnih kotlov s sprotno pripravo premogovega prahu.

Ključne besede: ARIMA model, elektrostatična merilna metoda, kontrolni diagram, ventilatorski mlin, pnevmatski transport, premogov prah, statistično modeliranje

*Naslov avtorja za dopisovanje: Univerza v Ljubljani, Fakulteta za strojništvo, Aškerčeva 6, 1000 Ljubljana, Slovenija, igor.kustrin@fs.uni-lj.si

Strojniški vestnik - Journal of Mechanical Engineering 63(2017)4, SI 39
© 2017 Strojniški vestnik. Vse pravice pridržane.
Prejeto v recenzijo: 2016-08-30
Prejeto popravljeno: 2016-12-02
Odobreno za objavo: 2016-12-16

Analiza odpovedi večstopenjskega vrstnega rotacijskega tesnila v vodi pod visokim tlakom

Zenghui Liu[1,2] – Changlong Du[1,*] – Songyong Liu[1] – Hongxiang Jiang[1]
[1] Kitajska rudarska in tehniška univerza, Šola za mehatroniko, Kitajska
[2] Univerza Monash, Oddelek za gradbeništvo, Avstralija

Napredovalni stroji si pri razbijanju trde skale pomagajo z visokotlačnimi vodnimi curki. Pri tem je pomemben dejavnik doba do odpovedi visokotlačnih rotacijskih tesnil (HPRS), ki vpliva na varnost in učinkovitost napredovalnega stroja. Članek opisuje eksperimentalno raziskavo mehanskih lastnosti HPRS.

Eksperimentalna analiza enostopenjskega vrstnega rotacijskega tesnila je pokazala, da so mehanske lastnosti kombiniranega tesnila boljše od lastnosti obročnega tesnila zaradi manjšega tornega navora, večjega kontaktnega pritiska in manj puščanja. Puščanje pri obročnih tesnilih se z delovnim tlakom povečuje, pri kombiniranih tesnilih pa zmanjšuje. Puščanje pri nižjih hitrostih vretena se povečuje s hitrostjo do določene vrednosti, nato pa praktično ni več odvisno od dodatne rasti hitrosti.

Za kombinirana tesnila velja, da so pri večjih vrednostih Δp večje tudi deformacije obročnega tesnila. To lahko povzroči večji kontaktni pritisk med zobatim drsnim obročem in gredjo ter manjše puščanje. Pri obročnem tesnilu povzroči večja vrednost Δp večje deformacije, tesnilo se lahko zvije in če so deformacije dovolj velike, ga lahko celo obrne. Puščanje se tedaj povečuje sorazmerno z Δp. Pri običajnem obročnem tesnilu sta statično in dinamično puščanje pri delovnem tlaku 40 MPa presegala dovoljeno največjo vrednost 50 ml/h. Običajno obročno tesnilo zato ni primerno za uporabo v rotacijskih tesnilih pod visokim tlakom in za preizkus dobe do odpovedi večstopenjskega rotacijskega tesnila je bilo izbrano kombinirano tesnilo. Ugotovljeno je bilo, da je doba do odpovedi rotacijskih tesnil od 1. do 4. stopnje 15, 11, 5 oz. 4 dni.

Temperatura v vseh stopnjah raste s časom, pri čemer temperatura v 1. in 2. stopnji raste počasneje na začetku preizkusa in nato hitreje do odpovedi, temperatura v 3. in 4. stopnji pa zraste takoj. Trend krivulj puščanja je podoben trendu temperaturnih krivulj. Ko je bila lekažna odprtina v 1. stopnji zamašena z navojnim čepom, se je lahko voda pod visokim tlakom pretakala v rotacijsko tesnilo 2. stopnje in nekaj odpadkov je prišlo neposredno do stika 2. stopnje. Krivulje 2. stopnje zato nimajo stabilne periode v primerjavi s 1. stopnjo in doba do odpovedi je krajša kot v 1. stopnji. Najtežje poškodbe so bile ugotovljene na stiku 1. stopnje, najmanjše pa v 4. stopnji. Razlog je v tem, da trenje na stiku 1. stopnje nikoli ne izgine zaradi slabe toplotne prevodnosti in velikega temperaturnega koeficienta dolžinskega raztezka materiala PTFE. Tako zaide več odpadkov PTFE in kovine iz 1. in 2. stopnje do stika 3. in 4. stopnje, zaradi česar se močno povišata temperatura in puščanje, rotacijsko tesnilo pa hitro odpove.

Celotna doba do odpovedi večstopenjskega vrstnega rotacijskega tesnila je bila 35 dni, mnogo nad pričakovanji. Delovna vrtilna hitrost gredi je bila večino časa okrog 50 obr./min in ne 100 obr./min. Dejanska doba do odpovedi štiristopenjskega rotacijskega tesnila v delovnih pogojih bi bila zato daljša od 35 dni, presežna doba do odpovedi pa lahko šteje kot varnostni faktor. Pri večstopenjskem vrstnem rotacijskem tesnilu je doba do odpovedi višje stopnje prekratka v primerjavi z nižjo stopnjo. Priporočljiva je uporaba tri- ali štiristopenjskih rotacijskih tesnil.

Ključne besede: analiza odpovedi, rotacijsko tesnilo, mehansko preizkušanje, obraba, visok tlak

*Naslov avtorja za dopisovanje: Kitajska rudarska in tehniška univerza, Šola za mehatroniko, Xuzhou, Kitajska, duclhxj @cumt.edu.cn.

DOKTORSKI DISERTACIJI

Na Fakulteti za strojništvo Univerze v Mariboru je obranil svojo doktorsko disertacijo:

- dne *24. marca 2017* **Uroš KOKOLJ** z naslovom: »Numerično napovedovanje funkcionalnih lastnosti pečniškega prostora« (mentor: prof. dr. Leopold Škerget);

Cilj vseh proizvajalcev in uporabnikov pečic je imeti kar se da enakomerno zapečenost različnih jedi. To pa proizvajalci v zadnjih časih zaradi novih trendov in vse krajših razvojnih časov izdelkov težko dosegajo. Zato se je za potrebe numeričnega napovedovanja funkcionalnih lastnosti pečniškega prostora razvil časovno odvisen tridimenzionalni (3D) numerični model, ki se je preverjal z eksperimentalnimi meritvami. V modelu je obravnavan sistem vročega zraka, v katerem delujeta okroglo grelo in ventilator, prevladujoča sta sevanje in prisilna konvekcija. Zaradi obravnave prisilne konvekcije je zelo pomembna ustrezna izbira modela turbulence. Predstavljena je uporaba različnih modelov turbulence. Za obravnavano pečico se je kot najprimernejši izkazal SST-model turbulence. Ugotovljeno je bilo, da je v numerični model nujno treba vključiti proces izparevanja. Numerični model se je preverjal z eksperimentalnimi meritvami temperature in s funkcionalnimi preizkusi pečenja peciva. Po končanju preizkusa pečenja se je piškotom z metodo določevanja barvnih kontrastov, ki temelji na CIE L*a*b barvnem prostoru, določila stopnja porjavelosti Ry. Glede na rezultate se je predlagal linearni model, ki bo omogočal napovedovanje rezultatov porjavelosti s pomočjo numeričnih izračunov. Dodatno preverjanje modela se je izvedlo na področju optimizacije oziroma izboljšave pečenja pečice. S pomočjo numeričnih izračunov se je preverilo šest različnih izvedb pokrova ventilatorja. Na podlagi numeričnih izračunov se je določila numerična stopnja porjavelosti. Numerični rezultati so se preverjali s pomočjo eksperimentalnih preizkusov, ki so se izvedli na starem in novem pokrovu ventilatorja. Tako numerični kot eksperimentalni rezultati so pokazali, da izboljšan pokrov ventilatorja zagotovi boljše rezultate enakomernosti pečenja.

*

Na Fakulteti za strojništvo Univerze v Ljubljani je obranil svojo doktorsko disertacijo:

- dne *31. marca 2017* **Luca PETAN** z naslovom: »Lasersko udarno utrjevanje maraging jekla« (mentor: prof. dr. Janez Grum);

Doktorska disertacija obravnava možnost aplikacije laserskega udarnega utrjevanja na visokotrdnostnem in izločevalno utrjevalnem jeklu iz skupine maraging. Zaradi izjemnih mehanskih lastnosti se maraging jekla uporabljajo za izdelavo kritičnih in visokotehnoloških strojnih delov, ki so pogosto izpostavljena različnim oblikam utrujanja in obrabe. V okviru raziskovalnega dela je bil analiziran vpliv različnih kombinacij procesnih parametrov laserskega udarnega utrjevanja na integriteto površine maraging jekla X2NiCoMo18-9-5. Analiziran je bil efekt lasersko induciranih tlačnih zaostalih napetosti v površinskem sloju na odpornost maraging jekla na iniciacijo in rast razpok med mehanskim in termičnim utrujanjem. Za primerjavo je bil raziskan tudi efekt obravnavanega laserskega postopka na orodnem jeklu za delo v vročem X38CrMoV5-1. Analiza karakteristik površinskega sloja in testi utrujanja potrjujejo izboljšanje mehanskih lastnosti obravnavanih jekel po laserskem udarnem utrjevanju.

Information for Authors

All manuscripts must be in English. Pages should be numbered sequentially. The manuscript should be composed in accordance with the Article Template given above. The maximum length of contributions is 10 pages. Longer contributions will only be accepted if authors provide juastification in a cover letter. For full instructions see the Information for Authors section on the journal's website: http://en.sv-jme.eu .

SUBMISSION:

Submission to SV-JME is made with the implicit understanding that neither the manuscript nor the essence of its content has been published previously either in whole or in part and that it is not being considered for publication elsewhere. All the listed authors should have agreed on the content and the corresponding (submitting) author is responsible for having ensured that this agreement has been reached. The acceptance of an article is based entirely on its scientific merit, as judged by peer review. Scientific articles comprising simulations only will not be accepted for publication; simulations must be accompanied by experimental results carried out to confirm or deny the accuracy of the simulation. Every manuscript submitted to the SV-JME undergoes a peer-review process.

The authors are kindly invited to submit the paper through our web site: http://ojs.sv-jme.eu. The Author is able to track the submission through the editorial process - as well as participate in the copyediting and proofreading of submissions accepted for publication - by logging in, and using the username and password provided.

SUBMISSION CONTENT:

The typical submission material consists of:

- A **manuscript** (A PDF file, with title, all authors with affiliations, abstract, keywords, highlights, inserted figures and tables and references),
- Supplementary files:
  - a **manuscript** in a WORD file format
  - a **cover letter** (please see instructions for composing the cover letter)
  - a ZIP file containing **figures** in high resolution in one of the graphical formats (please see instructions for preparing the figure files)
  - possible **appendicies** (optional), cover materials, video materials, etc.

Incomplete or improperly prepared submissions will be rejected with explanatory comments provided. In this case we will kindly ask the authors to carefully read the Information for Authors and to resubmit their manuscripts taking into consideration our comments.

COVER LETTER INSTRUCTIONS:

Please add a **cover letter** stating the following information about the submitted paper:

1. Paper **title**, list of **authors** and their **affiliations**.
2. **Type of paper**: original scientific paper (1.01), review scientific paper (1.02) or short scientific paper (1.03).
3. A **declaration** that neither the manuscript nor the essence of its content has been published in whole or in part previously and that it is not being considered for publication elsewhere.
4. State the **value of the paper** or its practical, theoretical and scientific implications. What is new in the paper with respect to the state-of-the-art in the published papers? Do not repeat the content of your abstract for this purpose.
5. We kindly ask you to suggest at least two **reviewers** for your paper and give us their names, their full affiliation and contact information, and their scientific research interest. The suggested reviewers should have at least two relevant references (with an impact factor) to the scientific field concerned; they should not be from the same country as the authors and should have no close connection with the authors.

FORMAT OF THE MANUSCRIPT:

The manuscript should be composed in accordance with the Article Template. The manuscript should be written in the following format:

- A **Title** that adequately describes the content of the manuscript.
- A list of **Authors** and their **affiliations**.
- An **Abstract** that should not exceed 250 words. The Abstract should state the principal objectives and the scope of the investigation, as well as the methodology employed. It should summarize the results and state the principal conclusions.
- 4 to 6 significant **key words** should follow the abstract to aid indexing.
- 4 to 6 **highlights;** a short collection of bullet points that convey the core findings and provide readers with a quick textual overview of the article. These four to six bullet points should describe the essence of the research (e.g. results or conclusions) and highlight what is distinctive about it.
- An **Introduction** that should provide a review of recent literature and sufficient background information to allow the results of the article to be understood and evaluated.
- A **Methods** section detailing the theoretical or experimental methods used.
- An **Experimental section** that should provide details of the experimental set-up and the methods used to obtain the results.
- A **Results** section that should clearly and concisely present the data, using figures and tables where appropriate.
- A **Discussion** section that should describe the relationships and generalizations shown by the results and discuss the significance of the results, making comparisons with previously published work. (It may be appropriate to combine the Results and Discussion sections into a single section to improve clarity.)
- A **Conclusions** section that should present one or more conclusions drawn from the results and subsequent discussion and should not duplicate the Abstract.
- **Acknowledgement** (optional) of collaboration or preparation assistance may be included. Please note the source of funding for the research.
- **Nomenclature** (optional). Papers with many symbols should have a nomenclature that defines all symbols with units, inserted above the references. If one is used, it must contain all the symbols used in the manuscript and the definitions should not be repeated in the text. In all cases, identify the symbols used if they are not widely recognized in the profession. Define acronyms in the text, not in the nomenclature.
- **References** must be cited consecutively in the text using square brackets [1] and collected together in a reference list at the end of the manuscript.
- **Appendix(-icies)** if any.

SPECIAL NOTES

Units: The SI system of units for nomenclature, symbols and abbreviations should be followed closely. Symbols for physical quantities in the text should be written in italics (e.g. *v*, *T*, *n*, etc.). Symbols for units that consist of letters should be in plain text (e.g. ms^{-1}, K, min, mm, etc.). Please also see: http://physics.nist.gov/cuu/pdf/sp811.pdf .

Abbreviations should be spelt out in full on first appearance followed by the abbreviation in parentheses, e.g. variable time geometry (VTG). The meaning of symbols and units belonging to symbols should be explained in each case or cited in a **nomenclature** section at the end of the manuscript before the References.

Figures (figures, graphs, illustrations digital images, photographs) must be cited in consecutive numerical order in the text and referred to in both the text and the captions as Fig. 1, Fig. 2, etc. Figures should be prepared without borders and on white grounding and should be sent separately in their original formats. If a figure is composed of several parts, please mark each part with a), b), c), etc. and provide an explanation for each part in Figure caption. The caption should be self-explanatory. Letters and numbers should be readable (Arial or Times New Roman, min 6 pt with equal sizes and fonts in all figures). Graphics (submitted as supplementary files) may be exported in resolution good enough for printing (min. 300 dpi) in any common format, e.g. TIFF, BMP or JPG, PDF and should be named Fig1.jpg, Fig2.tif, etc. However, graphs and line drawings should be prepared as vector images, e.g. CDR, AI. Multi-curve graphs should have individual curves marked with a symbol or otherwise provide distinguishing differences using, for example, different thicknesses or dashing.

Tables should carry separate titles and must be numbered in consecutive numerical order in the text and referred to in both the text and the captions as Table 1, Table 2, etc. In addition to the physical quantities, such as *t* (in italics), the units [s] (normal text) should be added in square brackets. Tables should not duplicate data found elsewhere in the manuscript. Tables should be prepared using a table editor and not inserted as a graphic.

REFERENCES:

A reference list must be included using the following information as a guide. Only cited text references are to be included. Each reference is to be referred to in the text by a number enclosed in a square bracket (i.e. [3] or [2] to [4] for more references; do not combine more than 3 references, explain each). No reference to the author is necessary.

References must be numbered and ordered according to where they are first mentioned in the paper, not alphabetically. All references must be complete and accurate. Please add DOI code when available. Examples follow.

Journal Papers:

Surname 1, Initials, Surname 2, Initials (year). Title. Journal, volume, number, pages, DOI code.

[1] Hackenschmidt, R., Alber-Laukant, B., Rieg, F. (2010). Simulating nonlinear materials under centrifugal forces by using intelligent cross-linked simulations. *Strojniški vestnik - Journal of Mechanical Engineering,* vol. 57, no. 7-8, p. 531-538, DOI:10.5545/sv-jme.2011.013.

Journal titles should not be abbreviated. Note that journal title is set in italics.

Books:

Surname 1, Initials, Surname 2, Initials (year). Title. Publisher, place of publication.

[2] Groover, M.P. (2007). *Fundamentals of Modern Manufacturing*. John Wiley & Sons, Hoboken.

Note that the title of the book is italicized.

Chapters in Books:

Surname 1, Initials, Surname 2, Initials (year). Chapter title. Editor(s) of book, book title. Publisher, place of publication, pages.

[3] Carbone, G., Ceccarelli, M. (2005). Legged robotic systems. Kordić, V., Lazinica, A., Merdan, M. (Eds.), Cutting Edge Robotics. Pro literatur Verlag, Mammendorf, p. 553-576.

Proceedings Papers:

Surname 1, Initials, Surname 2, Initials (year). Paper title. Proceedings title, pages.

[4] Štefanić, N., Martinčević-Mikić, S., Tošanović, N. (2009). Applied lean system in process industry. *MOTSP Conference Proceedings*, p. 422-427.

Standards:

Standard-Code (year). Title. Organisation. Place.

[5] ISO/DIS 16000-6.2:2002. *Indoor Air – Part 6: Determination of Volatile Organic Compounds in Indoor and Chamber Air by Active Sampling on TENAX TA Sorbent, Thermal Desorption and Gas Chromatography using MSD/FID.* International Organization for Standardization. Geneva.

WWW pages:

Surname, Initials or Company name. Title, from http://address, date of access.

[6] Rockwell Automation. Arena, from *http://www.arenasimulation.com,* accessed on 2009-09-07.

EXTENDED ABSTRACT:

When the paper is accepted for publishing, the authors will be requested to send an **extended abstract** (approx. one A4 page or 3500 to 4000 characters). The instruction for composing the extended abstract are published on-line: http://www.sv-jme.eu/information-for-authors/ .

COPYRIGHT:

Authors submitting a manuscript do so on the understanding that the work has not been published before, is not being considered for publication elsewhere and has been read and approved by all authors. The submission of the manuscript by the authors means that the authors automatically agree to transfer copyright to SV-JME when the manuscript is accepted for publication. All accepted manuscripts must be accompanied by a Copyright Transfer Agreement, which should be sent to the editor. The work should be original work by the authors and not be published elsewhere in any language without the written consent of the publisher. The proof will be sent to the author showing the final layout of the article. Proof correction must be minimal and executed quickly. Thus it is essential that manuscripts are accurate when submitted. Authors can track the status of their accepted articles on http://en.sv-jme.eu/.

PUBLICATION FEE:

Authors will be asked to pay a publication fee for each article prior to the article appearing in the journal. However, this fee only needs to be paid after the article has been accepted for publishing. The fee is 240.00 EUR (for articles with maximum of 6 pages), 300.00 EUR (for articles with maximum of 10 pages), plus 30.00 EUR for each additional page. The additional cost for a color page is 90.00 EUR. These fees do not include tax.

Strojniški vestnik -Journal of Mechanical Engineering
Aškerčeva 6, 1000 Ljubljana, Slovenia,
e-mail: info@sv-jme.eu

9 770039 248001
ISSN 0039-2480

http://www.sv-jme.eu

Contents

Papers